Laser heating setup with high-magnification imaging for studies of physical and chemical phenomena up to ultra-high pressures in diamond anvil cells

Doctoral Thesis

submitted to obtain the academic degree of Doctor of Natural Sciences

(Dr. rer. nat.)

of the Bayreuth Graduate School of Mathematical and Natural Sciences (BayNAT)

of the University of Bayreuth

Timofey Fedotenko

from *Novosibirsk (Russian Federation)*

Bayreuth, 2021

This doctoral thesis was prepared at the Laboratory of Crystallography (Material Physics and Technology at Extreme Conditions Group) and the Bavarian Research Institute of Experimental Geochemistry and Geophysics (BGI) at the University of Bayreuth from 05/2017 until 04/2021 and was supervised by Prof. Dr. Dr. h. c. Natalia Dubrovinskaia and Prof. Dr. Dr. h. c. Leonid Dubrovinsky.”.

This is a full reprint of the thesis submitted to obtain the academic degree of Doctor of Natural Sciences (Dr. rer. nat.) and approved by the Bayreuth Graduate School of Mathematical and Natural Sciences (BayNAT) of the University of Bayreuth.

Date of submission: 22.04.2021

Date of defence: 14.06.2021

Acting director: Prof. Dr. Markus Lippitz

Doctoral committee:

Prof. Dr. Dr. h.c. Natalia Dubrovinskaia	(reviewer)
PD. Dr. Gerd Steinle-Neumann	(reviewer)
PD. Dr. Catherine McCammon	(chairman)
Prof. Dr. Daniel Frost	

Zusammenfassung

Die in situ Untersuchung von Materialien unter Hochdruck- und Hochtemperaturbedingungen ist von großem Interesse für die moderne Festkörperphysik, Chemie, Material-, Geo- und Planetenwissenschaften. Die Diamantstempelzelle (DAC) ist das Forschungsinstrument, das den breitesten Druckbereich im Vergleich zu anderen statischen Druckerzeugungsmethoden ermöglicht. Gekoppelt mit einer Laserheizung (LH), erweitert die DAC-Technik den zugänglichen thermodynamischen Bereich dramatisch. Sie wird zu einem extrem leistungsfähigen Werkzeug für die Synthese und Untersuchung neuartiger Materialien unter extremen Bedingungen.

Herkömmliche LH-Aufbauten, die in DAC-Experimenten bis zu etwa 200 GPa verwendet werden, ermöglichen die Fokussierung von Laserstrahlen auf Spots in der Größenordnung von 10 µm. Experimente jenseits von 200 GPa erfordern eine engere Fokussierung, da bei solch hohen Drücken die Größe der Proben auf wenige µm reduziert werden muss. Gleichzeitig ist eine qualitativ hochwertige Visualisierung der Probe ein Muss, um das Zeil beim Erhitzen zu erkennen. Um diesen Anforderungen gerecht zu werden, haben wir einen doppelseitigen Laser-Heizaufbau mit hoher Vergrößerung und hochauflösender Bildgebung für Inhouse- und Synchrotron-DAC-Experimente entwickelt. Die Fähigkeiten des Aufbaus zum Heizen bei extrem hohen Drücken wurden in einer Reihe von Inhouse-Experimenten bei Multimegabar-Drücken erfolgreich getestet.

Die Kompatibilität des Aufbaus mit Synchrotrontechniken wurde an der Beamline ID15B an der European Synchrotron Radiation Facility (ESRF) demonstriert. Wir haben es für die gleichzeitige Erwärmung und Visualisierung der Probe mittels Transmission-Röntgenmikroskopie (XRTM) eingesetzt. Unseres Wissens nach ist diese Arbeit die erste Demonstration der Kombination der LHDAC-Technik mit XRTM. Die Anwendbarkeit von XRTM-LHDAC für die in situ Schmelzdetektion wurde in einem Experiment zum Schmelzen von Platin (Pt) bei 22(1) GPa demonstriert. Der mit dieser Methode ermittelte Schmelzpunkt stimmt gut mit den Literaturdaten überein.

Außerdem wurde der entwickelte LH-Aufbau erfolgreich für DAC-Experimente an Carbiden bei moderaten und extrem hohen Drücken eingesetzt, die für die Geo- und Materialwissenschaften relevant sind. Ein neuartiges Nickelcarbid (Ni_3C) mit einer Zementit-Typ Struktur wurde in einer DAC bei 184(5) GPa und 3500(200) K synthetisiert. Seine Kristallstruktur wurde mithilfe von Synchrotron-Einkristall-Röntgenbeugungsdaten (SC-XRD) gelöst und verfeinert. Es wurde festgestellt, dass Ni_3C bis hinunter zu 84(5) GPa stabil ist. Die berechneten akustischen Ausbreitungsgeschwindigkeiten für Ni_3C scheinen denen von Fe_3C und Fe_7C_3 bis zu 400 GPa ähnlich zu sein. Es ist wahrscheinlich, dass die Anwesenheit von Ni im Fe-Ni-C-System die elastischen Eigenschaften bei hohem Druck nicht beeinflusst, aber möglicherweise die Kohlenstoffverteilung verändert. Aufgrund der Stabilität von Ni_3C bei Drücken über 150 GPa sollte es zusammen mit Fe_7C_3 als möglicher Kandidat für kohlenstoffhaltige Phasen im Erdkern betrachtet werden.

Bisher nicht berichtete kohlenstoffreiche Palladiumcarbide (PdC_x) wurden bei etwa 50 GPa und 2500-300 K in LH Diamantstempelzellen durch eine chemische Reaktion von Pd mit Kohlenstoff aus dem Diamantstempel synthetisiert. Die Proben wurden mittels XRD an der Beamline ID15B des ESRF charakterisiert. Das Kompressionsverhalten der Proben wurde bis zu 50 GPa untersucht und die Parameter der Zustandsgleichung (EOS) wurden als V_0 = 65,1(1) Å^3, K_0 = 241(9) GPa, K_0'= 2,1(3) für $PdC_{0.21}$ und V_0 = 64,51(5) Å^3, K_0 = 189(8) GPa, K_0' = 4,5(4) für $PdC_{0.19}$ ermittelt.

Die exzellente Qualität der mikroskopischen Bilder der Proben in DACs, die im Rahmen von LH-Experimenten gewonnen wurden, inspirierte zur Weiterentwicklung des optischen Systems und dessen Einsatz als hochauflösendes optisches Mikroskop. Wir nutzten das System zur Untersuchung des EOS von amorphen Materialien, auf die herkömmliche XRD nicht anwendbar ist. Die entwickelte Methode beruht auf der Verfolgung der linearen Abmessungen der Probe bei ihrer Kompression in der DAC und ermöglicht eine präzise Bestimmung der volumetrischen Kompression. Die Methode wurde durch optische Messungen des EOS von Ti validiert und stimmte sehr gut mit den Ergebnissen überein, die zuvor mit Synchrotron-XRD-Messungen ermittelt wurden. Um noch einen Schritt weiter zu gehen, wurde diese Technik angewendet, um die bisher unbekannte EOS von amorphem Kohlenstoff zu bestimmen. Der Kompressionsmodul und seine Druckableitung wurden mit K_0= 28,6(8) GPa und K_0'= 5,5(2) bestimmt. Somit ist die

optische Mikroskopie sehr attraktiv für die Untersuchung des EOS von Festkörpern. Sie kann sowohl auf kristalline als auch auf nicht-kristalline Materialien angewendet werden und alle Messungen können im Haus durchgeführt werden, was solche Untersuchungen unabhängig von der Zugänglichkeit von Synchrotroneinrichtungen macht.

Zusammenfassend lässt sich sagen, dass die in dieser Dissertation vorgestellten Arbeiten zur Entwicklung der Technik und Methodik von DAC-Experimenten und zur Untersuchung grundlegender Eigenschaften von Materialien unter extremen Bedingungen beitragen. Der Laser-Heizungsaufbau, der zunächst für Hochtemperaturexperimente bei Multi-Megabar-Druck entwickelt wurde, hat eine wichtige Anwendung für die Bestimmung der EOS von amorphen Materialien mit hoher Genauigkeit auf Laboraufbauten gefunden.

Summary

The *in situ* study of matter under high-pressure and high-temperature conditions is of great interest for modern solid-state physics, chemistry, materials, geological, and planetary sciences. The diamond anvil cell (DAC) is the research instrument, enabling the broadest pressure range compared to other static pressure generation methods. Coupled with laser heating (LH), the DAC technique dramatically expands the accessible thermodynamic space. It becomes an extremely powerful tool for the synthesis and studying of novel materials at extreme conditions.

Conventional LH setups, used in DAC experiments up to about 200 GPa, enable focusing of laser beams to spots on the scale of 20 µm. Experiments beyond 200 GPa require tighter focusing, at a such high pressures, the size of samples has to be reduced to a few µm. Simultaneously, to recognize the target upon heating, high-quality visualization of the sample becomes a must. We have developed a double-sided laser-heating setup with high magnification and high optical resolution imaging for in-house and synchrotron DACs experiments to address these demands. The capabilities of the setup for heating at ultra-high pressures have been tested successfully in a series of in-house experiments at multimegabar pressures.

The compatibility of the setup with synchrotron techniques was demonstrated on the beamline ID15B at the European Synchrotron Radiation Facility (ESRF). We applied it for simultaneous heating and visualization of the sample using X-ray transmission microscopy (XRTM). To the best of our knowledge, this thesis work is the first demonstration of combining the LHDAC technique with XRTM. The applicability of XRTM in LHDAC for *in situ* melting detection was showcased in an experiment on melting of platinum Pt at 22(1) GPa. The melting point determined using this method agrees well with the literature data.

Further, the developed LH setup was successfully employed for DAC experiments on carbides at moderate and ultra-high pressures, relevant for geological and materials sciences. A novel nickel carbide (Ni_3C) with the cementite-type structure was synthesized in a DAC at 184(5) GPa and 3500(200) K. Its crystal structure was solved and refined using synchrotron single-crystal X-ray

diffraction (SC-XRD) data. Ni_3C was found to be stable down to 84(5) GPa. The calculated bulk sound velocities for Ni_3C appeared to be similar to those of Fe_3C and Fe_7C_3 up to 400 GPa. Likely, Ni's alloying doesn't affect the elastic properties of in the Fe-Ni-C system but potentially could change the carbon distribution. Due to the stability of Ni_3C at pressures above 150 GPa, it should be considered a possible candidate to carbon-bearing phases in the Earth's core along with Fe_7C_3. Previously not reported carbon-rich palladium carbides (PdC_x, $0.015(1) < x < 0.21(3)$) were synthesized at about 50 GPa and 2500-300 K in LH DACs through the Pd chemical reaction with carbon from various precursors. The samples were characterized using powder XRD at the beamline ID15B of the ESRF. The compressional behavior of the samples was studied up to 50 GPa and the equation of state (EOS) parameters were found to be equal to $V_0 = 65.1(1)$ Å^3, $K_0 = 241(9)$ GPa, $K' = 2.1(3)$ for $PdC_{0.21}$, and $V_0 = 64.51(5)$ Å^3, $K_0 = 189(8)$ GPa, $K' = 4.5(4)$ for $PdC_{0.19}$.

The excellent quality of the microscopic images of the samples in DACs, which were obtained within the course of LH experiments, inspired further development of the optical system and its use as a high-resolution optical microscope. We utilized the system for studying the EOS of amorphous materials, to which conventional XRD is not applicable. The developed method relies on tracking the sample's linear dimensions upon its compression in the DAC and enables precise determination of the volumetric strain. The methodology was validated through optical measurements of the EOS of ω-Ti which agreed very well with the results previously established with synchrotron XRD measurements. Pushing one step further, this technique was applied to determine the previously unknown EOS of glassy carbon. The bulk modulus and its pressure derivative were found to be $K_0 = 28.6(8)$ GPa and $K' = 5.5(2)$. Thus, optical microscopy is very attractive for studying EOSes of solids. It can be applied to both crystalline and none-crystalline materials and all measurements can be conducted in-house, making such investigations independent of the accessibility of synchrotron facilities.

To summarize, the work presented in the thesis contributes to the development of DAC experiments' technique and methodology and the studies of fundamental properties of materials at extreme conditions. The laser-heating setup, first developed for high-temperature experiments at multi-megabar pressures, has found an important application for deriving the EOSes of amorphous materials with high accuracy on in-house facilities.

Acknowledgments

This dissertation is one of the results of my four-year adventure, and there is no real adventure to be undertaken alone. I was a newcomer to this field of knowledge before arriving at Bayreuth, the only thing I had was my willingness to learn and the people around me created an excellent environment for that. The smallest I can do is to show my gratitude to everyone who supported and inspired me over my scientific path and had direct or indirect contributions to the presented thesis.

First, I would like to thank my supervisors Prof. Dr. Natalia Dubrovinskaia and Prof. Dr. Leonid Dubrovinsky for their guidance, support, patience, and the best working environment I can imagine.

I would like to thank all the members of the Laboratory of Crystallography, where I spent a major part of my time, for a warm and friendly atmosphere. Special thanks to Prof. Dr. Sander van Smaalen and Dr. Andreas Schönleber for support and helpful discussions on the laboratory seminars, the laboratory secretary Denise Kelk-Huth who helped not to drown in the administrative problems and questions, and my office-mate Kerstin Kuspert for her willingness to help me in any situation and the good time we shared. I am truly grateful to Dr. Kirsten Schulze for translating the abstract of this thesis into German.

I have spent a lot of my working time doing experiments in BGI and would like to thank everyone there for providing me excellent environment for collaborative work. Especially Prof. Hans Keppler, Prof. Tomoo Katsura, Prof. Dan Frost. I would like to thank the administrative and technical staff of BGI Petra Buchert, Janina Potzel, Nicole Fischer, Stefan Übelhack, Detlef Krausse, Dr. Stefan Keyssner, Sven Linhardt, Raphael Njul, Trenz Ulrike for their help in corresponding problems.

Many of my experiments were performed on the synchrotron beamlines of ESRF and DESY and I would like to acknowledge their staff for support and assistance. Especially Konstantin Glazyrin,

Michael Hanfland, Hanns-Peter Liermann, Alexander Chumakov, Pavel Sedmak, and Valerio Cerantola.

There are no words that can express all of my gratitude to my friends and comrades: Egor Koemets, Iulia Koemets, Artem Chanyshev, Dmitry Druzhbin, Alexander Kurnosov, Stella Chariton, George Aprillis, Sumith Abeykoon, Anna Pakhomova, Maxim Bykov, Elena Bykova, Denis Vasiukov, Daniil Kudryavtsev, Dominique Laniel, Dmitry Bondar, Giacomo Criniti, Serena Dominijanni, Sylvain Petitgirard, Alena Aslandukova, Andrey Aslandukov. Thank you all for the time we spent together, your kindness and help, for the knowledge you gave me, and skills you helped me to receive, days and nights we shared on the beamlines, hundreds of liters of beer we drank together, and everything good what happened with me over this four years.

I would like to thank my father, Michail Fedotenko, my grandparents Alexander and Alexandra Fedotenko for their endless love and for guiding me on my first, but important steps. I would like to thank my first mentors Prof. Dr. Vladimir Pai and Dr. Andrey Plastinin for their guidance in both scientific and human aspects.

In the end, I would like to express my special gratitude to the person with many names: the best friend, colleague, and one who became my wife, Saiana Khandarkhaeva, thank you for always being on my side.

Table of Contents

1.Introduction

Modern science and technology are two complex, multifaceted, and closely related categories of human activities. Science creates the base of knowledge and ideas for technology. In turn, the impact of technology on science is, at least, equal. It provides the source of otherwise unavailable tools and methods that are necessary to address more complicated scientific problems efficiently. Furthermore, technology is a fruitful source of novel scientific questions itself. High-pressure science is a good example of such fusion between science and technology. It has been heavily experimental since the first high-pressure experiments at the end of the 19th century and remains the same nowadays. Modern high-pressure science relies on advanced instrumentation and analytical techniques presented on large-scale facilities, such as synchrotrons or free-electron lasers.

Pressure and temperature are fundamental thermodynamic variables and, therefore, largely determine the state of the system. Expanding of accessible pressure and temperature limits is the most naturally applicable for geo- and planetary sciences (it allows simulating otherwise inaccessible conditions of the Earth's and other extrasolar bodies interiors (Dubrovinskaia et al., 2016; Tateno et al., 2010)) but also founds many applications in material science, chemistry, and solid-state physics: for example to discover novel functional materials (L. S. Dubrovinsky et al., 2001), high-pressure superconductivity (Drozdov et al., 2015), and new phases/compounds (Zhang et al., 2017).

The generation of high pressures is a tradeoff between the highest achievable pressure and the size of the sample. There are two major principles of generation static high-pressure conditions: one can either increase the applied force or reduce the area where the force is applied. The first approach is implemented in the design of such devices as piston cylinder apparatuses and multi anvil presses (Kawai and Endo, 1970). They are mostly focused on maximizing applied force on

relatively large samples (approximately 0.1 - 3 mm in linear dimensions). These devices are routinely used for experiments with pressures up to 30 GPa and coupled with resistive heating that allows reaching temperatures up to ~2500K (Shatskiy et. al., 2011). The opposite approach is decreasing the sample dimensions to a micrometer scale, which is presented in diamond anvil cell devices (described in detail in section 3.1.1). The invention and technical development of the diamond anvil cell (DAC) technique (Basset, 2001) allowed to significantly enlarge accessible thermodynamic space in high-pressure studies. DAC technique has evolved into a powerful and routine experimental method at in-house laboratories and synchrotron beamlines and many scientific breakthroughs have been achieved in the last decades. DACs are routinely used for experiments up to 200 GPa, however, the size of the studied sample decreases dramatically with the raise of pressure. In a typical experiment at 200 GPa, the size of the studied sample is usually less than 5 μm.

There are two major approaches for the generation of high temperatures in diamond anvil cell experiments: resistive (Dubrovinskaia and Dubrovinsky, 2003; Zha and Boehler, 1985; Zha et al., 1986) and laser heating (LH). In the first case, diamonds with the gasket assemblage are surrounded by the external electrical resistive heater which provides homogeneous temperature distribution within the sample chamber. However, the maximum temperature is limited by the graphitization temperature of a diamond (1200 °C, in the inert atmosphere). Exotic internal resistive heating (where the micro heater is placed inside the DAC sample chamber) (Boehler et al., 1986; Liu and Bassett, 1975; Zha and Bassett, 2003) expands the maximum temperature up to 3000 K, but makes the preparation of the DAC extremely challenging and time-consuming.

The technique of laser heating takes advantage of the transparency of a diamond in a wide spectral range of electromagnetic radiation and allows achieving significantly higher temperatures. The laser beam is focused on the sample placed inside the DAC and easily heats it up to several thousands of degrees Kelvin. Obviously, different materials absorb the laser radiation differently, and the absorption capability of the sample starts to play a significant role in the laser heating experiments. This problem is partially solved by using laser sources with different wavelengths depending on the studied material. Most metals and compounds non-

transparent in visible light are usually heated using near-infrared (NIR) fiber and solid-state Nd-doped YAG lasers with a central wavelength of around 1060 nm (Basset 2016).

High power CO_2 infrared (IR) lasers with a central wavelength of around 10 μm are usually utilized for heating of wide range of materials such as non-metallic compounds or materials transparent in the visible light. Metals also absorb infrared radiation well and can be heated with such types of lasers. However, the high wavelength of IR lasers restricts the focusing of a laser beam. Moreover, optical components for 10 μm IR lasers are much more expensive and less functional compared to those for NIR.

Another drawback of laser heating compared to resistive heating is the less accurate temperature determination. Contrary to direct temperature measurements by a thermocouple placed close to the sample in resistive heating experiments, laser heating relies on spectroradiometry as a major method (Shen et al., 2010). This method is based on the fitting of the thermal radiation spectrum emitted by the heated sample to the Planck grey body radiation function. Therefore, it allows measuring only the highest temperature on the surface of the sample (Campbell et al., 2007). The uncertainty in the temperature measurements using spectroradiometry is affected by optical distortion introduced by different optical components of the LH setup. Particularly, chromatic distortions cannot be compensated well on the stage of thermal emission spectra processing or laser heating setup calibration (Marini et. al., 2013). They should be minimized through a proper choice of optical system design and the use of optical elements with chromatic corrections. The typical value of uncertainties in the temperature measurements at 2000 K is of the order of ±100 K, and at 5000 K it is of about ±500 K which is acceptable for most of high pressure experiments.

Despite the drawbacks, laser heating diamond anvil cells is the only method to generate temperatures above 3000 K in static high-pressure experiments, and has become very important for high-pressure chemistry, mineral and solid-state physics, Earth and material sciences (Bassett, 2016, 2001). Over the last decades, it has been coupled with many other analytical methods such as X-ray diffraction (Meng et al., 2015; Schultz et al., 2005), Nuclear Inelastic Scattering (NIS), the Synchrotron Mössbauer Source (SMS) (Kupenko et al., 2012; Lin, 2004), and X-ray Absorption Near-Edge Structure spectroscopy (XANES) (Aquilanti et al., 2009; Marini et al., 2013) and many

of high-pressure synchrotron beamlines dedicated to DAC are equipped with laser heating systems.

Laser heating experiments at multi-megabar pressures are especially challenging due to the extremely small size of the studied samples and, therefore, require an individual approach in the design of the laser heating system and the heating process itself. Such parameters as the high optical magnification of the laser heating system, quality of the observed image and deep focusing of the laser beam become extremely important. The present thesis focuses on the development of advanced laser heating for the multi-megabar pressure range. The developed system has been applied to the synthesis and study of materials relevant to Earth and material sciences at pressures up to 180 GPa, Pd and Ni carbides. Moreover, fascinated by the quality of the microscopic images obtained through the observation path of the laser heating system, we have developed the method for the study of the equation of state of amorphous materials based on high-resolution optical microscopy.

1.1. The scope of the thesis

In the course of the presented thesis, we have done both: extended the methodology of diamond anvil cell experiments and applied it for material and geo sciences problems. In particular, we have developed a new laser heating system for ultra-high pressure DAC experiments (section 5.A) and utilized it in combination with different analytical techniques. In the second study, we have designed a method for studies of the compressibility of amorphous materials (Section 5.B) using high-resolution optical microscopy and demonstrated its application to materials science problems. In two studies we investigate the synthesis and study of novel transition metal carbides relevant to the materials science (section 5.C) and Earth's sciences (section 5.D).

1.1.1. Development of the Laser heating system for ultra-high pressure experiments

Laser heating (LH) in diamond anvil cells (DACs) has been used for more than five decades (Bassett, 2016). There are many examples of its applications in geosciences for simulating the

conditions of deep Earth's and planetary interiors, studies of physical and chemical processes at extreme conditions, and synthesis of novel materials (Lavina et al., 2011; Liu, 1974; Mao et al., 2005; Meng et al., 2015; Zhang et al., 2014). The methodology of laser-heated diamond anvil cells (LHDAC) is well described in the literature (Boehler et al., 2009). Over the last decade, this technique has evolved into a useful and routine experimental method at synchrotron beamlines and has been coupled with various analytical techniques: powder and single crystal X-ray diffraction (Mezouar et al., 2007), X-ray Absorption spectroscopy (Aquilanti et al., 2009; Marini et al., 2013), nuclear inelastic scattering (Lin, 2004), and Synchrotron Mossbauer spectroscopy (Kupenko et al., 2012).

Dynamic development of the LHDAC technique during recent years has resulted in the emergence of portable laser heating systems which can be used for in house experiments in different scientific environments (i.e. simultaneously with resistivity measurements, Raman or Brillouin spectroscopy, X-ray diffraction, etc.), easily moved between synchrotron beamlines and coupled with different analytical techniques. The first portable laser heating systems were introduced in 2009 by Boehler (Boehler et al., 2009) and Dubrovinsky (Dubrovinsky et al., 2009). Both setups were successfully used for in-house and synchrotron *in situ* experiments. However, single side LH (Dubrovinsky et al., 2009) limits the application due to large temperature gradients within the samples. The system presented by Boehler (Boehler et al., 2009) does not allow simultaneous X-ray diffraction and temperature measurements.

The designs of the double-sided LH systems based on universal laser-heating heads (UniHeads, adapted finite cutting laser heads produced commercially by Precitec GmbH & Co. KG) (Kupenko et al., 2012; Aprilis et al., 2017), enable to decrease the size of a laser heating setup. The setups (Aprilis et al., 2017; Kupenko et al., 2012) are simple to install and can be used in experiments that require the rotation of DACs during data collection (particularly, for single-crystal XRD in laser-heated DACs). The UniHead-based LH setups allow varying the size of the laser beam from 15 to 50 μm FWHM and providing 20-time magnification of the samples in DACs, which is sufficient for the majority of conventional experiments with laser heating. However, the modern trend on the extension of pressure range in DAC experiments to multimegabar has naturally

resulted in a dramatic decrease of the sample dimensions and corresponding challenges for its laser heating.

The size of the studied sample in LHDAC experiments at 100 GPa is usually smaller than 15 μm, while at pressures above 200 GPa samples, as a rule, are about 3-4 μm in diameter. Thus, for precise heating of such small samples, it is necessary to localize the high-temperature zone and avoid heating of the gasket/pressure calibrant materials present in the sample chamber. Therefore, tight focusing of the laser beam, high optical magnification, and resolution are necessary. This part of the thesis project was aimed to design a new laser heating setup for DAC experiments at the multimegabar pressure range.

1.1.2. Determination of Equation of state of amorphous solids by optical microscopy measurements

Elastic properties of materials define the structural and electronic response of the system to applied stress that strongly depends on the nature of interatomic interactions. This makes knowledge of the elastic properties of materials as a function of pressure and temperature indispensable in materials science. The equation of state (EOS) of a system defines the relationship between the thermodynamic variables, such as volume (V), pressure (P), and temperature (T), through the bulk modulus and the thermal expansion coefficients. At a constant temperature, pressure-volume relations of a solid can be described by different types of analytical EOSes(Birch, 1947; Vinet et al., 1987), involving the isothermal bulk modulus ($K_0 = -V \cdot \left(\frac{\partial P}{\partial V}\right)$) and its pressure derivatives ($K' = \partial K/\partial P$) at zero pressure.

Investigating the EOSes of materials under pressure, require subjecting them to extreme conditions. X-ray diffraction (XRD) in DACs is the most common technique for deriving EOSes of crystalline materials through measuring the unit cell volume of a sample as a function of pressure, but it is not applicable to amorphous and glassy materials due to the presence of topological and chemical disorder (Yonezawa and Ninomiya, 1983). This explains why EOSes of crystalline materials have been well studied, but so far little is known about P-V relations for non-crystalline matter (melts, metallic glasses, and other amorphous solids and nanocrystalline ceramics). These

materials are currently at the focus of solid-state physics, chemistry, materials science, and geophysical research communities. In geosciences, glasses are considered as proxies for silicate melts whose properties are of great importance, as they control magmatic and volcanic activity and therefore play a central role in determining the chemical and physical evolution of the Earth throughout geologic time (Kushiro, 1976; Mysen and Virgo, 1994). Studies of the compressional behavior, local structures, and densification mechanisms of silicate glasses at deep mantle conditions can shed light on the dynamics of the Earth's interior, which is still insufficiently understood (Lee et al., 2005).

Elastic properties of both crystalline and amorphous materials can be studied *in situ* in DACs by utilizing such methods as X-ray absorption (Petitgirard et al., 2019), Brillouin scattering (BS) (Ko et al., 2017), ultrasonic measurements (US) (Jacobsen, 2002; Jacobsen et al., 2004), impulsive stimulated scattering (ISS) (Brown et al., 1989), inelastic X-ray scattering (IXS) (Fiquet et al., 2004)**,** or by determining strain-stress relations using optical microscopy (Amin et al., 2012; Scott and Jeanloz, 1984). The sample density (and hence the EOS) can be obtained from high-pressure X-ray absorption measurements (Katayama et al., 1998, 1996), but this method is hard to apply in DACs and it works reasonably well only for materials containing heavy elements (i.e. good X-ray absorbers).

Determination of the strain-stress relations using optical microscopy (Amin et al., 2012; Scott and Jeanloz, 1984) requires measurements of the dimensions of an object observed under the high-resolution optical microscope. The technique for studying EOS through the sample length determination in DAC using an image shearing device (Dyson, 1960) was firstly presented by Scott and Jeanloz (1984),s who reported the precision of measurements of about 0.065 μm (for the samples with the linear size of around 100 μm) and validated the technique through determining the EOS of Au. Deriving the EOS of GeO_2 glass up to 12 GPa through the optical microscopy measurements was reported by Smith et al (1995). In 2012, a partially automatized algorithm for determination of EOSes through high-resolution optical microscopy have been firstly described (Amin et al., 2012). The methodology relied on two-dimensional image acquisition and its subsequent analysis to quantify changes in the sample surface area. The authors applied the Canny edge detection algorithm (Canny, 1986) to define the sample boundaries and calculate its

surface area. The method was applied to study the EOS of As_2O_3 and $GeSe_2$ glasses, and amorphous red phosphorus at pressures up to 10 GPa. However, Amin et al. (2012) stated higher experimental uncertainties if compared to the method of Scott and Jeanloz (1984). The lower precision of the partially automatized measurements of Amin et al. (2012) could be potentially explained by applying Gaussian smoothing during the image processing with the Canny algorithm. Amin et al. (2012) chose samples of random shapes but applied smoothing algorithms, which blur out the corners and junctions, thus making it harder to detect their actual positions. Still, despite all obstacles, the method by Amin et al. (2012) performed reasonably well on several crystalline and amorphous compounds at pressures up to 12 GPa.

One of the major problems of the EOS measurements using optical microscopy is the high uncertainty in sample dimensions: the observed sample length/area is strongly affected by the focus position of the sample and the definition of the length relies on the subjective perception of the operator. In order to make the method reliable and accurate, the measurements have to be performed at the same focus position at each pressure point. Defining the focus point by eye is inaccurate. Therefore, to minimize subjective perception, fully automated experimental and data analysis procedures are required.

1.1.3. Synthesis of transition metal (Ni, Pd) carbides in laser-heated diamond anvil cells

Transition metal carbides are a large group of materials that possess outstanding physical and chemical properties such as high hardness and melting point, low compressibility, and high catalytic activity (Friedrich et al., 2011; Khandarkhaeva et al., 2020; Liang et al., 2000). The structure-property relation of transition metal carbides at pressures close to ambient have been intensively studied both experimentally and theoretically over the last decades (Friedrich et al., 2011; Singh et al., 2009; Yeung et al., 2016).

Studies of carbides at high pressure and temperature conditions in laser-heated diamond anvil cells are important not only for the synthesis of novel materials and investigation of their properties but also from a methodological point of view for understanding of underlying processes occurring during the laser heating. Diffusion of carbon from the diamond anvils to the

studied sample is possible and has been demonstrated in numerous experiments. In some cases, carbon contamination of the studied sample may be a reason for the large inconsistency in the experimentally measured melting curves of some materials. At the same time, the diamond anvil can be considered as a source of carbon for the synthesis of novel compounds in extreme conditions, and the studies presented in the following sections (5.C and 5.D) demonstrate that case.

1.1.3.1. Nickel carbide

Nickel is considered as the second most abundant element after iron in Earth's core (Birch, 1952; Prescher et al., 2015). Modern cosmochemical models and meteorite's studies propose that apart from Fe, the Earth's core contains up to 5 wt. % of Ni (Litasov and Shatskiy, 2016; McDonough, 2003) and, in the outer core, up to 10 wt. % of light elements (Poirier, 1994; Torchio et al., 2020; Wood, 1993). A significant amount of carbon in iron meteorites (Bashir et al., 1996), its high solubility in liquid Fe at high PT conditions (Hirayama et al., 1993; Wood, 1993), and high abundance of carbon in the solar system (Wood, 1993) imply that carbon is one of the most abundant light elements in Earth's core. Interest in the role of carbon in Earth's core geochemistry and mineralogy resulted in numerous high-pressure studies of the Fe-C system over the last decades. Such intermediate Fe-C compounds as Fe_3C and Fe_7C_3 were suggested to be the most likely candidates to the carbon-bearing phases in Earth's core, as they were found at relevant pressures and temperatures (Chen et al., 2014; Lord et al., 2009; Nakajima et al., 2009; Prescher et al., 2015; Wood, 1993). At room temperature Fe_3C was shown to be stable up to 187 GPa, however, it decomposes into a mixture of solid Fe_7C_3 and hcp-Fe at pressures above 145 GPa upon laser heating and transforms into Fe-C liquid and solid Fe_7C_3 at temperatures of above 3400 K (Liu et al., 2016). Moreover, the high Poisson's ratio of Fe_7C_3 at high pressures (Prescher et al., 2015) indicates that the presence of carbon may significantly affect the elastic properties of iron. This corroborates well with the Preliminary Reference Earth Model (PREM) (Dziewonski and Anderson, 1981), which suggests the material of Earth's inner core also has a high Poisson ratio.

Contrary to the binary iron-carbon system, the Fe – Ni – C, and Ni – C systems at high PT conditions are still poorly understood. Nickel can strongly modify the physical properties of pure Fe at elevated pressures and temperatures. Recent studies have shown that Ni alloying with Fe doesn't affect the melting temperature of Fe up to 100 GPa, however, modifies its phase boundary by shifting the hcp/fcc/liquid triple point to the higher pressure-temperature region (Torchio et al., 2020). For example, for Fe-20 wt.% Ni alloy the triple point was found to be at 170(20) GPa and 4000(400) K (Torchio et al., 2020) as compared to 100(10) GPa and 3500(200) K for pure Fe (Morard et al., 2018). Pressure-induced Invar effect in Fe-Ni alloys was reported by Dubrovinsky et al. in 2001. The thermal expansion of the alloys $Fe_{0.55}Ni_{0.45}$ and $Fe_{0.20}Ni_{0.80}$ was found to be extremely low in the temperature interval of 291 K to 500 K at pressures of 7.7 and 12.6 GPa, correspondingly (L. Dubrovinsky et al., 2001). It was also proven that alloys of Fe with Ni have significantly higher strength in comparison with pure Fe (Reagan et al., 2018). The mineral cohenite, $(Fe, Ni)_3C$, which is isostructural to Fe_3C, was found in iron meteorites (Brett, 1966) and predicted to be stable at high pressures (Ringwood, 1960), however, a pure-Ni end-member of solid solution, cementite-type phase (Ni_3C) has never been reported.

Understanding the properties of the Earth's outer core relies on knowledge of its composition. Therefore, the synthesis of novel Earth-related materials and the study of their properties are of great interest of fundamental geoscience. Particularly, studying of Ni-C system helps to understand both: chemical distribution of carbon in the Earth's core and the influence of carbon alloying on the elastic properties of the core itself.

1.1.3.2. Palladium carbide

Palladium is a transition metal well known for its exceptional ability to absorb hydrogen in a bulk (Adams and Chen, 2011; Manchester et al., 1994a). Moreover, palladium is one of the preferred catalysts for the hydrogenation of hydrocarbons in a petrochemical industry (Borodziński and Bond, 2006; Lazzarini et al., 2016; Pellegrini et al., 2011; Teschner et al., 2008). Thus, studies of palladium hydrides and carbides are of technological importance: their formation in palladium nanoparticles-based catalysts can significantly affect the activity and selectivity of the catalysts (Teschner et al., 2010; Tew et al., 2012).

Palladium hydride was found to exhibit superconducting properties (Tc = 8-10 K) (Skoskiewicz, 1972; Stritzker and Buckel, 1972) that stimulated intensive studying of the Pd-H and Pd-D systems at extreme conditions (Brownsberger et al., 2017), while the behavior of the Pd-C system at high pressures has not been studied so far.

Synthesis of PdC_x at ambient pressure was firstly demonstrated by Cadevill and Lerner (1976). PdC_x compound was synthesized by melting a mixture of palladium and graphite powders in an induction furnace under an argon atmosphere. However, the solubility of carbon in the palladium bulk was found to be extremely low (below x = 0.03). The higher carbon content (x = 0.13(5)) was reported in palladium carbide nanoparticles synthesized from palladium nanoparticles deposed on a carbon substrate (Bugaev et al., 2017). At a temperature of 400 K in acetylene and hydrogen atmosphere, either hydrides or carbides formed depending on the partial pressure of hydrogen and acetylene (Bugaev et al., 2017).

The material science part of this Ph.D. project aimed to conduct the synthesis of carbon-rich palladium carbide in laser-heated diamond anvil cells and complement the study by investigating its physical properties using *in situ* synchrotron X-ray diffraction.

1.2. Summary of the aims of the thesis project

- The methodological part of this Ph.D. project was divided into two parts. The first part was aimed to develop a new laser heating setup for ultra-high pressure diamond anvil cell experiments and test it for materials science and geoscience applications. The second part aimed to develop a new method to study the equation of state of crystalline and amorphous solids in diamond anvil cells using advanced optical microscopy and test it on examples interesting for materials science applications.
- The scientific case for the first application of laser-heating setup was the study of the behavior of the Ni-C system at pressures above 150 GPa. This part of the work has direct implications for the mineralogy and geochemistry of Earth's core.
- The material science part of this project aimed to conduct the synthesis of carbon-rich palladium carbide in laser-heated diamond anvil cells and to investigate its compressibility using *in situ* synchrotron X-ray diffraction.

2.Methods

This chapter describes major experimental techniques used in this thesis: the generation of high pressure and temperature conditions, Raman spectroscopy, and X-Ray diffraction.

2.1. Generation of high pressures

Pressure is one of the fundamental thermodynamic variables and therefore *in situ* study of the sample at non-ambient pressure conditions is of great importance for geo and material sciences. It enables the discovery of novel materials and unknown physical properties as well as the simulation of the interiors conditions of Earth and planetary body. Pressure (P) is the force exerted over a surface per unit area and expressed by the following formula:

$$P = \frac{F}{A} \qquad \text{Eq. (2.1.1)}$$

where F is the force applied to the normal of surface area and A is the area of that surface. According to this relation, to generate high pressures, it is necessary either to decrease the area to which external force is applied, or increase the force itself. These principles were implemented in the design of many high-pressure devices over the last decades. For example, piston-cylinder apparatuses and multi-anvil presses (Kawai and Endo, 1970) are large/massive devices in significant degree focused on maximizing of applied force on relatively large samples (approximately 0.1 - 1 cm in linear dimensions). The opposite approach is decreasing the sample dimensions to micrometer sizes is implemented in diamond anvil cell devices and found to be applicable for generation of significantly higher pressures up to 1 TPa (Dubrovinskaia et al., 2016).

2.1.1.Diamond anvil cells

The diamond anvil cell (DAC) is a very powerful technique introduced by Valkenburg et al. in 1959 (Valkenburg et al., 1959). The transparency of the diamond in a wide range of electromagnetic radiation makes the DAC one of the most valuable tools for studies of materials under extreme

conditions using different emission, scattering, and absorption methods. The basic principle of the pressure generation in DAC is the compression of the material between the flat tips (culets) of two gem-quality diamond anvils precisely driven against each other.

Many different DAC designs were invented over the last decades, but the basic idea remains the same, and different DAC types are sharing the same principle features. The common DAC (figure 2.1) consists of the metal body with a couple of seats, diamond anvils, precisely positioned on them, and the metal gasket with a circular hole placed between that anvils.

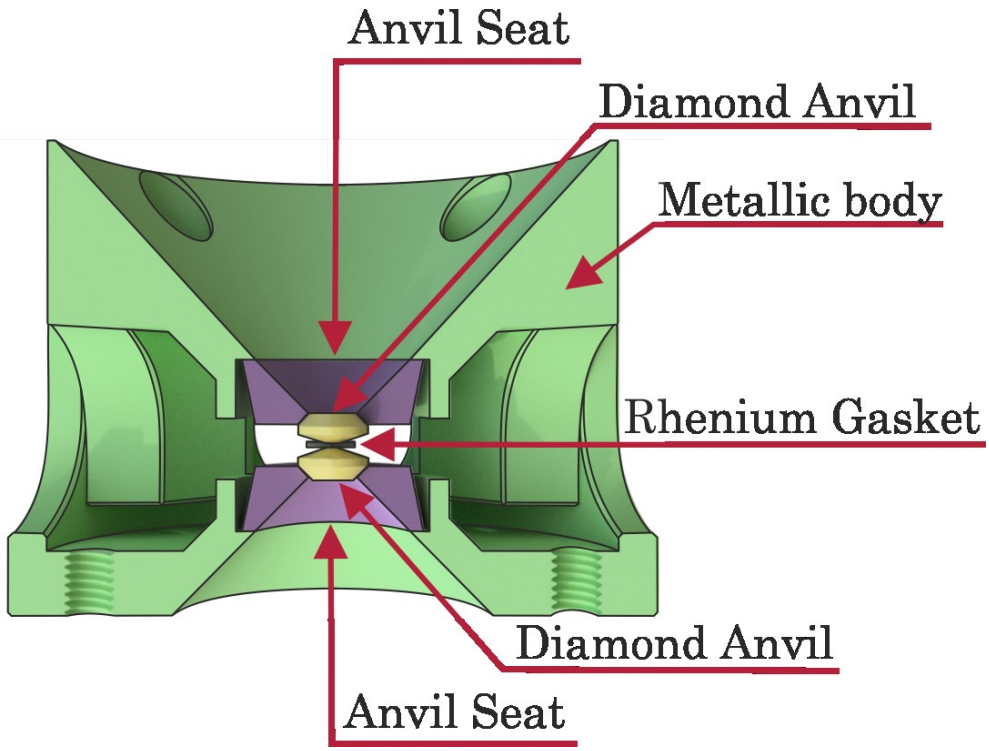

Figure 2.1. Schematic diagram of BX90-type DAC (Kantor et al., 2012).

Seats are commonly made out of hard materials (such as tungsten carbide) and serve to transfer the load from the external metallic body onto the diamond anvils. The metal gasket with a circular hole compressed between the diamond tips forms the cylindrical space (figure 2.2) that allows confining the sample position over the compression and redistribute uniaxial stress when filled with (soft) pressure-transmitting medium. Many materials can be used as a gasket, however, rhenium is one of the most common due to its exceptionally elastic properties such as low brittleness, relatively high hardness, and chemical inertness at ambient temperature.

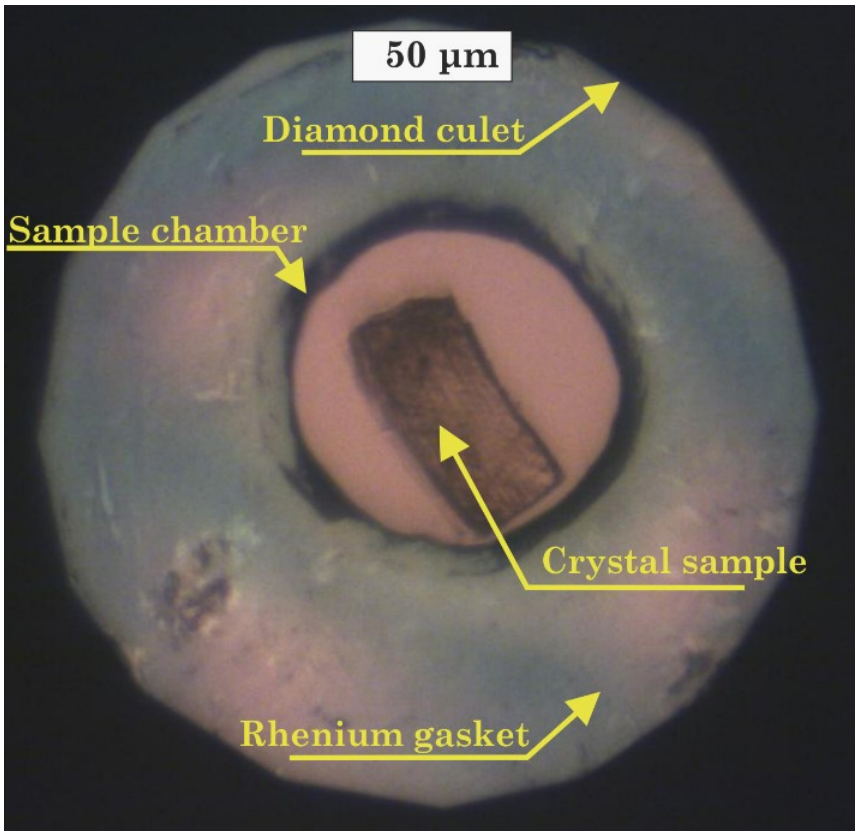

Figure 2.2. A microphotograph of the DAC sample chamber was taken under an optical microscope through the diamond anvil (top view). The culet diameter is 250 µm.

The diamond anvil is an essential part of the DAC. The size of the anvil culet can vary from about a millimeter to tens of micrometers and mainly determines the maximum achievable pressure. Smaller culets usually have a beveled shape (figure 2.3) and allow reaching higher pressure, however, they restrict the size of the studied sample.

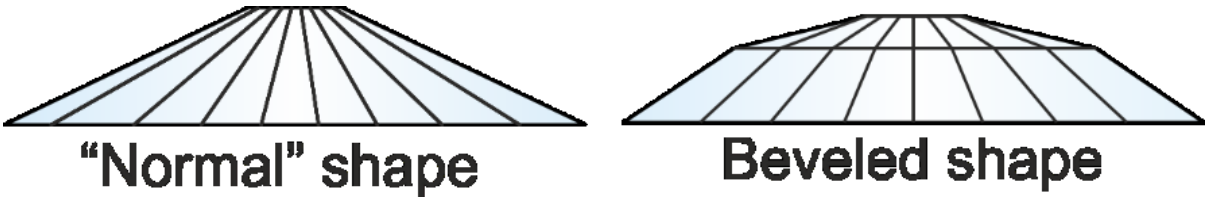

Figure 2.3. Examples of the culet shapes. Diamonds with culets diameter below 150 µm are usually beveled.

In turn, the combination of the geometrical shape of the diamond cut, the shape of the seat, and the aperture of the metallic body are crucial parameters. In spectroscopic experiments, where the position of the DAC remains stationary over the measurements, standard brilliant cut anvils (figure 2.4 (a)) and seats are common. For experiments where sample rotation is required, such as X-ray diffraction, large aperture Boehler-Almax diamond anvils and seats (figure 2.4 (b)) are necessary.

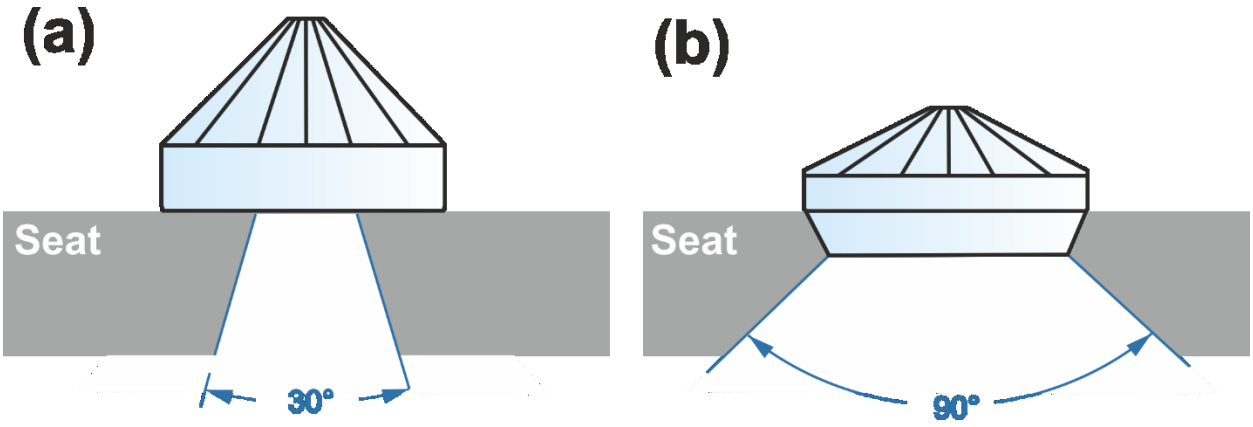

Figure 2.4. Different types of diamond anvils and seats. (a) Standard brilliant-cut diamond and seat for spectroscopic measurements; (b) Boehler-Almax designed diamond and seat for X-ray diffraction experiments.

For the purposes of the thesis, we used BX90 type DACs (Kantor et al., 2012). Diamonds with different culet diameters (80 to 250 µm) were: of large aperture Boehler-Almax design (Boehler and De Hantsetters, 2004) for X-ray diffraction experiments and of brilliant-cut standard design for optical measurements. The choice of the culet size depends on the desired pressure range. We used anvils with 250 µm culet diameters for experiments at pressures 75 GPa, 120 µm - below 120 GPa, and 80 µm culets to generate pressures up to 190 GPa.

2.1.2. Pressure transmitting media

By default, the DAC is a uniaxial compression device. Uniaxial compression of the sample results in high shear strains and doesn't give access to pressure as a thermodynamic variable (pressure is thermodynamic variable only in the assumption of hydrostatic conditions). To transmit the uniaxial stress from the diamond anvil to the sample and achieve (quasi-) hydrostatic conditions

and homogeneous pressure distribution, pressure transmitting media are used (figure 2.5). The pressure transmitting media (PTM) fill the sample chamber and surround the sample helping to make the stress quasihydrostatic. Any known liquids (including alcohol mixtures and paraffin oil) solidify at ambient temperature at pressures exceeding ~15 GPa. To serve well, solid PTM should be materials with relatively low bulk and shear modulus and ultimately low tensile strength.

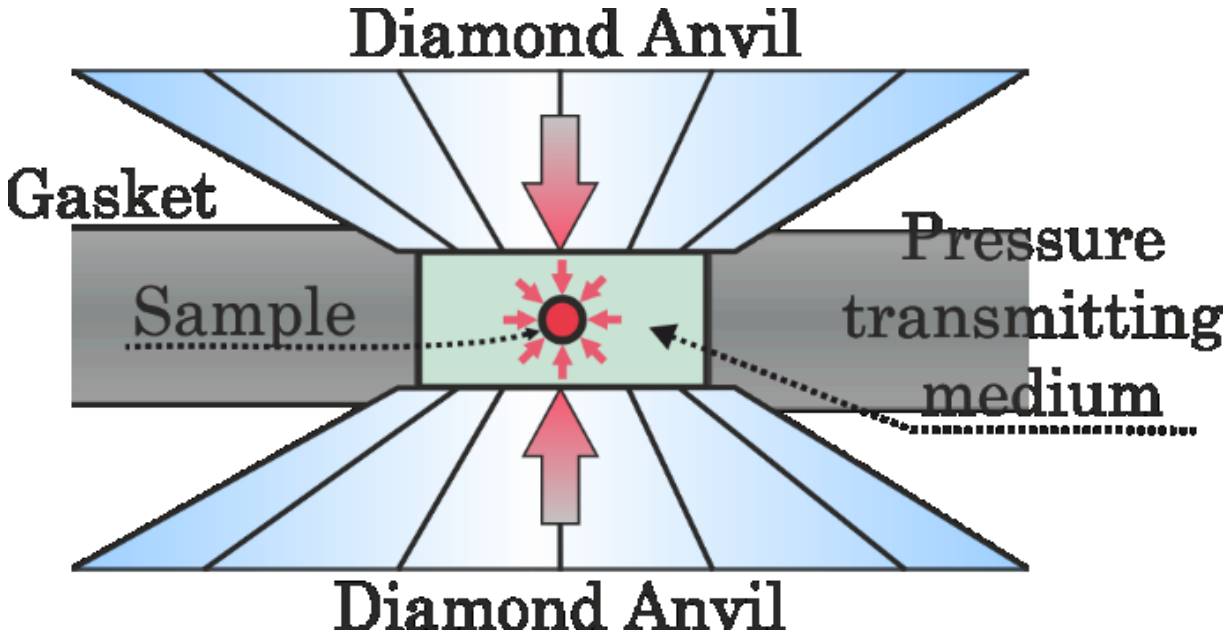

Figure 2.5 Schematic representation of stress distribution in DAC. Red arrows designate vectors of applied stress.

Some materials such as solid noble gases (He, Ne, Ar), and to a certain degree some alkali metal halides satisfy this criterion and can be used. In addition to uniform pressure distribution, PTM often play the role of a pressure gauge (Ne, Ar), the reactant in chemical reactions under extreme conditions (paraffin oil, O_2, N_2), or acts as a thermal insulation layer between sample and diamond surface during laser heating experiments (NaCl, KCl, LiF). The gases can be loaded into the DAC sample chamber using high-pressure gas loading apparatus (Kurnosov et al., 2008) or cryogenically, whereas solids and liquids PTMs (at atmospheric pressure) can be loaded manually. In this thesis different PTM were used: He and Ne loaded at ~1.2 kbar for precise measurements of the equations of state, NaCl and LiF for thermal insulation of the samples, and paraffin oil as a source of hydrogen for chemical reactions.

2.1.3. Pressure determination

In situ determination of the pressure inside the DAC sample chamber is a crucial point in any DAC experiment. The common methods are based on the use of different pressure calibrants. The material with a well-known response on applied pressure can be loaded into the DAC along with the sample and probed by analytical techniques. Pressure dependence of the ruby (Cr-doped Al_2O_3) fluorescence is the most common technique in a pressure range up to 100 GPa (Syassen, 2008).

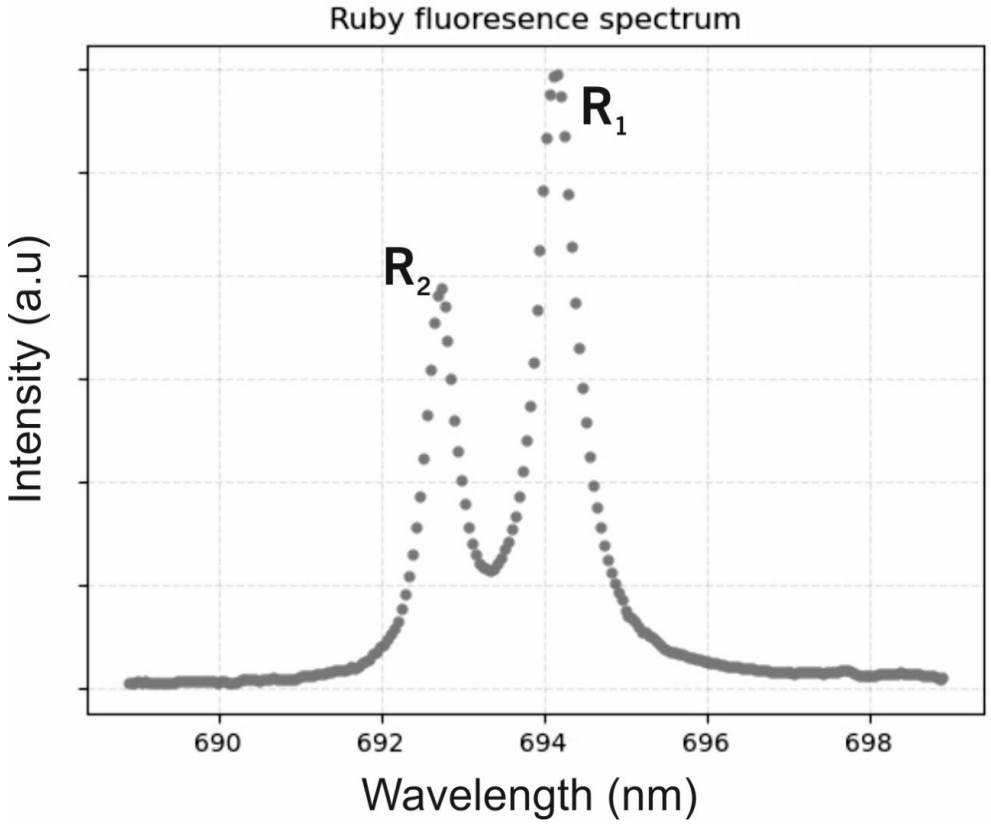

Figure 2.6. Typically ruby fluorescence spectrum.

The microsphere of a ruby is placed in the DAC sample chamber along with the sample and pressure medium. Probing of the ruby with the laser light induces its fluorescence, which can be observed using an optical spectrometer. The following equation describes the relationship between the central position of the ruby R1 spectral peak with pressure (Shen et al., 2020):

$$P(GPa) = A\frac{\Delta\lambda}{\lambda_0}\cdot\left[1 + B\cdot\left(\frac{\Delta\lambda}{\lambda_0}\right)\right] \qquad \text{Eq. (2.1.3.1)}$$

where A and B are the calibration constants (A=1.87(1)·103, B=5.5) and λ_0 is the position of R1 peak (figure 2.6) at ambient pressure, and $\Delta\lambda$ is the shift of R_1 peak at pressure P relative to λ_0. With the increase of pressure, the intensity of the ruby fluorescence signal dramatically decreases and is absent at pressures above 100 GPa. The ruby placed inside the DAC sample chamber can potentially be involved in chemical reactions and result in contaminations, especially in high-temperature experiments. Therefore, in our work, we used the ruby fluorescence technique only in ambient temperature experiments.

The pressure dependence of the first-order Raman mode of a diamond culet is an alternative method of spectroscopic pressure determination (Akahama and Kawamura, 2006). At the center of the culet, normal stress is known to correlate with the high-wavenumber edge of the Raman band in the following way:

$$P(GPa) = K_0\left(\frac{\Delta v}{v_0}\right)\left[1 + \frac{1}{2}(K' - 1)\left(\frac{\Delta v}{v_0}\right)\right] \qquad (2.1.3.2)$$

Where $K_0 = 547$ GPa and $K_0' = 3.75$ are calibration constants, v_0 is the position of the high-wavenumber Raman edge at ambient pressure and Δv is the difference in its positions at ambient and measured pressures. The position of the edge is defined as a local minimum of the first pressure derivative from the Raman spectra (figure 2.7). This method is less accurate compared to measurements of Ruby fluorescence due to its empirical nature, uncertainties introduced by focusing and positioning of the probing laser beam on the culet face surface. However, it is still preferable in experiments in a pressure range above 100 GPa or in the case of ruby is not desirable.

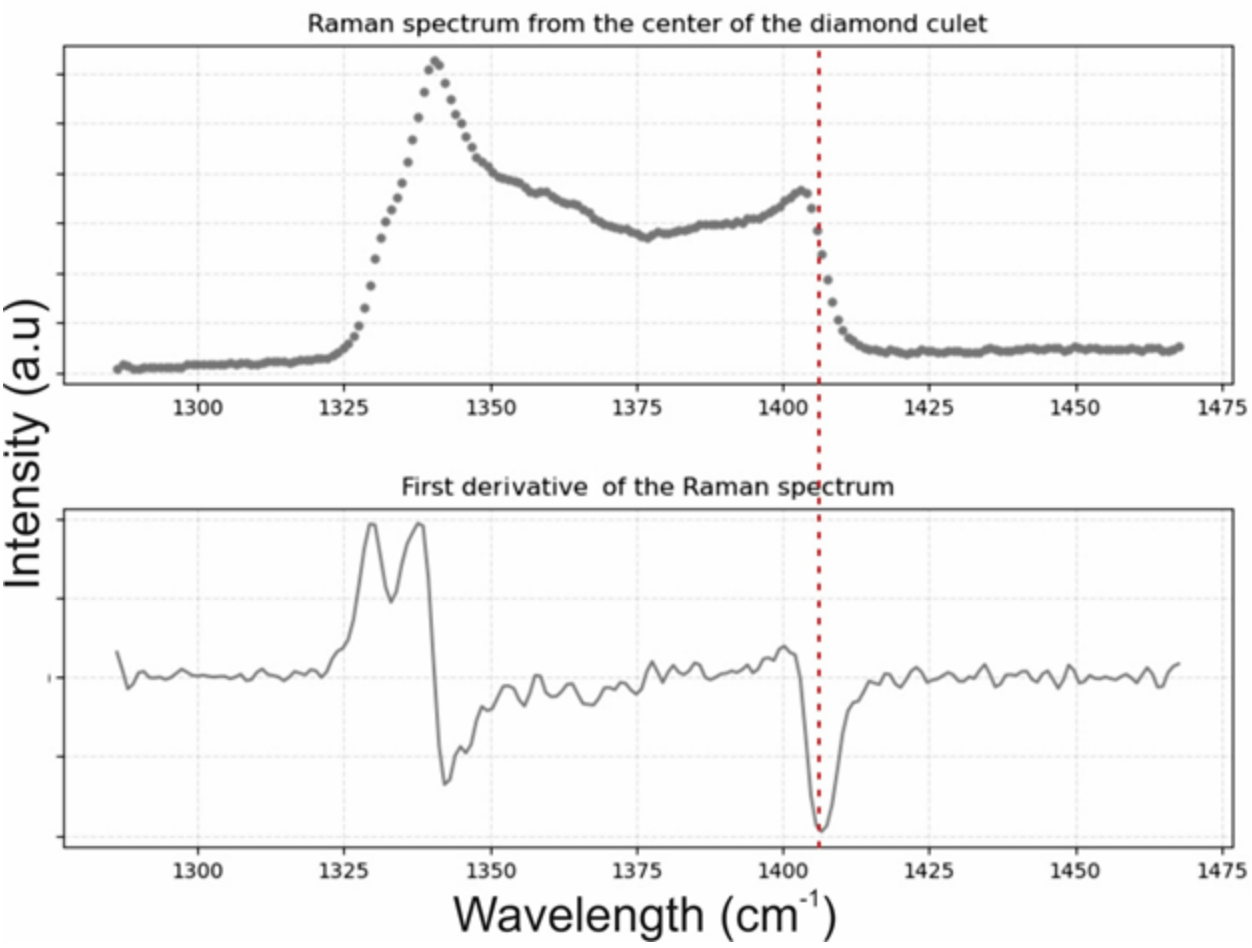

Figure 2.7. Typical Raman spectrum of the diamond anvil under applied stress and its first pressure derivative. The red dashed line indicates the position of the high-wavenumber edge.

In-situ X-ray diffraction is the most precise technique for pressure determination. The small amount of pressure calibrant with the well-known equation of state (EOS) can be loaded into the DAC along with the sample and probed by X-ray diffraction. That allows determining the unit-cell parameters of the calibrant accurately resulting in high precision in pressure determination. Calibrants are usually chemically inert compounds with high crystal symmetry (such as Au, Pt, W, sometimes Re) (Dewaele et al., 2008b; Dorogokupets and Dewaele, 2007; Fei et al., 2007). The absence of the pressure-induced phase transitions is desired in the pressure regions of interest. Using the PTM as a pressure marker by itself is an alternative way: solids like Ne, Ar, NaCl, KCl, LiF, KBr, and MgO (Dewaele et al., 2012, 2008a; Tateno et al., 2019; Ye et al., 2018; Zhang et al., 2014) have well-established equations of state in a wide range of pressures.

The equation of state of a system defines the relationship between the thermodynamic variables: volume (V), pressure (P), and temperature (T) through the bulk modulus and thermal expansion. At constant temperature, pressure-volume relations of matter can be described by different types of analytical EOSes (Birch, 1947; Vinet et al., 1987), if the bulk modulus ($K_0 = -V \cdot (\partial P/\partial V)$) and its pressure derivatives (particularly, $K' = \partial K/\partial P$) are known. The third order Birch-Murnaghan EOS is one of the most common in high-pressure science and we widely used it in our experiments:

$$\mathrm{P} = \frac{3\mathrm{K}_0}{2} \cdot \left[\left(\frac{\mathrm{V}_0}{\mathrm{V}}\right)^{\frac{7}{3}} - \left(\frac{\mathrm{V}_0}{\mathrm{V}}\right)^{\frac{5}{3}} \right] \cdot \left\{ 1 - \frac{3}{4}(4 - \mathrm{K}') \cdot \left[\left(\frac{\mathrm{V}_0}{\mathrm{V}}\right)^{\frac{2}{3}} - 1 \right] \right\} \qquad Eq.\ (2.1.3.3)$$

2.2. Generation of high temperatures – laser heating in diamond anvil cells

Transparency of the diamond in a wide range of electromagnetic radiation is one of significant advantages of the DAC technique and makes an observation and probing of the sample easy. It allows a high-power laser beam to be focused on the sample, while diamond anvils remain safe (Bassett, 2016). The choice of laser wavelengths mostly depends on the absorption characteristics of the sample. CO_2-based infrared (λ = 10.6 μm) and Nd: YAG near-infrared lasers (NIR, λ ~ 1064 nm) are the most common in high-pressure science. Being close to the spectral region of visible light, NIR lasers are usually used for heating non-transparent materials such as metals, alloys, and various transition metal bearing oxides, while transparent materials are heated by CO_2 infrared laser.

Along with the high hardness, diamond has one of the best thermal conductivity among all materials found in nature. Intensive dissipation of the heat through the diamond anvil during laser heating is one of the major problems in DAC experiments. The temperature gradients along the compressional axis can be reduced by using double-sided laser heating systems, while the lateral gradients are usually reduced by shaping of the laser beam to a flat-top profile (Prakapenka et al., 2008). Insulation of the sample from the diamond anvil is the only method to achieve temperature stability during laser heating in DACs. Such solid compounds as NaCl, KCl,

KBr, LiF are often used as both pressure transmitting and thermal insulating media. In that case, the sample is loaded into the sample chamber being clamped between layers of insulation material forming a "sandwich" arrangement.

The development of a new laser heating setup for ultra-high pressure studies was one of the subjects of this Ph. D. project. A detailed description of the technique is provided in the section 5.A.

2.3. Raman spectroscopy

Raman spectroscopy is a technique based on the inelastic scattering of monochromatic radiation on the irradiated sample. The method found application in many scientific fields and provides information on the molecular vibrations and crystal structure.

While the scattering of the light with no loss of energy (elastic, Rayleigh scattering) is dominant, a part of the incident laser radiation can be scattered inelastically with loss (Stokes Raman scattering) or gain (anti-Stokes Raman scattering) in energy. Absorbing the incident laser photon, the molecule moves from the ground to an excited (so-called "virtual") energy level. The virtual level is unstable and thus molecule seeks to turn back into the ground state. Stokes Raman scattering corresponds to the case when the molecule absorbs the incident photon and moves into final state which is higher in energy than the initial state and emit lower energy photon. If the final state of the molecule is lower in energy than an initial state, the scattered photon will be shifted to higher frequency region (anti-Stokes Raman scattering, figure 2.8).

The intensity ratio between the Stokes and anti-Stokes scattering components depends on the population of vibrational levels described by Boltzmann’s law. Therefore, at ambient temperature, the Stokes component is dominant in the inelastic spectra and commonly the only one considered.

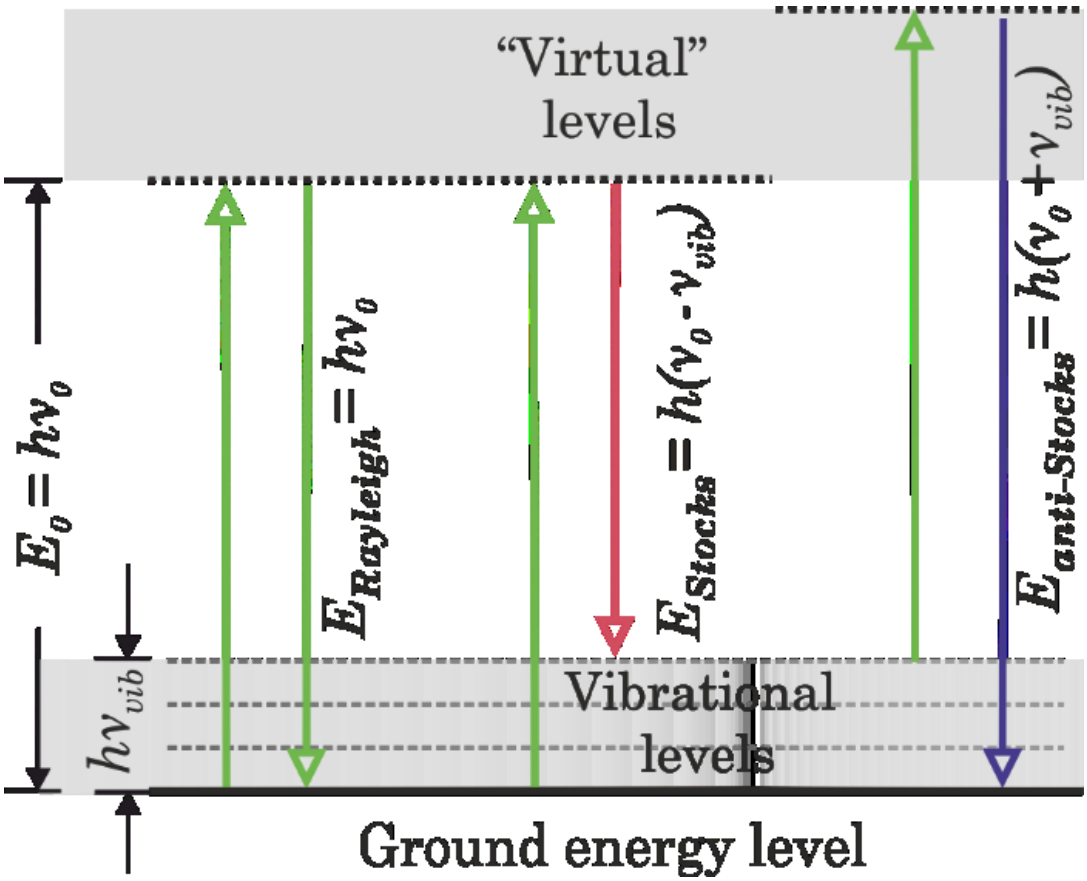

Figure 2.8. The principal scheme of Rayleigh and Raman scattering processes. A molecule is excited from the ground level to the virtual state absorbing a photon and returns to the ground state emitting a lower energy photon. The excitation energy, $E_0 = h\nu_0$, is the energy of the incident photon, h is Planck's constant, and ν_{vib} is the frequency that corresponds to molecular vibrations.

In this work, the Raman studies of the samples were performed using LabRam systems equipped with the He-Ne (632 nm) laser source. The He-Ne laser operates in CW mode with a constant power of 50 mW. Raman spectra were collected in the region of 200 –4000 cm^{-1} with a resolution of 0.5 cm^{-1}.

2.4. X-Ray diffraction

2.4.1. Basic principle

X-ray diffraction is the non-destructive analytical method for the structural characterization of crystalline materials. It is based on the elastic scattering of X-ray photons on the electrons of atoms in the crystals. The wavelength of X-ray photons is usually relevant to the interatomic distances and therefore, an array of periodically arranged atoms scatter the incident monochromatic X-rays producing constructive interference at specific angles (Nespolo, 2011).

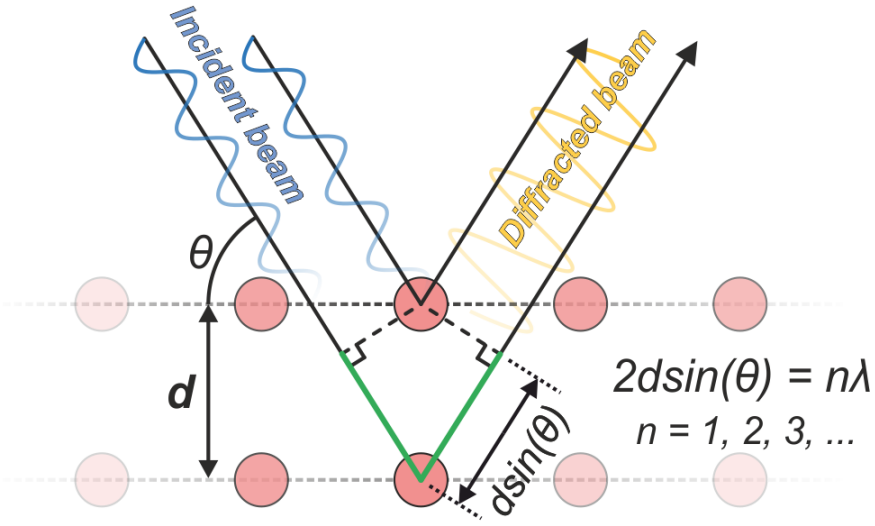

Figure 2.9. The geometric principle of X-ray diffraction. Incident X-rays approach parallel planes of atoms in crystals and diffracted X-ray beam scattered on the lower plane traverses an extra length of 2dsinθ. Constructive interference occurs when the difference in the path lengths is equal to an integer number of the wavelength.

As a consequence of the three-dimensional periodicity of a crystal structure, it is possible to construct sets of atoms arranged in layers with a constant spacing between them. If an incident X-ray beam makes an angle θ with such a set of planes, the “reflected” beam also makes an angle θ with the planes, as in the case of optical reflection (figure 2.9). Reflections from successive planes interfere constructively when the difference between path lengths of the two waves is

equal to an integer number (n) of the wavelength (figure 2.9). The condition of constructive interference is known as Bragg's law (Ladd and Palmer, 2013):

$$2d \cdot sin(\theta) = n\lambda \qquad Eq.(2.4.1.1)$$

where d is the spacing between the lattice planes, θ is the angle of the incident X-ray, n is an integer number, and λ is the wavelength of the incident X-rays. A graph showing the dependence of the intensity of scattered radiation as a function of the scattered angle is called a diffraction pattern, while peaks on the pattern, known as Bragg reflections, are the result of constructive interference corresponding to Bragg's law. The position of the Bragg reflections allows extracting information on the size and shape of a unit cell. Analysis of intensities of the Bragg reflections allows reconstruction of the distribution of electronic densities within the unit cell, which is essential for determining atomic positions, type of atoms and chemical bonds, crystallographic disorder, and other properties (Clegg et al., 2009).

2.4.2. Powder and single crystal XRD

The information that can be extracted from powder or single-crystalline samples is different. A powder sample consists of numerous randomly oriented tiny crystal grains and therefore scatters incident X-ray beam in the form of Debye-Scherrer rings (figure 2.10(a)). In high-pressure crystallography, powder X-ray diffraction (PXRD) is the common technique for phase identification and determination of the unit cell parameters for known phases. However, phase and structural identification of novel compounds, especially with complex crystal structures, has proven to be difficult and ambiguous (Bykov et al., 2020, 2018; Khandarkhaeva et al., 2020; Laniel et al., 2020).

Single crystal samples produce XRD patterns consists of many diffractions spots (figure 2.10(b)) that appears on the XRD detector only at a specific angular orientation of the crystal. Thus, to obtain a dataset with a big number of reflections, diffraction should be collected at the different orientations of the sample. To do so, a sample is commonly placed on a goniometer and rotated with simultaneous collection of diffraction data. The intensities of the collected diffraction peaks from a single-crystal sample provides information on the exact content of the unit cell (i.e. the

type and coordinates of atoms, provide the information on the type of polyhedral, interatomic distance, bound angles, etc.).

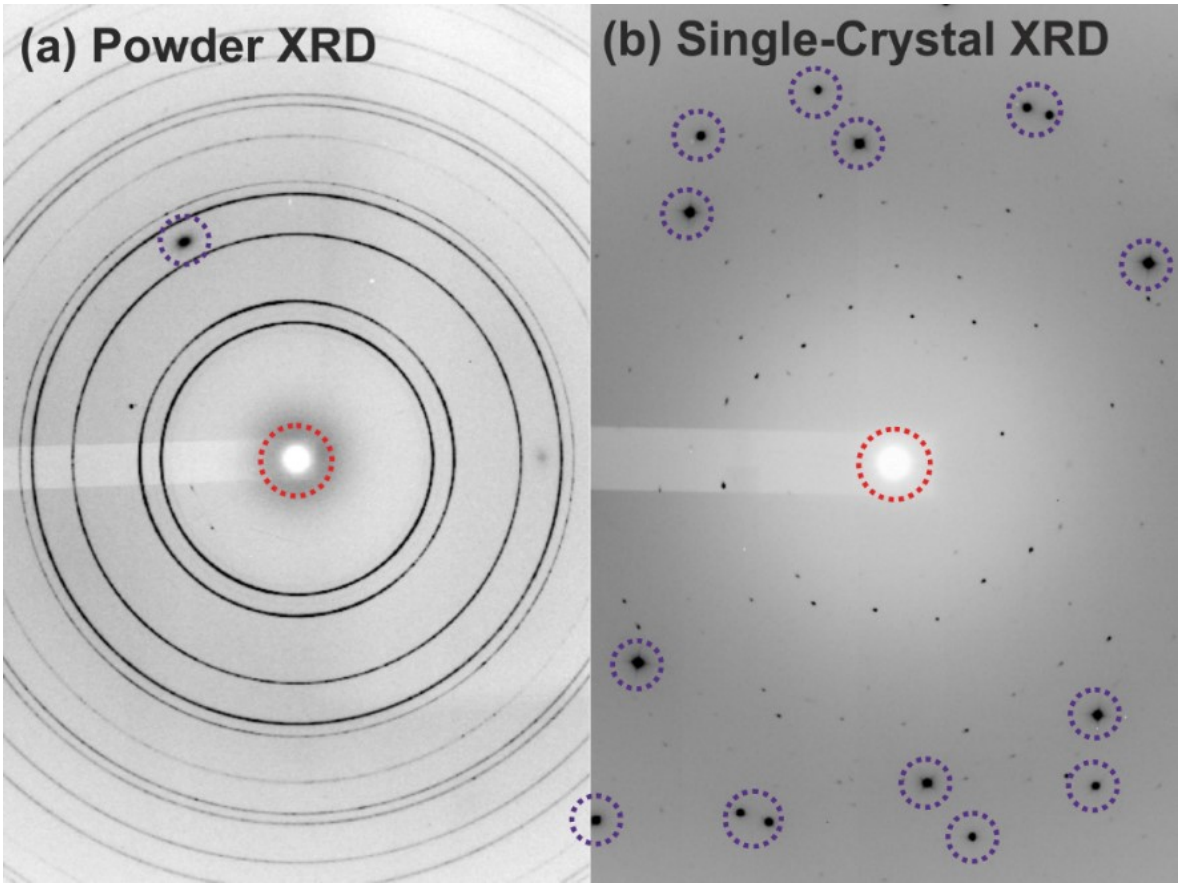

Figure 2.10. Example of X-ray diffraction (XRD) patterns produced by a powder (a) and a single crystal sample (b). The dotted red circles mark the beam stop shadow. Blue dotted circles highlight the intense reflections from the diamond anvil. The Debye-Scherrer rings on (a) correspond to the Pd powder sample. Non-highlighted spots on (b) are the Bragg reflections from the Mn_3O_4 crystal.

The SCXRD and PXRD experiments within the scope of this thesis were performed at following X-ray diffraction beamlines dedicated to extreme conditions: ID15b at ESRF (λ≈0.411 Å, ~10×10 μm^2 beam size, MAR555 flat-panel detector), ID11 at ESRF (λ = 0.30996 Å, 0.5 × 0.5 μm^2 beam size, Frelon4M detector), and P02.2 at PETRA III (λ≈0.29 Å, ~2×2 μm^2 beam size, PerkinElmer XRD 1621 flat-panel detector). The SCXRD data were processed with the CrysAlisPro software (Rigaku Oxford Diffraction, 2018). The analysis procedure includes a peak search, finding reflections

belonging to a unique single-crystal domain, indexing, and data integration. The crystal structures were solved using ShelXT (Sheldrick, 2015) structure solution program and refined with the JANA 2006 software (Petříček et al., 2016). Analysis of powder XRD data was done with the Dioptas (Prescher and Prakapenka, 2015) and TOPAS 4.2 packages.

3.Thesis synopsis

This chapter provides a short overview of the results presented in Chapter 5, that have been published in peer-reviewed journals. Section 5.1 describes the design and development of laser heating setup for *in situ* synchrotron and in-house high and ultra-high pressure studies. The developed laser heating system has been coupled with synchrotron X-ray diffraction and X-ray transmission microscopy (XRTM) at high-pressure diffraction beamline ID15b of European Synchrotron Radiation Facility (Grenoble). Section 5.2 describes a novel method to study the equation of state of crystalline and amorphous solids using optical microscopy and a statistical approach to data analysis. Section 5.3 is devoted to the synthesis of carbon and hydrogen reach palladium alloys in laser-heated diamond anvil cells. Section 5.4 describes the first synthesis and compressibility of nickel carbide, Ni_3C, at pressures of Earth's outer core, and illustrates the application of the developed laser heating setup to experiments at multimegabar pressure range.

3.1. Laser heating setup for diamond anvil cells for in-situ synchrotron and in house high and ultra-high pressure studies

Our goal was to build up the double-sided laser heating set up for ultra-high pressure experiments in DACs. As soon as the concept of transportable setups was proven to be very productive (Aprilis et al., 2017; Kupenko et al., 2012), we decided to develop a system that can be used in different experimental environments in-house and at synchrotron facilities. Such a system had to allow focusing laser spot on the sample for precise heating in DACs at pressures above 200 GPa and at the same time provide accurate *in situ* temperature measurements.

The designed setup consists of two identical parts which are schematically shown in figure 3.1.1.

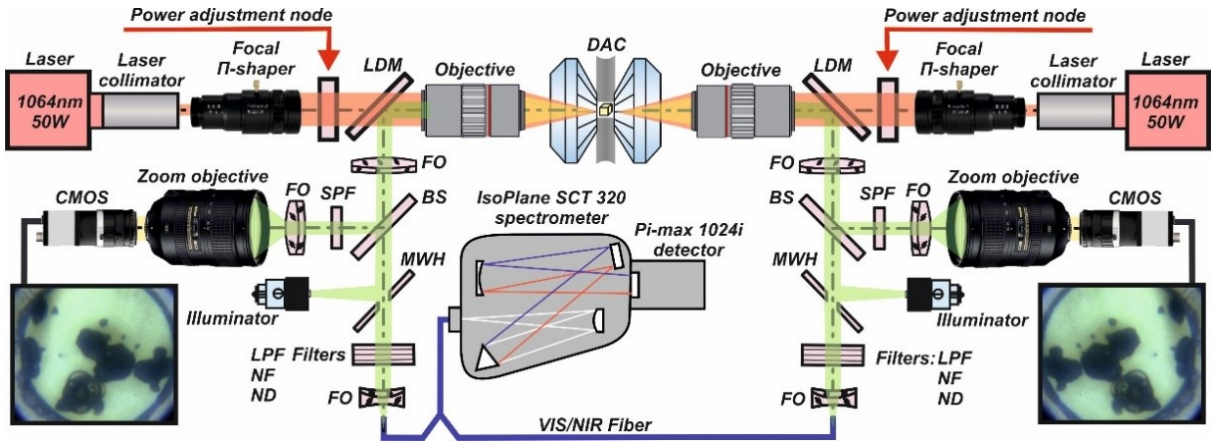

Figure 3.1.1. Schematic diagram of the double-sided laser heating system for diamond anvil cells. LDMs are the long-pass dichromic mirrors; FOs are the focusing optics; BSs are 50/50 beam splitters; SPFs are the short-pass filters with a cut off at 800 nm; CMOSes are the cameras for optical observation; MWHs are the mirrors with a hole; LPFs are the long-pass filters with a cut-on wavelength of 550 nm; NFs are the notch filters at 1064 nm; NDs are neutral density filters.

Each of the parts includes the following nodes:

- NIR Laser
- Focusing and shaping optics
- Power control module
- Observation module
- Temperature collection module

All optical components are mounted on the breadboard and can be easily adjusted or modified depending on a type or specific needs of experiments. System flexibility allows the quick exchange of the laser sources for in-house or synchrotron experiments (i.e. laser sources do not need to be transferred together with the laser-heating setup). In our studies, we use two pairs of lasers: the first pair consist of SPI RedPower R4 Modulated Fiber Lasers with a maximum power of 100 W, the second one of SPI G4 Pulsed Fiber Lasers with a maximum output power of 50 W. Both laser pairs produce collimated randomly polarized Gaussian beam (TEM00) with central wavelength 1064 ± 10 nm. The SPI RedPower R4 lasers can be operated in a continuous-wave (CW) mode or modulated with a maximum frequency of up to 100 kHz. The G4 Pulsed Fiber Lasers

can be operated in both continuous-wave and pulsed mode with minimal possible laser pulse FWHM of 11 ns. To expand the output collimated laser beam with spatial Gaussian distributed intensity to a flattop π-shape profile, the LH setup is equipped with Focal-π Shapers (Focal-π Shaper_9_1064 by AdlOptica GmbH), specially designed for TEM00.

In synchrotron experiments, we use a GeoHeat 40_NIR achromatic objective. The GeoHeat 40_NIR is used for simultaneous temperature measurements and focusing the NIR laser beam (Aprilis et al., 2017) and minimizes chromatic aberrations in the spectral range of 600-900 nm. By adjusting the Focal-π Shaper we reach the smallest FWHM of the laser beam of 20 µm when the flat-top beam profile is used.

For in-house experiments with ultra-high pressure DACs, we apply a Mitutoyo 20x objective (Mitutoyo NIR infinity-corrected M Plan Apo B 20x). It allows the focusing of the laser beam to ~ 5 µm FWHM and provides higher magnification and better optical resolution which is crucial as the size of a sample could be less than 5 µm.

The power of the laser beam for sample heating is controlled by polarizers (figure 3.1.2).

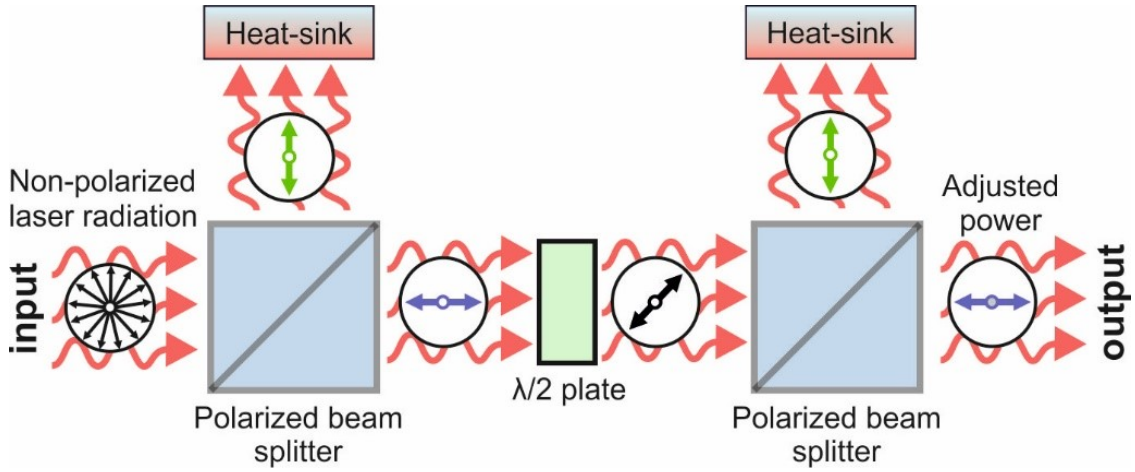

Figure 3.1.2. Schematic diagram of the power control node. The module consists of two polarized NIR beam splitters (Thorlabs CCM1-PBS25-1064) and a half-wave plate (Thorlabs WPH05M-1064) mounted between them. The output power level is controlled by the rotation of the λ/2 wave plate in the range from 0 to 45 degrees to reach zero and maximum power, correspondingly.

Optical power control allows adjustment at laser power below 5 W (that is a common problem for fiber lasers) and allows for the independent adjustment of the laser pulse shapes and their energy while operating in pulse mode.

The image of the sample inside the DAC is obtained either in transmitted light, if the material in the sample chamber is at least partially transparent, or/and in reflected light. The light passes through a set of lenses into a zoom objective (Nikon AF-S NIKKOR 28-300mm f/3.5-5.6G ED VR Lens) projecting the image of the sample on the matrix of a CMOS camera (EYE © UI-3240CP). Coupled with GeoHeat_40_NIR lenses, the system enables the magnification to be varied within approximately 20 to 35 times, while Mitutoyo 20x provides 80 to 320 times magnification.

Temperature measurements are performed utilizing spectroradiometry. A 50/50 beam splitter (Thorlabs BSW10) installed on the observation path reflects half of the light intensity to the spectrometer for the temperature measurements, while the other half goes to the CMOS camera for simultaneous visual observations. The thermal radiation reflected by the beam splitter is focused on the optical fiber and guided into an IsoPlane SCT 320 spectrometer with a 1024x256 PI-MAX 4 camera (Princeton Instruments, Inc.). Once the thermal emission spectra of the heated sample are collected, the temperature can be extracted by fitting spectra in a given wavelength range (typically 570-830 nm) to the grey body approximation of Plank's law.

Figure 3.1.3 shows the in-house configuration of the LH setup mounted on the optical table.

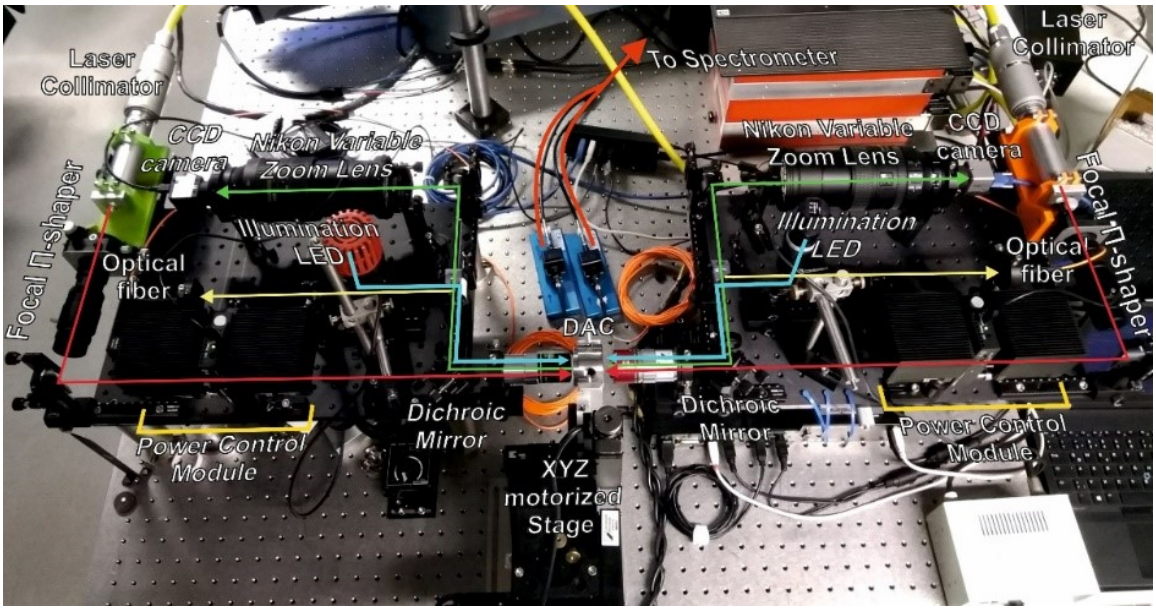

Figure 3.1.3. Configuration of the LH setup for in house experiments

The setup was successfully tested in experiments with 40-µm culet size anvils (pressure chambers are about 10 to 20 µm in diameter, with characteristic sample sizes of about 5 µm) at pressures over 200 GPa.

The transportability of the system has been demonstrated during a series of experiments at the synchrotron X-ray source coupled with LHDAC at the High-Pressure Diffraction beamline (ID15B) of the European Synchrotron Radiation Facility (ESRF). The system was transported to the ESRF and mounted in the experimental hutch of the beamline (figure 3.1.5) within a single day (8 to 10 hours) prior to the experiment.

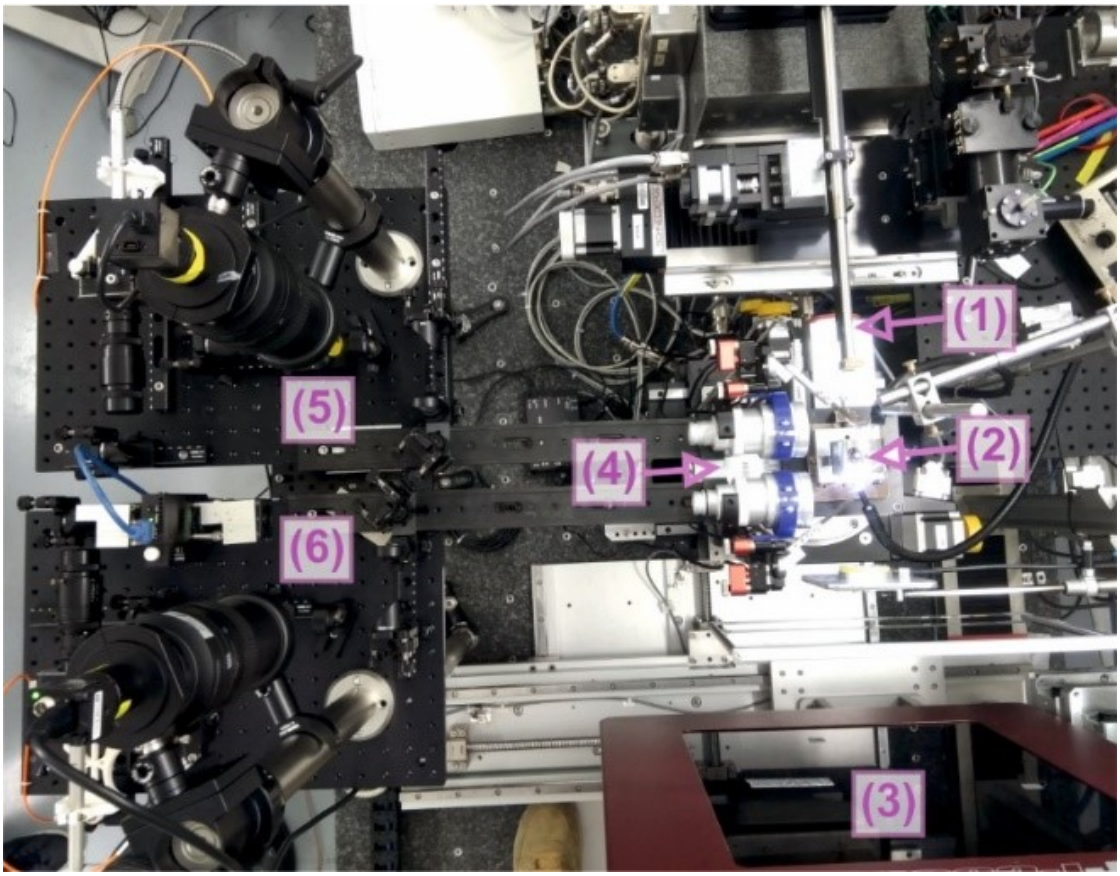

Figure 3.1.5. Configuration of the LH setup mounted on ID15b beamline of ESRF. (1) X-ray beam pinhole; (2) DAC; (3) Mar555 detector; (4) Focusing and targeting optics; (5) upstream breadboard; (6) downstream breadboard.

The flexible design of our setup allows the simple interchange of laser sources and focusing optics for application in different types of studies. We demonstrate the application of the setup for the

in-situ powder X-ray diffraction study on synthesis and stability of PdH (see Section 5.1). Moreover, we were able to couple our laser-heating setup with X-ray transmission microscopy (XRTM) at ID15b at ESRF. That allows visualizing the processes inside the DAC sample chamber at high temperatures. To the best of our knowledge, there were no experiments with XRTM LHDAC before. Particularly, we have observed the melting of platinum in a DAC at high pressures and demonstrated the applicability of this approach for in situ melting detection in DAC experiments (figure. 3.1.6).

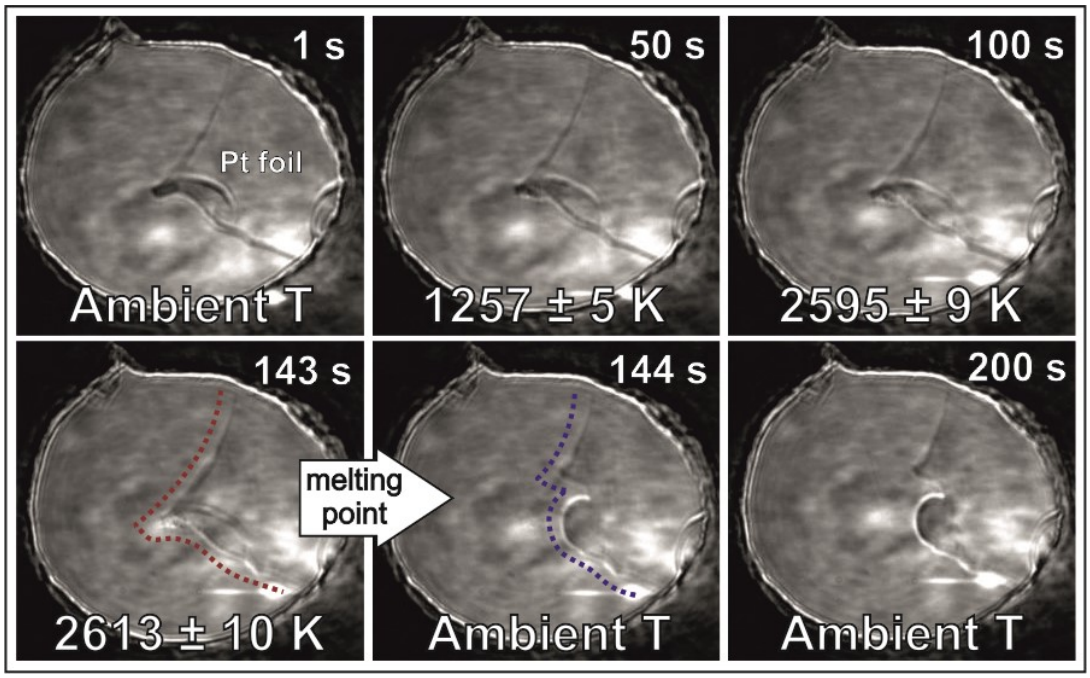

Figure 3.1.6. Example of the melting detection on platinum using XRTM in LHDAC. XRTM images of platinum foil were taken during the heating process with 1 second exposure time each. Red and blue dotted lines represent the shape of the Pt foil before and after melting respectively. The melting event was detected between 143th and 144th seconds by observation of the significant changes in the shape of the Pt foil. The melting temperature of Pt at 22 (1) GPa is 2613±10 K.

3.2. Isothermal equation of state of crystalline and glassy materials from optical measurements in diamond anvil cells

Here we developed a methodology to study the EOS of crystalline and amorphous materials in DAC. Our methodology exploits high-resolution optical microscopy in DACs, image analysis, and statistical data treatment. A significant advantage of our approach is that experiments do not require access to synchrotron facilities or specialized X-ray sources. At the same time, our method can be easily applied in combination with X-ray imaging and diffraction. The data analysis is fully automatized (i.e. the effect of the operator is negligible) and applicable to opaque crystalline and amorphous/glassy materials.

The optical system is based on the laser heating setup describe in detail in the Section 5.A. The schematic diagram with the key components is presented in figure 3.2.1.

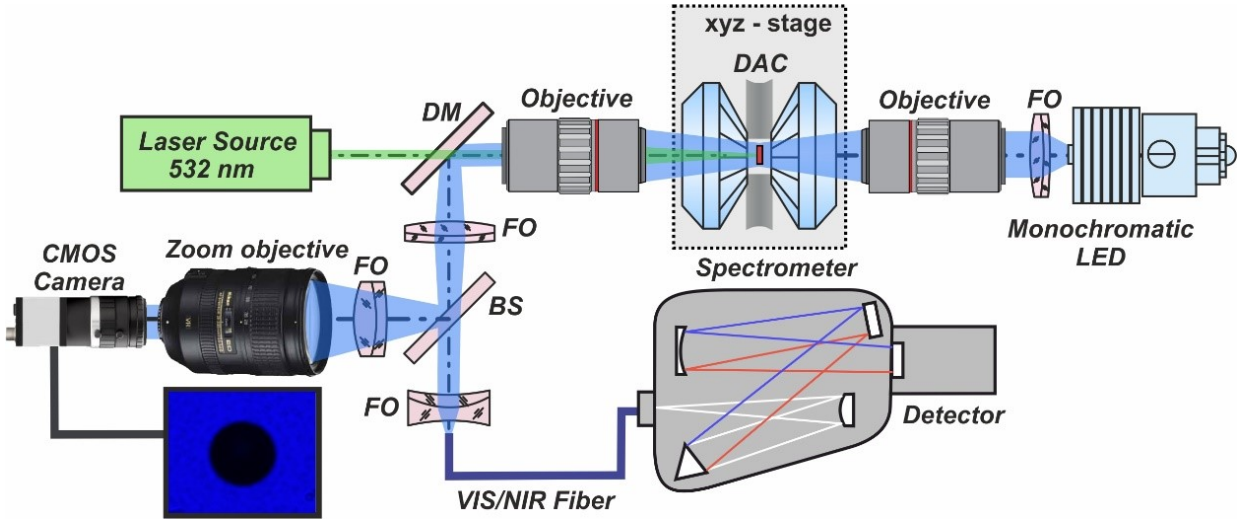

Figure 3.2.1. Schematic diagram of the optical system. DM is the long-pass dichromic mirror; FO is the focusing optics; BS is the 50/50 beam splitter; CMOS is the camera for image observation.

The image of the sample is formed by transmitted monochromatic light passing through a DAC sample chamber and collected from the opposite side by a long working distance objective. Further, the light passes through a set of lenses and projects the sample image on the matrix of a high-resolution CMOS camera.

The geometrical shape of a sample plays an important role in data acquisition and analysis. Simple and symmetrical shapes, such as balls or rectangular plates, allow multiple measurements of the sample length from a single image and therefore improves the statistics and reduces the random error. As samples, we use spheres of glassy carbon and rectangular plates made of Ti (figure 3.2.2). Spherical samples were directly purchased from Cospheric Microspheres Inc. while square plates were shaped by milling Ti foil using FEI - QUANTA 3D Focused Ion Beam (FIB).

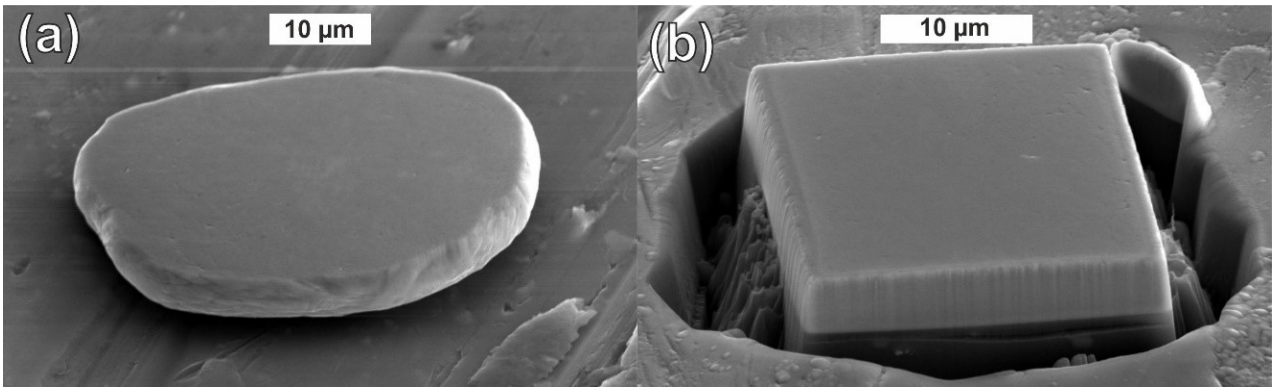

Figure 3.2.2. SEM images of the Ti sample. (a) A flattened microsphere of the initial diameter of about 25 µm; (b) A square plate-shaped by FIB.

Before data collection adjustment of the optical system is necessary for reproducible and precise measurements. Such parameters as the intensity and angle of the incident light, CMOS camera parameters, and the sample position within the field of view must be kept constant during the whole set of measurements at different pressure points. To achieve stable illumination conditions during the whole experiment, the DAC was coupled with a membrane pressure controller and mounted on a 3-axis motorized stage.

For correct determination of the sample dimensions using optical microscopy, it is necessary to perform length measurements with the sample in the right focus position (figure 3.2.3) at each pressure point. In our method, we implement the focus stacking approach, by collecting the sample images upon continuous movement of the DAC along the optical axis.

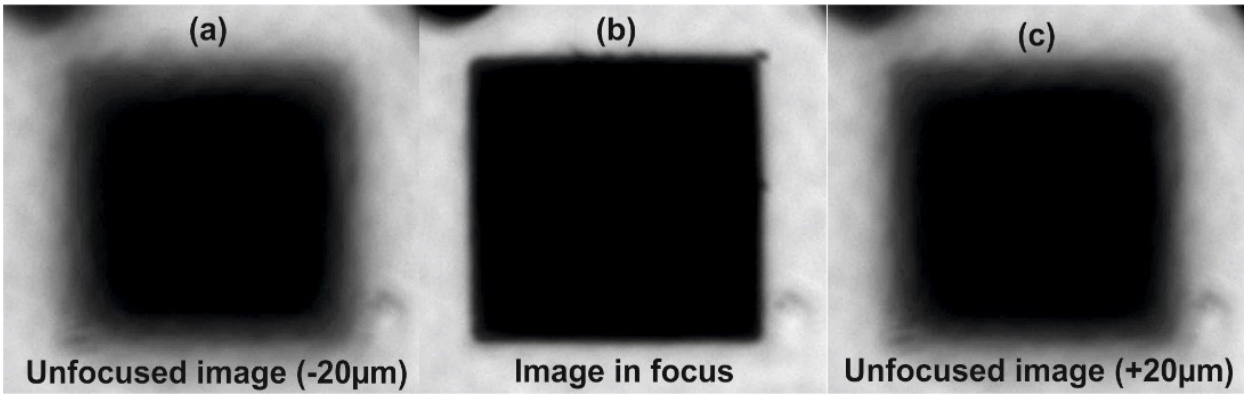

Figure 3.2.3. Illustration of focus stacking on the example of images of a titanium plate at 4 GPa. (a) The image was taken at -20 μm from the approximate in-focus position; (b) near the in-focus position as first determined by eye; (c) at + 20 μm from the approximate in-focus position.

Further, all images are analyzed and only ones which are in focus positions are used for length determination (the algorithm for selecting in-focus images is described below). A typical number of images in a single dataset is up to 200.

We have developed a fully automatic procedure for data analysis including selecting the in-focus images, length determination, and error analysis. The procedure includes the analysis of image intensity profiles at the edges of the sample. It allows to precisely determine the steepness and position of the edge, and to determine the length through those parameters (figure 3.2.4).

We describe the edges of the intensity profile using the parametric sigmoid function:

$$S(x) = A_o + \frac{K - A_0}{1 + e^{-\alpha(x - x_0)}} \qquad Eq.(3.2.1)$$

(where x is the pixel coordinate, A_o is the lower asymptote, K is the upper asymptote, α is the growth rate (or steepness of the curve) and x_0 is the value of the sigmoid's midpoint). Thereby, we define the sample length in pixels as a difference between the two sigmoid's midpoints taken along a single image cross-section (at the right and left edges of the sample) ($x_0^{right} - x_0^{left}$). Such parametrization allows defining the positions of the edges with subpixel accuracy.

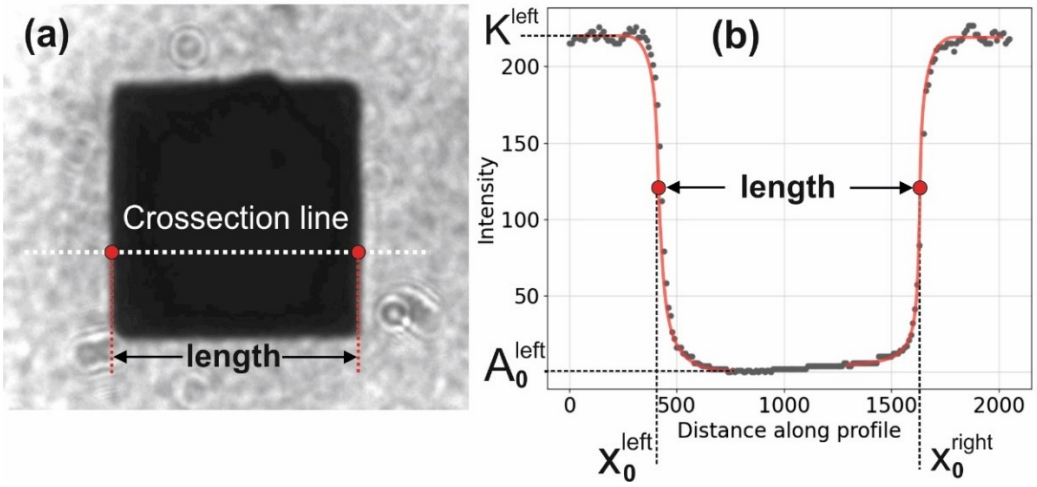

Figure 3.2.4. Image intensity profile for defining the edges of the sample. (a) Sample image with the cross-section line. The enlarged red dots mark the position of the sample edges, which define the sample length (in a horizontal direction); (b) image cross-section intensity profile. Grey dots are the measured intensity profile; red curves are the fit of the left and right edges regions to the parametric sigmoid functions; enlarged red dots are left and right sigmoid's midpoints, which define the position of the sample edges.

If an object is not in focus, its edges look blur. It is obvious that the sharper the image, the steeper the edges of the intensity profile (figure 3.2.5). To select the images, which are in-focus, we analyzed every image of the set and plotted the steepness parameter (i.e. the growth rate parameter α of the sigmoidal function, Eq. 3.2.1) vs the image number, which indicates the DAC position along the optical axis. An example of such a plot is shown in figure 3.2.6. Only the images with the highest absolute growth rate are selected as in-focus and further considered for length measurements.

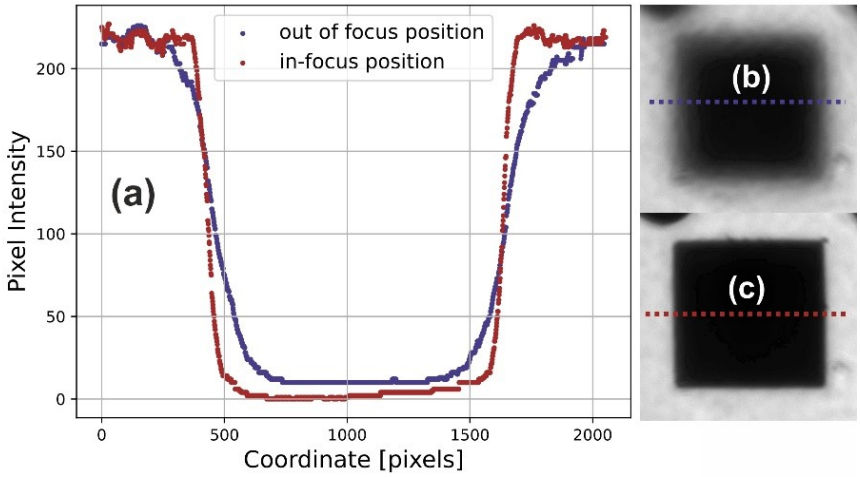

Figure 3.2.5. The image cross-section intensity profiles and microphotographs of the sample. (a) Profiles; (b) out of focus position; (c) in-focus position.

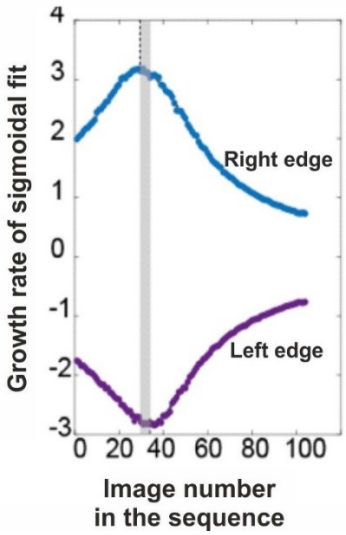

Figure 3.2.6. Growth rate (parameter α of the sigmoidal function) vs the image number.

Since both vertical and horizontal cross-sections are used for in-focus image selection, the algorithm gives four, usually slightly different, focal positions. This can be attributed to slightly uneven illumination of different sample edges or minor inclination of the sample in the DAC. However, we found that for a set of 100 - 150 images (frames) the variations within up to 10 frames do not introduce measurable errors in the length of the sample (see error evaluations section below).

Usually, four in-focus images are selected (one per top, bottom, left, and right edges of the sample).

For each image, we made a cross-section mesh of 50 to 100 lines with a line spacing of 5 to 20 pixels (figure 3.2.7).

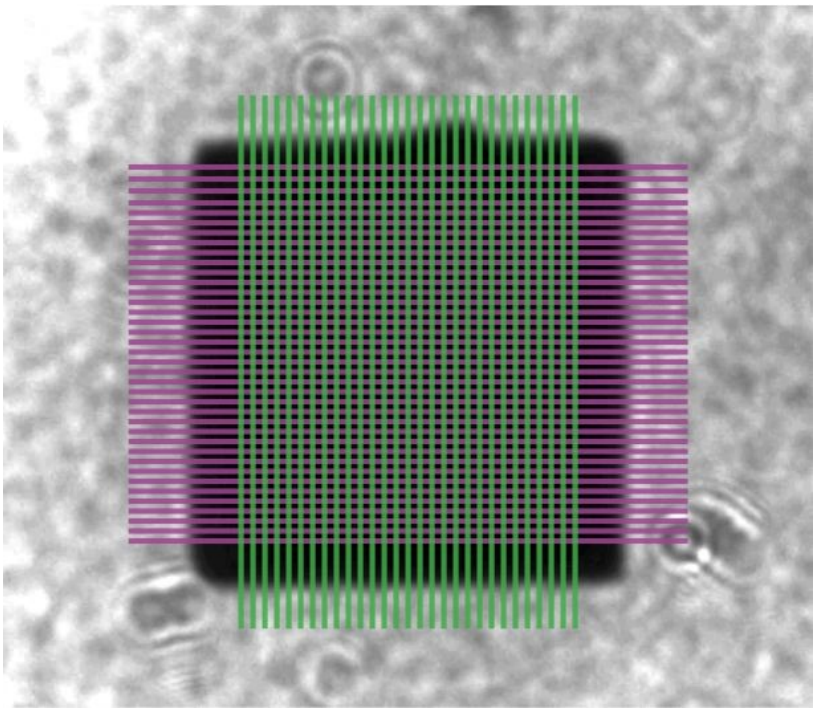

Figure 3.2.7. Schematic of the cross-section mesh for the length measurements. Green and purple lines represent image cross-sections. Length measurements are performed along each of vertical and horizontal cross-sections. The mesh size depends on the sample size and geometry, with a typical value of 50 to 100 cross-section lines per dimension with line spacing of 5 to 20 pixels.

For each cross-section line, the length of the sample was determined independently. All measurements for vertical and horizontal lines were averaged independently, and the standard deviation was calculated for both vertical and horizontal dimensions.

Assuming that sample conditions in DAC are (1) quasi-hydrostatic; (2) the sample does not have voids in the bulk; (3) compression of the sample is isotropic, the sample strain (f_e) can be described as Eulerian finite strain (Katsura and Tange, 2019):

$$f_e = \frac{1}{2}\left[\left(\frac{V_p}{V}\right)^{\frac{2}{3}} - 1\right] \qquad Eq.(3.2.2)$$

where V is the sample volume at a given pressure, and V_p is the sample volume at the reference pressure. Hence the following relationship is true:

$$\frac{V}{V_p} = \left(\frac{L}{L_p}\right)^3 \qquad Eq.(3.2.3)$$

where L is the average length at a given pressure, and L_p is the average length at the reference pressure. To determine the bulk modulus ($\boldsymbol{K_0}$) and it's derivative ($\boldsymbol{K_0'}$) the pressure–strain data, obtained by optical measurements, were fitted to the 3rd order Birch-Murnaghan EOS (Eq. 2.1.3.3) (Anderson, 1995).

The described method was validated by comparing of the results of optical measurements with the well-known EOS of the same material obtained by XRD. We chose Ti as the reference material, it undergoes the α-to-ω structural phase transition between 2 and 12 GPa at 300 K depending on the pressurization conditions (Errandonea et al., 2005) which result in the volume reduction of a few percent and provides a chance to test if the first order phase transition can be detected using the presented methodology.

The sample of Ti rectangle plate was loaded into the DAC with Ne as a PTM and then studied on compression in the pressure range of 8 to 30 GPa (figure 3.2.8).

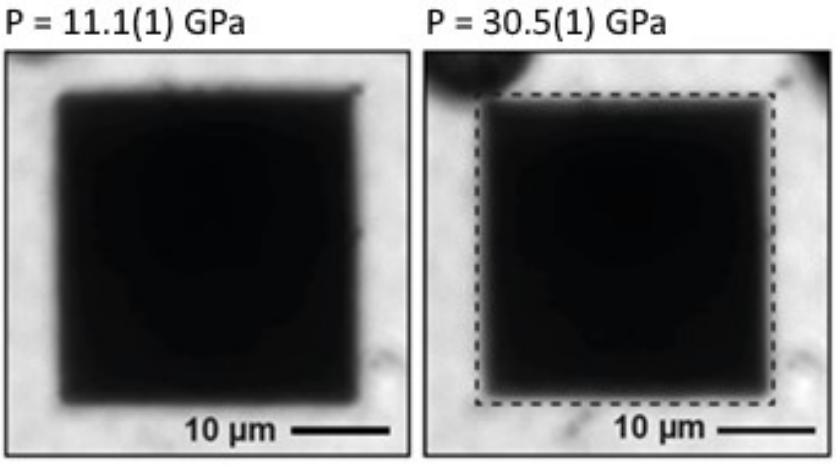

Figure 3.2.8. Images of the Ti square plate at 11.1(1) and 30.5(1) GPa. The dashed line on the right image corresponds to the sample contour at 11.1(1) GPa.

The results of measurements, in form of the dependence of the relative volume on pressure, are shown in figure 3.2.9. Some irregularities in the compressional behavior of the sample were observed at around 11 GPa, which may be related to the α-to-ω Ti phase transition (Dewaele et al., 2015). However, the effect is hardly visible (figure 3.2.9, inset).

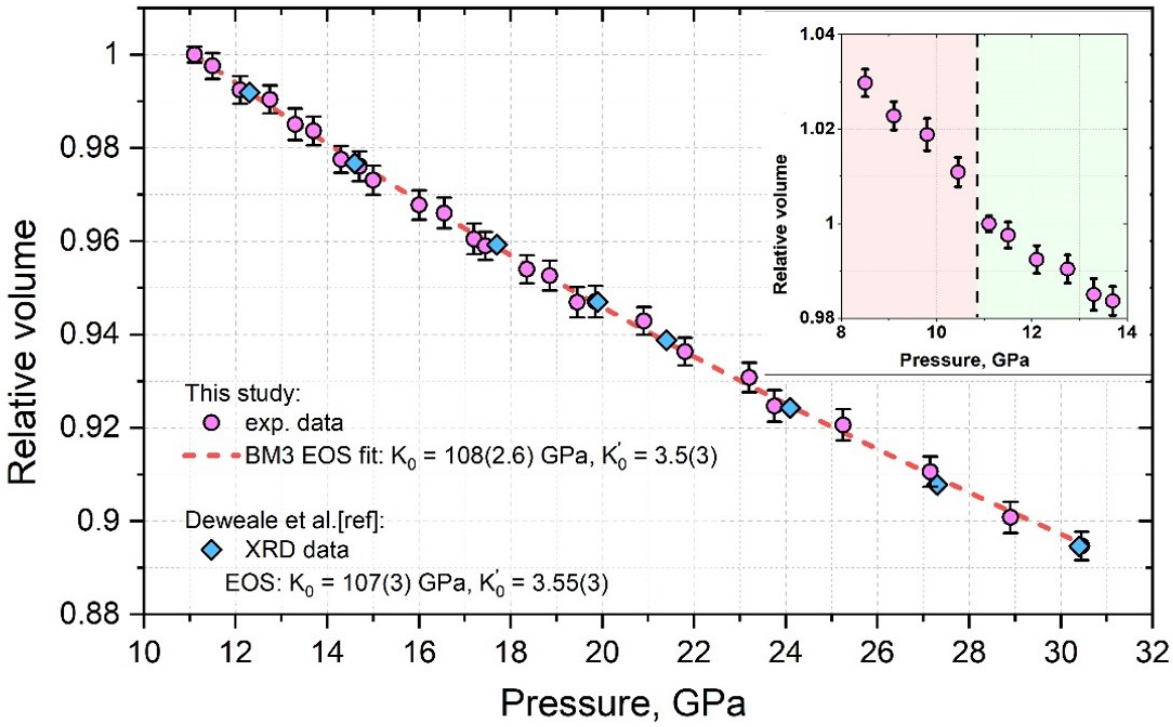

Figure 3.2.9. The pressure dependence of the relative volume of ω-Ti. Our experimental points are shown by purple circles; the red dashed line is the fit of the experimental data to the 3rd order BM EOS with the following parameters $K_0 = 108\ (2.6)$ GPa GPa, $K' = 3.5(3)$. Blue diamonds are the experimental data from Dewaele et al (2015) obtained by XRD measurements. The inset shows the P region between 8 and 14 GPa. Different colors indicate the fields of α-Ti (pink) and ω-Ti (green).

The data collected above 11 GPa corresponds to ω–Ti. Over the compression from 11.1(1) to 30.5(1) GPa, a decrease in the average sample length of 48 pixels (~1μm) was observed, while the sample volume contracted by about 10%. The pressure – relative volume data (figure 4.2.10) were fitted to the 3rd order BM EOS with the parameters $K_0 = 108\ (2.6)$ GPa and $K' =$

$3.5(3)$, in good agreement with those obtained from XRD data of Dewaele et al. (2015) with $K_0 = 107(3)$ GPa, $K' = 3.55(3)$).

Additionally, we applied the developed methodology to study the EOS of glassy carbon. A glassy carbon sphere (microspheres type-I, purchased from Alpha Aesar Inc.) with a diameter of about 25 µm was loaded into the sample chamber and pressurized in a Ne pressure transmitting medium from 6.9(1) up to 30 GPa. Over the compression, we observed a decrease in the average sample length (the diameter of the sphere) of ~81 pixels (~1.7 µm), and the sample volume contracted by about 20%. The pressure-volume relation for glassy carbon is shown in figure 3.2.10. As expected, the compressibility of glassy carbon appeared to be relatively high, with the bulk modulus found to be $K_0 = 28.6(8)$ GPa ($K' = 5.5\ (2)$). Thus, the compressional behavior of glassy carbon was found to be very smooth, in agreement with the previous studies based on Raman spectroscopy (Solopova et al., 2013), which gave no evidence of a significant change in the type of chemical bonding in GC up to 60 GPa.

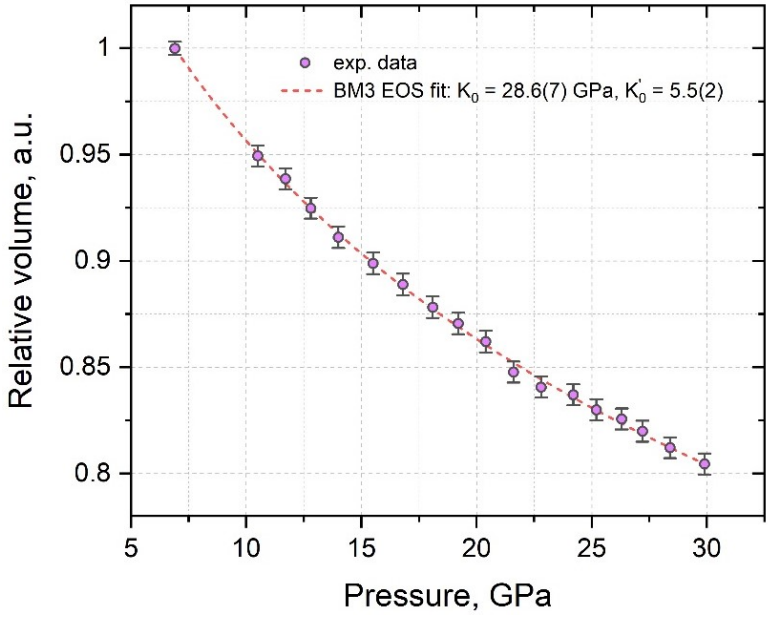

Figure. 3.2.10. The EOS of glassy carbon. Our experimental points are shown by purple circles; the red dashed line is the fit of the experimental data to the 3rd order BM EOS with the following parameters: $K_0 = 28.6(8)$ GPa, $K' = 5.5\ (2)$.

The EOS of glassy carbon reported in this work was determined for the first time. The significant advantage of the presented method is that experiments do not require access to synchrotron facilities or specialized X-ray sources (but it can be easily coupled with X-ray imaging and diffraction).

3.3. Synthesis of palladium carbides and palladium hydride in laser-heated diamond anvil cells

In order to detect the effect of possible carbon or hydrogen dissolution in palladium, we require data on the compressibility of pure Pd. Pd remains fcc structure (fm-3m space group) over a wide range of pressures. Known carbides and hydrides of palladium are rather alloys than ionic compounds (Manchester et al., 1994b): carbon or hydrogen atoms occupy octahedral interstitial sites of the fcc palladium structure that results in an increase of the lattice parameter without change of the symmetry (i.e., there are no extra Bragg reflections compare to pure Pd). Thus, to determine the composition we have to rely on the measured lattice parameters and therefore good EOS of pure Pd is needed.

To determine EOS of pure Pd a piece of Pd foil was loaded into a sample chamber of a DAC along with Ne and stepwise pressurized up to 30 GPa. The experimental pressure-volume data were fitted (figure 3.3.1) using the third order Birch-Murnaghan EOS (BM3 EOS, Eq. 2.1.3.3) with the following parameters: V_0= 58.868(2) Å^3, K_0 = 157(3) GPa, and K' = 9.9(4). The volume of the Pd unit cell at ambient pressure is in good agreement with literature data: 58.85 Å^3 (McMurdie et al., 1986), 58.9 Å^3 (Rao and Rao, 1964).

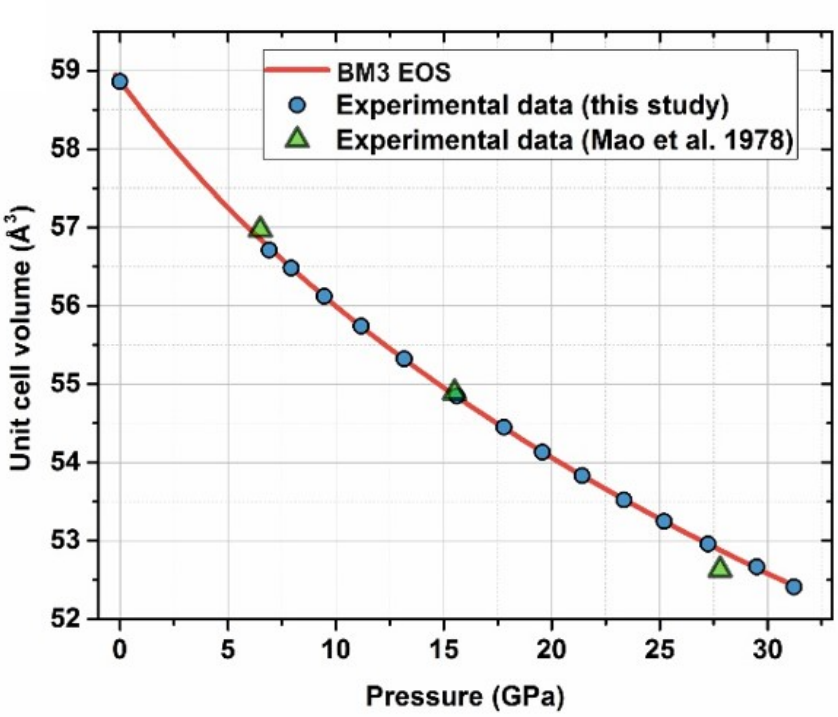

Figure 3.3.1. The pressure dependence of the unit cell volume of Pd. Our experimental points are shown by circles. The solid curve is the fit of the experimental P-V data using the BM3 EOS with the following parameters: V_0= 58.868(2) Å^3, K_0 = 157(3) GPa, and K_0' = 9.9(4). Errors in experimental data are within the symbol size

In the second experiment, the sample of Pd foil was pressurized in Ne pressure-transmitting medium to 52(1) GPa and laser heated up to 3000(200) K.

The new phases that appeared after laser heating were indexed as fcc structured PdC_x. The carbon content – x was estimated using Vegard's law, and the known unit cell volumes of pure Pd and $PdC_{0.03}$(Cadeville and Lerner, 1976). The phase with the largest amount of carbon was determined as $PdC_{0.21(1)}$, the smallest content of carbon was found to be $PdC_{0.15(1)}$. A possible explanation of that phenomenon is the temperature dependence of carbon solubility in palladium that leads to the formation of a plethora of PdC_x compositions at the presence of large temperature gradients during laser heating. We followed changes in the lattice parameters of various PdC_x phases with pressure (Figure 3.3.2) and determined the parameters of the BM3 EOS for $PdC_{0.21(1)}$: V_0 = 65.1(1) Å^3, K_0 = 241(9) GPa and K_0' = 2.1(3).

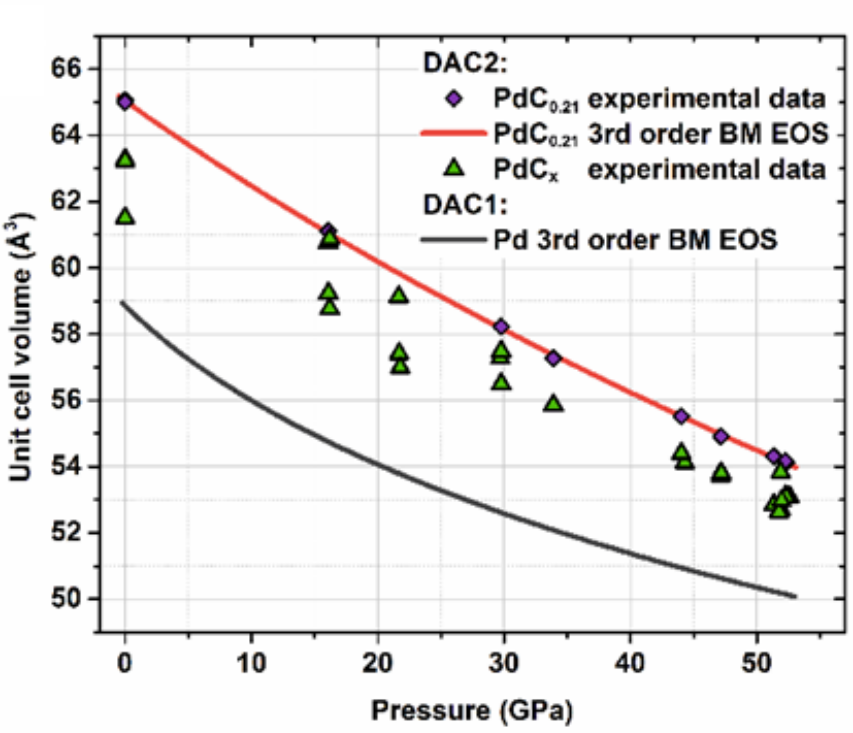

Figure 3.3.2. The pressure-volume dependence for a few PdC_x. phases with different carbon content from x=0.15(1) to x=0.21(1). Green triangles and purple diamonds represent experimental results; the solid red curve is the BM3 EOS fit for $PdC_{0.21(1)}$ (V_0 = 65.1(1) Å^3, K_0 = 241(9) GPa and K_0' = 2.1(3)). All error bars are within the size of the symbols.

In the third experiment, a piece of Pd foil was clamped between two thin layers of NaCl and compressed up to 58(2) GPa. NaCl was used as a pressure transmitting medium to provide better thermal insulation compared to Ne (Uts et al., 2013), and reduce thermal gradients over the laser heating. Laser heating of the sample up to 2500(200) K results in the synthesis of $PdC_{0.19(1)}$. No peak splitting of PdC_x was detected here. This supports our suggestion of the temperature dependence of carbon's solubility in palladium. The P-V data obtained on $PdC_{0.19(1)}$ decompression were fitted to the BM3 EOS model and gave the following parameters V_0 = 64.51(5) Å^3, K_0 = 189(8) GPa, and K_0' = 4.5(4).

It is known that laser heating of metal in paraffin oil in a DAC may lead to the synthesis of carbides (sometimes together with hydrides) (Narygina et al., 2011). In the fourth experiment, a piece of Pd foil was loaded inside the sample chamber of a DAC along with paraffin oil, which served as

both a pressure-transmitting medium and a source of carbon and hydrogen. The sample was compressed up to 39(2) GPa (close to the pressure at which PdC_x were synthesized) and laser-heated at around 1500(200) K. The X-ray diffraction data of the temperature quenched sample reveals the presence of polycrystalline diamond and the unknown fcc-structured phase with the unit cell volume V = 60.18(5) $Å^3$ at 39(2) GPa. Within the uncertainty the unit cell volume of the new fcc-phase, 60.18(5) perfectly matches with the unit cell volume, 60.1(1) $Å^3$,of fcc PdH at the same pressure (Brownsberger et al., 2017). Thus we assume that the reaction of pure Pd and paraffin oil at ~39 GPa and ~1500(200) K results in the synthesis of PdH compound and diamond. In conclusion, we show that pure Pd metal reacts with carbon from the diamond anvil at high pressure and high-temperature conditions with the formation of *fcc* PdC_x. We suggest that carbon solubility in palladium strongly dependent on temperature. Additionally, we have shown the possibility of the synthesis of PdH at high pressure in DACs by a direct chemical reaction of Pd and paraffin oil and found that when there is an excess of both carbon and hydrogen, PdH is the favorable reaction product.

3.4. Synthesis and compressibility of novel nickel carbide at pressures of Earth's outer core

The sample of Ni foil was pressurized in LiF pressure-transmitting medium up to 184 (5) GPa and laser-heated up to 3500 (200) K. A direct reaction between Ni and carbon from the diamond anvil resulted in the synthesis of a new compound indexed as orthorhombic. The reaction product was identified using synchrotron single-crystal XRD. The structure solution and refinement revealed the presence of cementite-type orthorhombic structure (space group Pnma, #62; a = 4.520(3) Å, b = 5.8014(17) Å, c = 4.009(4) Å at 184 (5) GPa) with Ni_3C composition (figure 3.4.1).

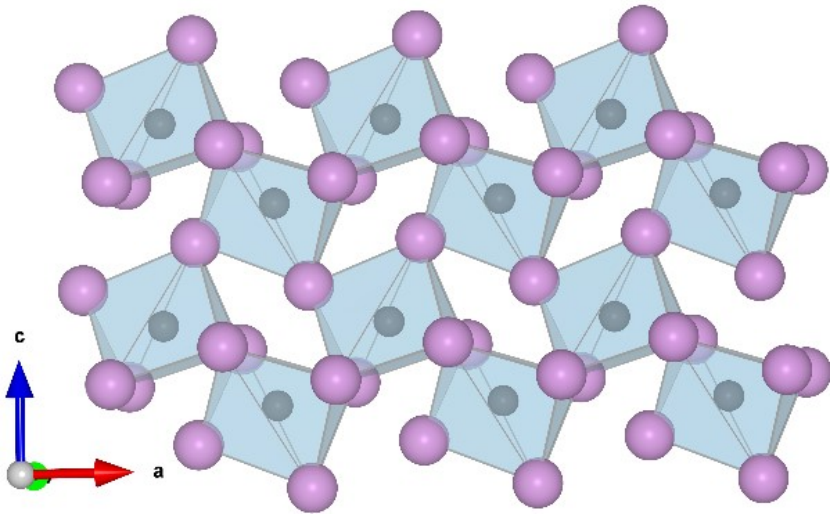

Figure 3.4.1. Crystal structure of the cementite type Ni_3C at 184(5) GPa and room temperature. Purple and black spheres designate nickel and carbon atoms, correspondingly.

The Ni_3C sample was studied on a stepwise decompression and no diffraction pattern from Ni_3C was observed at pressures below 84(2) GPa. The pressure-volume relation of Ni_3C was fitted to the 3rd order Birch-Murnaghan (BM3) EOS and gave the following parameters: V_0 = 147.7(8) Å^3; K_0 = 157(10) GPa, K´ = 7.8(6) (figure 3.4.2).

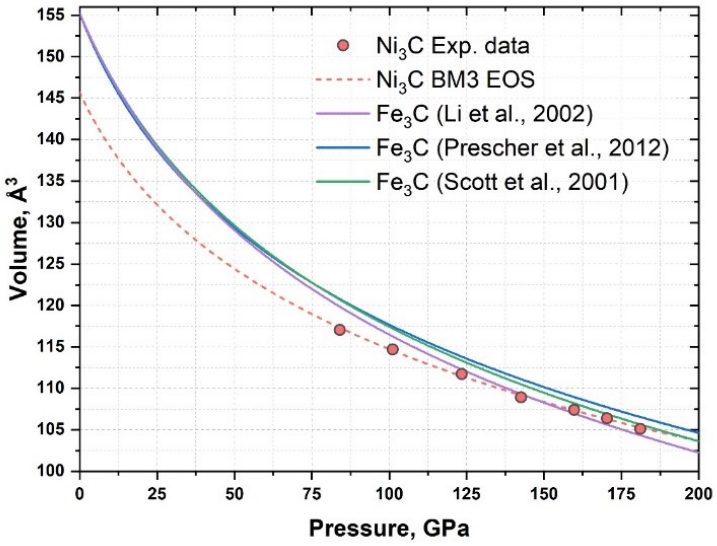

Figure 3.4.2. The pressure-volume dependence of Ni_3C. Red dots represent experimental data, the dashed red curve is the BM3 EOS fit (V_0 = 147.7(8) Å^3; K_0 = 157(10) GPa, K´ = 7.8(6)).

Based on obtained data, we calculated the bulk sound velocity for Ni_3C as a function of pressure at ambient temperature and compared it with those known for Fe, Ni, and possible carbon-bearing components of Earth's core (Fe_3C and Fe_7C_3). We found that Ni_3C exhibits similar bulk sound velocities as Fe_3C and Fe_7C_3 at pressures up to 400 GPa (figure 3.4.3). Thereby, the presence of Ni in the alloy likely should not affect the elastic properties of the Fe-Ni-C system but potentially can change the carbon distribution. There is no experimental information regarding the behavior of the Fe-Ni-C system at conditions of Earth core, but the stability of Ni_3C at pressures above 150 GPa may indicate that the addition of Ni stabilizes cementite-type phase over orthorhombic Fe_7C_3 (Liu et al., 2016; Prescher et al., 2015). Alternatively, our result may infer an immiscibility gap between Ni_3C and Fe_7C_3. Further experimental work is needed to clarify the phase relations in the Fe-Ni-C system at multimegabar pressures.

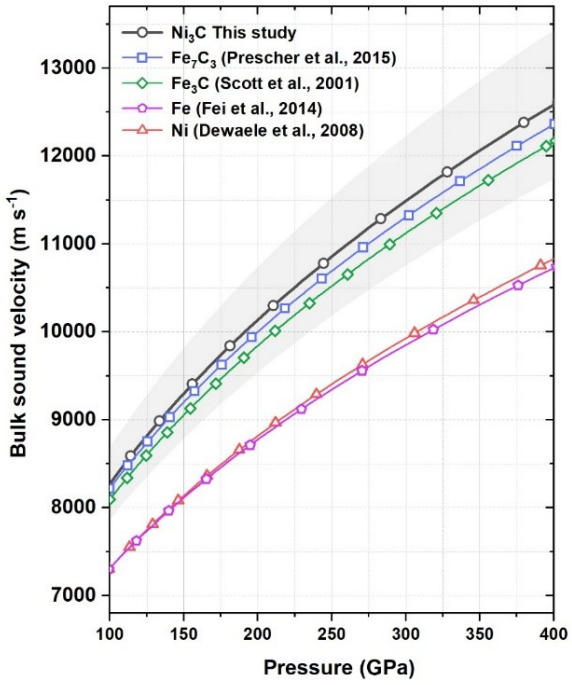

Figure 3.4.3. Calculated bulk sound velocity of Ni_3C as a function of pressure (this study, black solid line with circles); Fe_3C (green line with diamonds(Scott et al., 2001)) and Fe_7C_3 (blue line with squares (Prescher et al., 2015)); Ni (red line with triangles (Dewaele et al., 2008b)); Fe (purple line with pentagons (Fei et al., 2016)) at 293 K.

3.5. List of manuscripts and statement of authors' contribution

[1] T. Fedotenko (TF), L. Dubrovinsky (LD), G. Aprilis (GA), E. Koemets (EK), A. Snigirev (AS), I. Snigireva (IS), A. Barannikov (AB), P. Ershov (PE), F. Cova (FC), M. Hanfland (MH), N. Dubrovinskaia (ND). Laser heating setup for diamond anvil cells for *in situ* synchrotron and in house high and ultra-high pressure studies. **Review of Scientific Instruments, 90(10):104501, 2019 (DOI: 10.1063/1.5117786)**

The laser system described in the paper was developed by TF with the technical support of LD, ND, and GA. The synchrotron x-ray diffraction data were collected by TF, LD, EK, FC, MH and analyzed by TF. X-ray transmission microscopy data were collected by TF, LD, GA, EK, AS, IS, AV, PE and analyzed by AS, IS, AV, PE. All authors were involved in the data discussion. TF did a final assessment of the results and wrote the manuscript with help of other co-authors.

[2] T. Fedotenko (TF), D.S. Souza (DSS), S. Khandarkhaeva (SK), L. Dubrovinsky (LD) and N. Dubrovinskaia (ND). Isothermal Equation of State of Crystalline and Glassy Materials From Optical Measurements in Diamond Anvil Cells Dubrovinskaia. **Review of Scientific Instruments, 92: 063907, 2021 (DOI: 10.1063/5.0050190).**

The methodology was developed by TF with the support of LD and ND. All Matlab and Python scripts were written by TF and DSS. Samples were prepared by TF with help of SK and DSS. Data collection and analysis were conducted by TF, DSS. TF did a final assessment of the results and wrote the manuscript with contributions from all co-authors.

[3] T. Fedotenko (TF), S. Khandarkhaeva (SK), L. Dubrovinsky (LD), S. Chariton (SC), E. Koemets (EK), I. Koemets (IK), M. Hanfland (MH) and N. Dubrovinskaia (ND). Synthesis of palladium carbides and palladium hydride in laser-heated diamond anvil cells. **Journal of Alloys and Compounds 844:156179, 2020 (DOI: 10.1016/j.jallcom.2020.156179)**

Sample and DACs preparation were done by TF. The synchrotron X-ray diffraction experiments were conducted by TF, SK, SC, EK, IK, and MH. All experimental data were processed and analyzed by TF with the help of LD and ND. TF did a final assessment of the results and wrote the manuscript with contributions from all co-authors.

[4] T. Fedotenko (TF), S. Khandarkhaeva (SK), L. Dubrovinsky (LD), K. Glazyrin, P. Sedmak, and N. Dubrovinskaia (ND). Synthesis and compressibility of novel nickel carbide at pressures of Earth's outer core. **Minerals 11(5), 516, 2021 (DOI: 10.3390/min11050516)**

Sample preparation and laser heating were performed by TF and LD. Synchrotron single crystal X-ray diffraction data were collected by TF, SK, KG, LD, PS. All experimental data were analyzed by TF, SK. All authors were involved in the data discussion.TF did a final assessment of the results and wrote the manuscript with help of other co-authors.

4.References

Adams, B.D., Chen, A., 2011. The role of palladium in a hydrogen economy. Mater. Today 14, 282–289. https://doi.org/10.1016/S1369-7021(11)70143-2

Akahama, Y., Kawamura, H., 2006. Pressure calibration of diamond anvil Raman gauge to 310GPa. J. Appl. Phys. 100, 043516. https://doi.org/10.1063/1.2335683

Amin, S.A., Rissi, E.N., McKiernan, K., Yarger, J.L., 2012. Determining the equation of state of amorphous solids at high pressure using optical microscopy. Rev. Sci. Instrum. 83, 033702. https://doi.org/10.1063/1.3688656

Anderson, O.L., 1995. Equations of State of Solids for Geophysics and Ceramic Science. Oxford University Press, New Yourk.

Aprilis, G., Strohm, C., Kupenko, I., Linhardt, S., Laskin, A., Vasiukov, D.M., Cerantola, V., Koemets, E.G., McCammon, C., Kurnosov, A., Chumakov, A.I., Rüffer, R., Dubrovinskaia, N., Dubrovinsky, L., 2017. Portable double-sided pulsed laser heating system for time-resolved geoscience and materials science applications. Rev. Sci. Instrum. 88, 084501. https://doi.org/10.1063/1.4998985

Aquilanti, G., Pascarelli, S., Mathon, O., Muñoz, M., Narygina, O., Dubrovinsky, L., 2009. Development of micro-XANES mapping in the diamond anvil cell. J. Synchrotron Radiat. 16, 376–379. https://doi.org/10.1107/S0909049509007134

Bashir, N., Beckett, J. ~R., Hutcheon, I. ~D., Stolper, E. ~M., 1996. Carbon in the Metal of Iron Meteorites, in: Lunar and Planetary Science Conference, Lunar and Planetary Science Conference. p. 63.

Bassett, W.A., 2016. Diamond Anvil Cells: Laser heating of samples at high pressure: 50 years. Laser Focus World. https://www.laserfocusworld.com/articles/print/volume-52/issue-04/features/diamond-anvil-cells-laser-heating-of-samples-at-high-pressure-50-years.html

Bassett, W.A., 2001. The birth and development of laser heating in diamond anvil cells. Rev. Sci. Instrum. 72, 1270. https://doi.org/10.1063/1.1343861

Birch, F., 1952. Elasticity and constitution of the Earth's interior. J. Geophys. Res. 57, 227–286. https://doi.org/10.1029/JZ057i002p00227

Birch, F., 1947. Finite Elastic Strain of Cubic Crystals. Phys. Rev. 71, 809–824. https://doi.org/10.1103/PhysRev.71.809

Boehler, R., De Hantsetters, K., 2004. New anvil designs in diamond-cells. High Press. Res. 24, 391–396. https://doi.org/10.1080/08957950412331323924

Boehler, R., Musshoff, H.G., Ditz, R., Aquilanti, G., Trapananti, A., 2009. Portable laser-heating stand for synchrotron applications. Rev. Sci. Instrum. 80, 045103. https://doi.org/10.1063/1.3115183

Boehler, R., Nicol, M., Zha, C.S., Johnson, M.L., 1986. Resistance heating of Fe and W in diamond-anvil cells. Phys. B+C 139–140, 916–918. https://doi.org/10.1016/0378-4363(86)90728-X

Borodziński, A., Bond, G.C., 2006. Selective Hydrogenation of Ethyne in Ethene-Rich Streams on Palladium Catalysts. Part 1. Effect of Changes to the Catalyst During Reaction. Catal. Rev. 48, 91–144. https://doi.org/10.1080/01614940500364909

Brett, R., 1966. Cohenite in Meteorites: A Proposed Origin. Science (80-.). 153, 60–62. https://doi.org/10.1126/science.153.3731.60

Brown, J.M., Slutsky, L.J., Nelson, K.A., Cheng, L.-T., 1989. Single-crystal elastic constants for San Carlos peridot: An application of impulsive stimulated scattering. J. Geophys. Res. 94, 9485. https://doi.org/10.1029/JB094iB07p09485

Brownsberger, K., Ahart, M., Somayazulu, M., Park, C., Gramsch, S.A., Hemley, R.J., 2017. X-ray

Diffraction, Lattice Structure, and Equation of State of PdH x and PdD x to Megabar Pressures. J. Phys. Chem. C 121, 27327–27331. https://doi.org/10.1021/acs.jpcc.7b09290

Bugaev, A.L., Guda, A.A., Lazzarini, A., Lomachenko, K.A., Groppo, E., Pellegrini, R., Piovano, A., Emerich, H., Soldatov, A. V., Bugaev, L.A., Dmitriev, V.P., van Bokhoven, J.A., Lamberti, C., 2017. In situ formation of hydrides and carbides in palladium catalyst: When XANES is better than EXAFS and XRD. Catal. Today 283, 119–126. https://doi.org/10.1016/j.cattod.2016.02.065

Bykov, M., Bykova, E., Koemets, E., Fedotenko, T., Aprilis, G., Glazyrin, K., Liermann, H.-P., Ponomareva, A. V., Tidholm, J., Tasnádi, F., Abrikosov, I.A., Dubrovinskaia, N., Dubrovinsky, L., 2018. High-Pressure Synthesis of a Nitrogen-Rich Inclusion Compound ReN 8 · x N 2 with Conjugated Polymeric Nitrogen Chains. Angew. Chemie 130, 9186–9191. https://doi.org/10.1002/ange.201805152

Bykov, M., Chariton, S., Bykova, E., Khandarkhaeva, S., Fedotenko, T., Ponomareva, A. V., Tidholm, J., Tasnádi, F., Abrikosov, I.A., Sedmak, P., Prakapenka, V., Hanfland, M., Liermann, H., Mahmood, M., Goncharov, A.F., Dubrovinskaia, N., Dubrovinsky, L., 2020. Innenrücktitelbild: High-Pressure Synthesis of Metal–Inorganic Frameworks Hf 4 N 20 · N 2 , WN 8 · N 2 , and Os 5 N 28 · 3 N 2 with Polymeric Nitrogen Linkers (Angew. Chem. 26/2020). Angew. Chemie 132, 10753–10753. https://doi.org/10.1002/ange.202005697

Cadeville, M.C., Lerner, C., 1976. On the electronic structure of interstitial transition-metal based alloys with boron and carbon impurities. Philos. Mag. 33, 801–824. https://doi.org/10.1080/14786437608221917

Campbell, A.J., Seagle, C.T., Heinz, D.L., Shen, G., Prakapenka, V.B., 2007. Partial melting in the iron–sulfur system at high pressure: A synchrotron X-ray diffraction study. Phys. Earth Planet. Inter. 162, 119–128. https://doi.org/10.1016/j.pepi.2007.04.001

Canny, J., 1986. A Computational Approach to Edge Detection. IEEE Trans. Pattern Anal. Mach. Intell. PAMI-8, 679–698. https://doi.org/10.1109/TPAMI.1986.4767851

Chen, B., Li, Z., Zhang, D., Liu, J., Hu, M.Y., Zhao, J., Bi, W., Alp, E.E., Xiao, Y., Chow, P., Li, J., 2014. Hidden carbon in Earth's inner core revealed by shear softening in dense Fe 7 C 3. Proc. Natl. Acad. Sci. 111, 17755–17758. https://doi.org/10.1073/pnas.1411154111

Clegg, W., Blake, A.J., Cole, J.M., Evans, J.S.O., Main, P., Parsons, S., Watkin, D.J., 2009. Crystal Structure Analysis. Oxford University Press. https://doi.org/10.1093/acprof:oso/9780199219469.001.0001

Dewaele, A., Belonoshko, A.B., Garbarino, G., Occelli, F., Bouvier, P., Hanfland, M., Mezouar, M., 2012. High-pressure–high-temperature equation of state of KCl and KBr. Phys. Rev. B 85, 214105. https://doi.org/10.1103/PhysRevB.85.214105

Dewaele, A., Datchi, F., Loubeyre, P., Mezouar, M., 2008a. High pressure–high temperature equations of state of neon and diamond. Phys. Rev. B 77, 094106. https://doi.org/10.1103/PhysRevB.77.094106

Dewaele, A., Stutzmann, V., Bouchet, J., Bottin, F., Occelli, F., Mezouar, M., 2015. High pressure-temperature phase diagram and equation of state of titanium. Phys. Rev. B 91, 134108. https://doi.org/10.1103/PhysRevB.91.134108

Dewaele, A., Torrent, M., Loubeyre, P., Mezouar, M., 2008b. Compression curves of transition metals in the Mbar range: Experiments and projector augmented-wave calculations. Phys. Rev. B 78, 104102. https://doi.org/10.1103/PhysRevB.78.104102

Dorogokupets, P.I., Dewaele, A., 2007. Equations of state of MgO, Au, Pt, NaCl-B1, and NaCl-B2: Internally consistent high-temperature pressure scales. High Press. Res. 27, 431–446. https://doi.org/10.1080/08957950701659700

Drozdov, A.P., Eremets, M.I., Troyan, I.A., Ksenofontov, V., Shylin, S.I., 2015. Conventional superconductivity at 203 kelvin at high pressures in the sulfur hydride system. Nature 525, 73–76. https://doi.org/10.1038/nature14964

Dubrovinskaia, N., Dubrovinsky, L., 2003. Whole-cell heater for the diamond anvil cell. Rev. Sci. Instrum. 74, 3433–3437. https://doi.org/10.1063/1.1578151

Dubrovinskaia, N., Dubrovinsky, L., Solopova, N.A., Abakumov, A., Turner, S., Hanfland, M., Bykova, E., Bykov, M., Prescher, C., Prakapenka, V.B., Petitgirard, S., Chuvashova, I., Gasharova, B., Mathis, Y.-L., Ershov, P., Snigireva, I., Snigirev, A., 2016. Terapascal static pressure generation with ultrahigh yield strength nanodiamond. Sci. Adv. 2, e1600341. https://doi.org/10.1126/sciadv.1600341

Dubrovinsky, L., Dubrovinskaia, N., Abrikosov, I.A., Vennström, M., Westman, F., Carlson, S., van

Schilfgaarde, M., Johansson, B., 2001. Pressure-Induced Invar Effect in Fe-Ni Alloys. Phys. Rev. Lett. 86, 4851–4854. https://doi.org/10.1103/PhysRevLett.86.4851

Dubrovinsky, L., Glazyrin, K., McCammon, C., Narygina, O., Greenberg, E., Übelhack, S., Chumakov, A.I., Pascarelli, S., Prakapenka, V., Bock, J., Dubrovinskaia, N., 2009. Portable laser-heating system for diamond anvil cells. J. Synchrotron Radiat. 16, 737–741. https://doi.org/10.1107/S0909049509039065

Dubrovinsky, L.S., Dubrovinskaia, N.A., Swamy, V., Muscat, J., Harrison, N.M., Ahuja, R., Holm, B., Johansson, B., 2001. The hardest known oxide. Nature 410, 653–654. https://doi.org/10.1038/35070650

Dyson, J., 1960. Precise Measurement by Image-Splitting. J. Opt. Soc. Am. 50, 754. https://doi.org/10.1364/JOSA.50.000754

Dziewonski, A.M., Anderson, D.L., 1981. Preliminary reference Earth model. Phys. Earth Planet. Inter. 25, 297–356. https://doi.org/10.1016/0031-9201(81)90046-7

Errandonea, D., Meng, Y., Somayazulu, M., Häusermann, D., 2005. Pressure-induced transition in titanium metal: a systematic study of the effects of uniaxial stress. Phys. B Condens. Matter 355, 116–125. https://doi.org/10.1016/j.physb.2004.10.030

Fei, Y., Murphy, C., Shibazaki, Y., Shahar, A., Huang, H., 2016. Thermal equation of state of hcp-iron: Constraint on the density deficit of Earth's solid inner core. Geophys. Res. Lett. 43, 6837–6843. https://doi.org/10.1002/2016GL069456

Fei, Y., Ricolleau, A., Frank, M., Mibe, K., Shen, G., Prakapenka, V., 2007. Toward an internally consistent pressure scale. Proc. Natl. Acad. Sci. 104, 9182–9186. https://doi.org/10.1073/pnas.0609013104

Fiquet, G., Badro, J., Guyot, F., Bellin, C., Krisch, M., Antonangeli, D., Requardt, H., Mermet, A., Farber, D., Aracne-Ruddle, C., Zhang, J., 2004. Application of inelastic X-ray scattering to the measurements of acoustic wave velocities in geophysical materials at very high pressure. Phys. Earth Planet. Inter. 143–144, 5–18. https://doi.org/10.1016/j.pepi.2003.10.005

Friedrich, A., Winkler, B., Juarez-Arellano, E.A., Bayarjargal, L., 2011. Synthesis of Binary Transition Metal Nitrides, Carbides and Borides from the Elements in the Laser-Heated

Diamond Anvil Cell and Their Structure-Property Relations. Materials (Basel). 4, 1648–1692. https://doi.org/10.3390/ma4101648

Hirayama, Y., Fujii, T., Kurita, K., 1993. The melting relation of the system, iron and carbon at high pressure and its bearing on the early stage of the Earth. Geophys. Res. Lett. 20, 2095–2098. https://doi.org/10.1029/93GL02131

Jacobsen, S.D., 2002. Structure and elasticity of single-crystal (Mg,Fe)O and a new method of generating shear waves for gigahertz ultrasonic interferometry. J. Geophys. Res. 107, 2037. https://doi.org/10.1029/2001JB000490

Jacobsen, S.D., Spetzler, H., Reichmann, H.J., Smyth, J.R., 2004. Shear waves in the diamond-anvil cell reveal pressure-induced instability in (Mg,Fe)O. Proc. Natl. Acad. Sci. 101, 5867–5871. https://doi.org/10.1073/pnas.0401564101

Kantor, I., Prakapenka, V., Kantor, A., Dera, P., Kurnosov, A., Sinogeikin, S., Dubrovinskaia, N., Dubrovinsky, L., 2012. BX90: A new diamond anvil cell design for X-ray diffraction and optical measurements. Rev. Sci. Instrum. 83, 125102. https://doi.org/10.1063/1.4768541

Katayama, Y., Tsuji, K., Kanda, H., Nosaka, H., Yaoita, K., Kikegawa, T., Shimomura, O., 1996. Density of liquid tellurium under pressure. J. Non. Cryst. Solids 205–207, 451–454. https://doi.org/10.1016/S0022-3093(96)00259-1

Katayama, Y., Tsuji, K., Shimomura, O., Kikegawa, T., Mezouar, M., Martinez-Garcia, D., Besson, J.M., Häusermann, D., Hanfland, M., 1998. Density measurements of liquid under high pressure and high temperature. J. Synchrotron Radiat. 5, 1023–1025. https://doi.org/10.1107/S0909049597015239

Katsura, T., Tange, Y., 2019. A Simple Derivation of the Birch–Murnaghan Equations of State (EOSs) and Comparison with EOSs Derived from Other Definitions of Finite Strain. Minerals 9, 745. https://doi.org/10.3390/min9120745

Kawai, N., Endo, S., 1970. The Generation of Ultrahigh Hydrostatic Pressures by a Split Sphere Apparatus. Rev. Sci. Instrum. 41, 1178–1181. https://doi.org/10.1063/1.1684753

Khandarkhaeva, S., Fedotenko, T., Bykov, M., Bykova, E., Chariton, S., Sedmak, P., Glazyrin, K., Prakapenka, V., Dubrovinskaia, N., Dubrovinsky, L., 2020. Novel Rhenium Carbides at 200 GPa. Eur. J. Inorg. Chem. 2020, 2186–2190. https://doi.org/10.1002/ejic.202000252

Ko, Y.-H., Ahart, M., Ko, J.-H., Song, J., 2017. Investigation of polymorphism for amorphous and semi-crystalline poly (-ethylene terephthalate-) using high-pressure Brillouin spectroscopy. J. Korean Phys. Soc. 70, 382–388. https://doi.org/10.3938/jkps.70.382

Kupenko, I., Dubrovinsky, L., Dubrovinskaia, N., McCammon, C., Glazyrin, K., Bykova, E., Ballaran, T.B., Sinmyo, R., Chumakov, A.I., Potapkin, V., Kantor, A., Rüffer, R., Hanfland, M., Crichton, W., Merlini, M., 2012. Portable double-sided laser-heating system for Mössbauer spectroscopy and X-ray diffraction experiments at synchrotron facilities with diamond anvil cells. Rev. Sci. Instrum. 83, 124501. https://doi.org/10.1063/1.4772458

Kurnosov, A., Kantor, I., Boffa-Ballaran, T., Lindhardt, S., Dubrovinsky, L., Kuznetsov, A., Zehnder, B.H., 2008. A novel gas-loading system for mechanically closing of various types of diamond anvil cells. Rev. Sci. Instrum. 79, 045110. https://doi.org/10.1063/1.2902506

Kushiro, I., 1976. Changes in viscosity and structure of melt of NaAlSi 2 O 6 composition at high pressures. J. Geophys. Res. 81, 6347–6350. https://doi.org/10.1029/JB081i035p06347

Ladd, M., Palmer, R., 2013. Structure Determination by X-ray Crystallography. Springer US, Boston, MA. https://doi.org/10.1007/978-1-4614-3954-7

Laniel, D., Winkler, B., Fedotenko, T., Pakhomova, A., Chariton, S., Milman, V., Prakapenka, V., Dubrovinsky, L., Dubrovinskaia, N., 2020. High-Pressure Polymeric Nitrogen Allotrope with the Black Phosphorus Structure. Phys. Rev. Lett. 124, 216001. https://doi.org/10.1103/PhysRevLett.124.216001

Lavina, B., Dera, P., Kim, E., Meng, Y., Downs, R.T., Weck, P.F., Sutton, S.R., Zhao, Y., 2011. Discovery of the recoverable high-pressure iron oxide Fe4O5. Proc. Natl. Acad. Sci. 108, 17281–17285. https://doi.org/10.1073/pnas.1107573108

Lazzarini, A., Piovano, A., Pellegrini, R., Leofanti, G., Agostini, G., Rudić, S., Chierotti, M.R., Gobetto, R., Battiato, A., Spoto, G., Zecchina, A., Lamberti, C., Groppo, E., 2016. A comprehensive approach to investigate the structural and surface properties of activated carbons and related Pd-based catalysts. Catal. Sci. Technol. 6, 4910–4922. https://doi.org/10.1039/C6CY00159A

Lee, S.K., Fei, Y., Cody, G.D., Mysen, B.O., 2005. The application of 17O and 27Al solid-state (3QMAS) NMR to structures of non-crystalline silicates at high pressure, in: Advances in

High-Pressure Technology for Geophysical Applications. Elsevier, pp. 241–261. https://doi.org/10.1016/B978-044451979-5.50014-4

Liang, C., Wei, Z., Xin, Q., Li, C., 2000. Synthesis and characterization of nanostructured Mo2C on carbon material by carbothermal hydrogen reduction. pp. 975–982. https://doi.org/10.1016/S0167-2991(00)80742-9

Lin, J.-F., 2004. Absolute temperature measurement in a laser-heated diamond anvil cell. Geophys. Res. Lett. 31, L14611. https://doi.org/10.1029/2004GL020599

Litasov, K.D., Shatskiy, A.F., 2016. Composition of the Earth's core: A review. Russ. Geol. Geophys. 57, 22–46. https://doi.org/10.1016/j.rgg.2016.01.003

Liu, J., Lin, J.-F., Prakapenka, V.B., Prescher, C., Yoshino, T., 2016. Phase relations of Fe 3 C and Fe 7 C 3 up to 185 GPa and 5200 K: Implication for the stability of iron carbide in the Earth's core. Geophys. Res. Lett. 43, 12,415-12,422. https://doi.org/10.1002/2016GL071353

Liu, L.-G., Bassett, W.A., 1975. The melting of iron up to 200 kbar. J. Geophys. Res. 80, 3777–3782. https://doi.org/10.1029/JB080i026p03777

Liu, L., 1974. Silicate perovskite from phase transformations of pyrope-garnet at high pressure and temperature. Geophys. Res. Lett. 1, 277–280. https://doi.org/10.1029/GL001i006p00277

Lord, O.T., Walter, M.J., Dasgupta, R., Walker, D., Clark, S.M., 2009. Melting in the Fe–C system to 70 GPa. Earth Planet. Sci. Lett. 284, 157–167. https://doi.org/10.1016/j.epsl.2009.04.017

Manchester, F.D., San-Martin, A., Pitre, J.M., 1994a. The H-Pd (hydrogen-palladium) System. J. Phase Equilibria 15, 62–83. https://doi.org/10.1007/BF02667685

Manchester, F.D., San-Martin, A., Pitre, J.M., 1994b. The H-Pd (hydrogen-palladium) System. J. Phase Equilibria 15, 62–83. https://doi.org/10.1007/BF02667685

Mao, W.L., Meng, Y., Shen, G., Prakapenka, V.B., Campbell, A.J., Heinz, D.L., Shu, J., Caracas, R., Cohen, R.E., Fei, Y., Hemley, R.J., Mao, H. -k., 2005. Iron-rich silicates in the Earth's D'' layer. Proc. Natl. Acad. Sci. 102, 9751–9753. https://doi.org/10.1073/pnas.0503737102

Marini, C., Kantor, I., Mathon, O., Pascarelli, S., 2013. On-line laser heating setup for ED-XAS at

ID24: preliminary optical design and test results. High Press. Res. 33, 108–113. https://doi.org/10.1080/08957959.2012.748762

McDonough, W.F., 2003. Compositional Model for the Earth's Core, in: Treatise on Geochemistry. Elsevier, pp. 547–568. https://doi.org/10.1016/B0-08-043751-6/02015-6

McMurdie, H.F., Morris, M.C., Evans, E.H., Paretzkin, B., Wong-Ng, W., Ettlinger, L., Hubbard, C.R., 1986. Standard X-Ray Diffraction Powder Patterns from the JCPDS Research Associateship. Powder Diffr. 1, 64–77. https://doi.org/10.1017/S0885715600011593

Meng, Y., Hrubiak, R., Rod, E., Boehler, R., Shen, G., 2015. New developments in laser-heated diamond anvil cell with in situ synchrotron x-ray diffraction at High Pressure Collaborative Access Team. Rev. Sci. Instrum. 86, 072201. https://doi.org/10.1063/1.4926895

Mezouar, M., Rambert, N., Fiquet, G., Andrault, D., Sitaud, B., Loubeyre, P., Bauchau, S., Crichton, W., Boehler, R., Schultz, E., Blattmann, G., 2007. Double-sided laser heating system for in situ high pressure–high temperature monochromatic x-ray diffraction at the esrf . High Press. Res. 25, 71–83. https://doi.org/10.1080/08957950500076031

Morard, G., Boccato, S., Rosa, A.D., Anzellini, S., Miozzi, F., Henry, L., Garbarino, G., Mezouar, M., Harmand, M., Guyot, F., Boulard, E., Kantor, I., Irifune, T., Torchio, R., 2018. Solving Controversies on the Iron Phase Diagram Under High Pressure. Geophys. Res. Lett. 45. https://doi.org/10.1029/2018GL079950

Mysen, B.O., Virgo, D., 1994. Structure and Properties of Silicate Glasses and Melts; Theories and Experiment, in: Advanced Mineralogy. Springer Berlin Heidelberg, Berlin, Heidelberg, pp. 238–254. https://doi.org/10.1007/978-3-642-78523-8_14

Nakajima, Y., Takahashi, E., Suzuki, T., Funakoshi, K., 2009. "Carbon in the core" revisited. Phys. Earth Planet. Inter. 174, 202–211. https://doi.org/10.1016/j.pepi.2008.05.014

Narygina, O., Dubrovinsky, L.S., McCammon, C.A., Kurnosov, A., Kantor, I.Y., Prakapenka, V.B., Dubrovinskaia, N.A., 2011. X-ray diffraction and Mössbauer spectroscopy study of fcc iron hydride FeH at high pressures and implications for the composition of the Earth's core. Earth Planet. Sci. Lett. 307, 409–414. https://doi.org/10.1016/j.epsl.2011.05.015

Nespolo, M., 2011. Fundamentals of Crystallography , 3rd edition. By C. Giacovazzo, H. L. Monaco, G. Artioli, D. Viterbo, M. Milaneso, G. Ferraris, G. Gilli, P. Gilli, G. Zanotti and M.

Catti. Edited by C. Giacovazzo. IUCr Texts on Crystallography No. 15, IUCr/Oxford Univer. Acta Crystallogr. Sect. A Found. Crystallogr. 67, 561–563. https://doi.org/10.1107/S0108767311039523

Pellegrini, R., Agostini, G., Groppo, E., Piovano, A., Leofanti, G., Lamberti, C., 2011. 0.5wt.% Pd/C catalyst for purification of terephthalic acid: Irreversible deactivation in industrial plants. J. Catal. 280, 150–160. https://doi.org/10.1016/j.jcat.2011.03.012

Petitgirard, S., Spiekermann, G., Glazyrin, K., Garrevoet, J., Murakami, M., 2019. Density of amorphous GeO2 to 133 GPa with possible pyritelike structure and stiffness at high pressure. Phys. Rev. B 100, 214104. https://doi.org/10.1103/PhysRevB.100.214104

Petříček, V., Dušek, M., Plášil, J., 2016. Crystallographic computing system Jana2006: solution and refinement of twinned structures. Zeitschrift für Krist. - Cryst. Mater. 231. https://doi.org/10.1515/zkri-2016-1956

Poirier, J.-P., 1994. Light elements in the Earth's outer core: A critical review. Phys. Earth Planet. Inter. 85, 319–337. https://doi.org/10.1016/0031-9201(94)90120-1

Prakapenka, V.B., Kubo, A., Kuznetsov, A., Laskin, A., Shkurikhin, O., Dera, P., Rivers, M.L., Sutton, S.R., 2008. Advanced flat top laser heating system for high pressure research at GSECARS: application to the melting behavior of germanium. High Press. Res. 28, 225–235. https://doi.org/10.1080/08957950802050718

Prescher, C., Dubrovinsky, L., Bykova, E., Kupenko, I., Glazyrin, K., Kantor, A., McCammon, C., Mookherjee, M., Nakajima, Y., Miyajima, N., Sinmyo, R., Cerantola, V., Dubrovinskaia, N., Prakapenka, V., Rüffer, R., Chumakov, A., Hanfland, M., 2015. High Poisson's ratio of Earth's inner core explained by carbon alloying. Nat. Geosci. 8, 220–223. https://doi.org/10.1038/ngeo2370

Prescher, C., Prakapenka, V.B., 2015. DIOPTAS : a program for reduction of two-dimensional X-ray diffraction data and data exploration. High Press. Res. 35, 223–230. https://doi.org/10.1080/08957959.2015.1059835

Rao, C.N., Rao, K.K., 1964. Effect of temperature on the lattice parameters of some silver–palladium alloys. Can. J. Phys. 42, 1336–1342. https://doi.org/10.1139/p64-120

Reagan, M.M., Gleason, A.E., Liu, J., Krawczynski, M.J., Van Orman, J.A., Mao, W.L., 2018. The

effect of nickel on the strength of iron nickel alloys: Implications for the Earth's inner core. Phys. Earth Planet. Inter. 283, 43–47. https://doi.org/10.1016/j.pepi.2018.08.003

Rigaku Oxford Diffraction, 2018. CrysAlis Pro (v. 171.39.46).

Ringwood, A.E., 1960. Cohenite as a pressure indicator in iron meteorites. Geochim. Cosmochim. Acta 20, 155–158. https://doi.org/10.1016/0016-7037(60)90059-4

Schultz, E., Mezouar, M., Crichton, W., Bauchau, S., Blattmann, G., Andrault, D., Fiquet, G., Boehler, R., Rambert, N., Sitaud, B., Loubeyre, P., 2005. Double-sided laser heating system for in situ high pressure–high temperature monochromatic x-ray diffraction at the esrf. High Press. Res. 25, 71–83. https://doi.org/10.1080/08957950500076031

Scott, C., Jeanloz, R., 1984. Optical length determinations in the diamond-anvil cell. Rev. Sci. Instrum. 55, 558–562. https://doi.org/10.1063/1.1137791

Scott, H.P., Williams, Q., Knittle, E., 2001. Stability and equation of state of Fe 3 C to 73 GPa: Implications for carbon in the Earth's core. Geophys. Res. Lett. 28, 1875–1878. https://doi.org/10.1029/2000GL012606

A. Shatskiy, T. Katsura, K.D. Litasov, A.V. Shcherbakova, Y.M. Borzdov, D. Yamazaki, A. Yoneda, E. Ohtani, E. Ito. High pressure generation using scaled-up Kawai-cell, Physics of the Earth and Planetary Interiors, Volume 189, Issues 1–2, 2011, Pages 92-108. https://doi.org/10.1016/j.pepi.2011.08.001

Sheldrick, G.M., 2015. SHELXT – Integrated space-group and crystal-structure determination. Acta Crystallogr. Sect. A Found. Adv. 71, 3–8. https://doi.org/10.1107/S2053273314026370

Shen, G., Wang, L., Ferry, R., Mao, H., Hemley, R.J., 2010. A portable laser heating microscope for high pressure research. J. Phys. Conf. Ser. 215, 012191. https://doi.org/10.1088/1742-6596/215/1/012191

Shen, G., Wang, Y., Dewaele, A., Wu, C., Fratanduono, D.E., Eggert, J., Klotz, S., Dziubek, K.F., Loubeyre, P., Fat'yanov, O. V., Asimow, P.D., Mashimo, T., Wentzcovitch, R.M.M., 2020. Toward an international practical pressure scale: A proposal for an IPPS ruby gauge (IPPS-Ruby2020). High Press. Res. 40, 299–314. https://doi.org/10.1080/08957959.2020.1791107

Singh, A., Aynyas, M., Sanyal, S.P., 2009. High pressure behavior and structural properties of transition metal carbides. Phase Transitions 82, 576–586. https://doi.org/10.1080/01411590903211309

Skoskiewicz, T., 1972. Superconductivity in the palladium-hydrogen and palladium-nickel-hydrogen systems. Phys. Status Solidi 11, K123–K126. https://doi.org/10.1002/pssa.2210110253

Smith, K.H., Shero, E., Chizmeshya, A., Wolf, G.H., 1995. The equation of state of polyamorphic germania glass: A two-domain description of the viscoelastic response. J. Chem. Phys. 102, 6851–6857. https://doi.org/10.1063/1.469122

Solopova, N.A., Dubrovinskaia, N., Dubrovinsky, L., 2013. Raman spectroscopy of glassy carbon up to 60 GPa. Appl. Phys. Lett. 102, 121909. https://doi.org/10.1063/1.4798660

Stritzker, B., Buckel, W., 1972. Superconductivity in the palladium-hydrogen and the palladium-deuterium systems. Zeitschrift für Phys. A Hadron. Nucl. 257, 1–8. https://doi.org/10.1007/BF01398191

Syassen, K., 2008. Ruby under pressure. High Press. Res. 28, 75–126. https://doi.org/10.1080/08957950802235640

Tateno, S., Hirose, K., Ohishi, Y., Tatsumi, Y., 2010. The Structure of Iron in Earth's Inner Core. Science (80-.). 330, 359–361. https://doi.org/10.1126/science.1194662

Tateno, S., Komabayashi, T., Hirose, K., Hirao, N., Ohishi, Y., 2019. Static compression of B2 KCl to 230 GPa and its P-V-T equation of state. Am. Mineral. 104, 718–723. https://doi.org/10.2138/am-2019-6779

Teschner, D., Borsodi, J., Kis, Z., Szentmiklósi, L., Révay, Z., Knop-Gericke, A., Schlögl, R., Torres, D., Sautet, P., 2010. Role of Hydrogen Species in Palladium-Catalyzed Alkyne Hydrogenation. J. Phys. Chem. C 114, 2293–2299. https://doi.org/10.1021/jp9103799

Teschner, D., Borsodi, J., Wootsch, A., Revay, Z., Havecker, M., Knop-Gericke, A., Jackson, S.D., Schlogl, R., 2008. The Roles of Subsurface Carbon and Hydrogen in Palladium-Catalyzed Alkyne Hydrogenation. Science (80-.). 320, 86–89. https://doi.org/10.1126/science.1155200

Tew, M.W., Nachtegaal, M., Janousch, M., Huthwelker, T., van Bokhoven, J.A., 2012. The

irreversible formation of palladium carbide during hydrogenation of 1-pentyne over silica-supported palladium nanoparticles: in situ Pd K and L3 edge XAS. Phys. Chem. Chem. Phys. 14, 5761. https://doi.org/10.1039/c2cp24068h

Torchio, R., Boccato, S., Miozzi, F., Rosa, A.D., Ishimatsu, N., Kantor, I., Sévelin-Radiguet, N., Briggs, R., Meneghini, C., Irifune, T., Morard, G., 2020. Melting Curve and Phase Relations of Fe-Ni Alloys: Implications for the Earth's Core Composition. Geophys. Res. Lett. 47. https://doi.org/10.1029/2020GL088169

Uts, I., Glazyrin, K., Lee, K.K.M., 2013. Effect of laser annealing of pressure gradients in a diamond-anvil cell using common solid pressure media. Rev. Sci. Instrum. 84, 103904. https://doi.org/10.1063/1.4821620

Vinet, P., Ferrante, J., Rose, J.H., Smith, J.R., 1987. Compressibility of solids. J. Geophys. Res. 92, 9319. https://doi.org/10.1029/JB092iB09p09319

Van Valkenburg, A., Weir, C.E., Lippincott, E.R., Bunting, E.N., 1959. Infrared studies in the 1- to 15-micron region to 30,000 atmospheres. J. Res. Natl. Bur. Stand. Sect. A Phys. Chem. 63A, 55. https://doi.org/10.6028/jres.063A.003

Wood, B.J., 1993. Carbon in the core. Earth Planet. Sci. Lett. 117, 593–607. https://doi.org/10.1016/0012-821X(93)90105-I

Ye, Y., Shim, S.-H., Prakapenka, V., Meng, Y., 2018. Equation of state of solid Ne inter-calibrated with the MgO, Au, Pt, NaCl-B2, and ruby pressure scales up to 130 GPa. High Press. Res. 38, 377–395. https://doi.org/10.1080/08957959.2018.1493477

Yeung, M.T., Mohammadi, R., Kaner, R.B., 2016. Ultraincompressible, Superhard Materials. Annu. Rev. Mater. Res. 46, 465–485. https://doi.org/10.1146/annurev-matsci-070115-032148

Yonezawa, F., Ninomiya, T. (Eds.), 1983. Topological Disorder in Condensed Matter, Springer Series in Solid-State Sciences. Springer Berlin Heidelberg, Berlin, Heidelberg. https://doi.org/10.1007/978-3-642-82104-2

Zha, C.-S., Bassett, W.A., 2003. Internal resistive heating in diamond anvil cell for in situ x-ray diffraction and Raman scattering. Rev. Sci. Instrum. 74, 1255–1262. https://doi.org/10.1063/1.1539895

Zha, C.-S., Boehler, R., 1985. Melting of sodium and potassium in a diamond anvil cell. Phys. Rev. B 31, 3199–3201. https://doi.org/10.1103/PhysRevB.31.3199

Zha, C., Boehler, R., Young, D.A., Ross, M., 1986. The argon melting curve to very high pressures. J. Chem. Phys. 85, 1034–1036. https://doi.org/10.1063/1.451295

Zhang, L., Meng, Y., Yang, W., Wang, L., Mao, W.L., Zeng, Q.-S., Jeong, J.S., Wagner, A.J., Mkhoyan, K.A., Liu, W., Xu, R., Mao, H. -k., 2014. Disproportionation of (Mg,Fe)SiO3 perovskite in Earth's deep lower mantle. Science (80-.). 344, 877–882. https://doi.org/10.1126/science.1250274

Zhang, L., Wang, Y., Lv, J., Ma, Y., 2017. Materials discovery at high pressures. Nat. Rev. Mater. 2, 17005. https://doi.org/10.1038/natrevmats.2017.5

5.Manuscripts of the thesis

Section 5.A.

Laser heating setup for diamond anvil cells for *in situ* synchrotron and in house high and ultra-high pressure studies

T. Fedotenko [1,*], L. Dubrovinsky[2], G. Aprilis[1], E. Koemets[2], A. Snigirev[3], I. Snigireva[4], A. Barannikov[3], P. Ershov[3], F. Cova[4], M. Hanfland[4], N. Dubrovinskaia[1]

[1]*Material Physics and Technology at Extreme Conditions, Laboratory of Crystallography, University of Bayreuth, D-95440 Bayreuth, Germany*

[2]*Bayerisches Geoinstitut Universität Bayreuth, D-95440 Bayreuth, Germany*

[3]*Immanuel Kant Baltic Federal University, 236041 Kaliningrad, Russian Federation*

[4]*European Synchrotron Radiation Facility, F-38043 Grenoble, France*

Review of Scientific Instruments 90(10):104501, October 2019
DOI: 10.1063/1.5117786

Abstract:

The diamond anvil cell (DAC) technique combined with laser heating is one of the major methods for studying materials at high pressure and high temperature conditions. In this work, we present a transferable double-sided laser heating setup for diamond anvil cells with *in situ* temperature determination. The setup allows precise heating of samples inside a DAC at pressures above 200 GPa and could be combined with synchrotron beamline equipment. It can be applied to X-ray diffraction and X-ray transmission microscopy experiments. In the setup we use high-magnification and low working distance infinity corrected laser focusing objectives which enable us to decrease the size of the laser beam to less than 5 μm and achieve a maximum optical magnification of 320 times. All optical components of the setup were chosen to minimize chromatic and spatial aberrations for accurate *in situ* temperature determination by multiwavelength spectroscopy in the 570 – 830 nm spectral range. The flexible design of our setup allows the simple interchange of laser sources and focusing optics for application in different types of studies. The setup was successfully tested in house and at the high-pressure diffraction beamline ID15B at the European Synchrotron Radiation Facility. We demonstrate an example of application of the setup for the high pressure - high temperature powder diffraction study of PdH and X-ray transmission microscopy of platinum at 22(1) GPa as a novel method of melting detection in DACs.

[*] Corresponding author, email: TimofeyFedotenko@gmail.com

1. Introduction

Laser heating (LH) in diamond anvil cells (DACs) has been used for more than five decades[1,2] and there are many examples of its applications in geosciences for simulating the conditions of deep Earth's and planetary interiors, studies of physical and chemical processes at extreme conditions, and synthesis of novel materials[3–7]. The methodology of laser-heated diamond anvil cells (LHDAC) is well described in the literature[8]. Over the last decade, this technique has evolved into a useful and routine experimental method at synchrotron beamlines. The LHDAC technique has been coupled with different analytical methods such as powder and single crystal X-ray diffraction[9] (XRD), X-ray Absorption Spectroscopy (XAS)[10,11], nuclear inelastic scattering[12], and Synchrotron Mossbauer source (SMS)[13].

Dynamic development of the LHDAC technique during recent years has resulted in the emergence of portable laser heating systems which can be used for *in house* experiments in different scientific environments (i.e. simultaneously with resistivity measurements, Raman or Brillouin spectroscopy, etc.), are easily moved between synchrotron beamlines and coupled with different analytical techniques in response to modern scientific challenges. The portable laser heating system was invented by Boehler in 2009[8] and was successfully tested in XRD and XAS experiments at a synchrotron source. The one-side LH setup developed by Dubrovinsky et al[14] was successfully used for in house[15] studies and synchrotron *in situ* X-ray absorption and single-crystal XRD experiments[16]. However, the single-side heating leads to large temperature gradients within the samples that limit applications of the set up for thin samples.

The designs of the double-sided LH systems described by Kupenko et al. [13] and Aprilis et al. [17] are based on universal laser-heating heads (UniHeads, adapted finite cutting laser heads produced commercially by Precitec GmbH & Co. KG), which enable to decrease the size of a laser heating setup. The setups[13,17] are simple to install and may be used in experiments that require the rotation of DACs during data collection (particularly, for single-crystal XRD in laser-heated DACs).

The UniHead-based LH setups allow varying the size of the laser beam from 15 to 50 μm FWHM and providing 20 times magnification of the samples in DACs, which is sufficient

for the majority of conventional experiments with laser heating. However, in ultra-high pressure diamond anvil cells (with beveled anvils with small culet sizes, double-stage- or toroidal-type anvils, for example) the size of the pressure chamber is usually smaller than 15 μm and above 200 GPa samples, as a rule, are of about 3-4 μm in diameter. This requires tighter laser beam focusing, higher magnification, and better optical resolution. Moreover, even when using specially designed objectives (like GeoHeat 40_NIR), it is hard to reduce chromatic and spatial aberrations introduced by commercial optical elements of UniHeads (especially in the case of tight focusing) that could be crucial for temperature determination in laser heating experiments at temperatures above 3000 K.

In this paper, we present a transportable double-sided laser-heating setup for *in-house* and synchrotron experiments. It is designed to improve the accuracy of temperature measurements, to decrease the size of the laser spot focused on the sample, and to get higher magnification for precise heating in DACs at pressures above 200 GPa.
We demonstrate its application on examples of an *in situ* powder X-ray diffraction experiment and in situ X-Ray Transmission Microscopy (XRTM) imaging at the ID15B beamline of the European Synchrotron Radiation Facility (ESRF) and a series of in house experiments with the heating of samples in DACs above 200 GPa.

2. Design overview

2.1. General overview

The system consists of two identical parts which are schematically shown in FIG. 1.

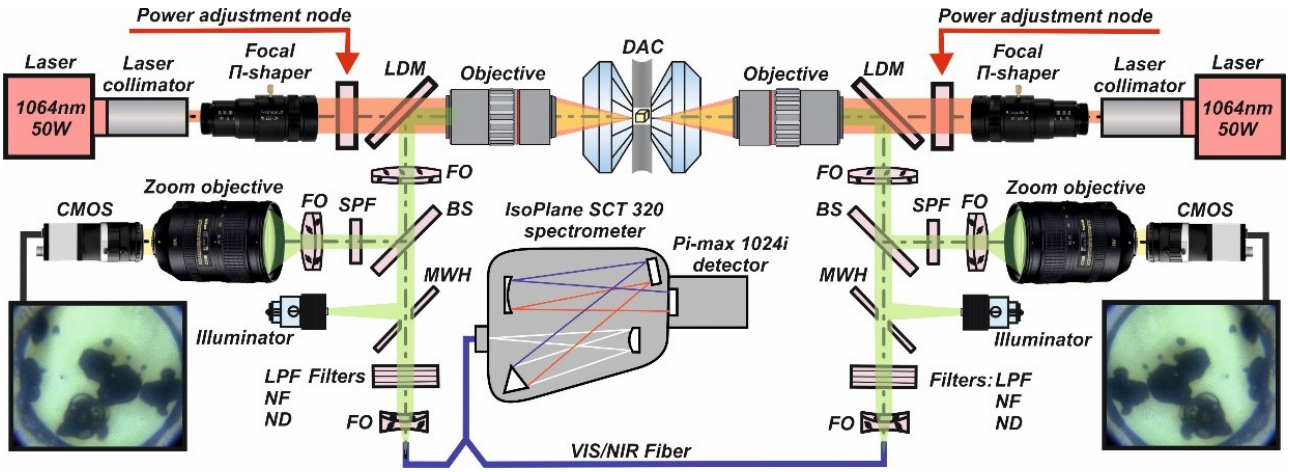

FIG. 1. Schematic diagram of the double-sided laser heating system for diamond anvil cells. LDMs are the long-pass dichromic mirrors; FOs are the focusing optics; BSs are 50/50 beam splitters; SPFs are the short-pass filters with a cut off at 800 nm; CMOSes are the cameras for optical observation; MWHs are the mirrors with a hole; LPFs are the long-pass filters with a cut-on wavelength of 550 nm; NFs are the notch filters at 1064 nm; NDs are neutral density filters.

Each of the parts includes the following nodes:

- NIR Laser
- Power control module based on two polarizing beam splitters and a half-wave plate.
- Focusing and shaping optics
- Observation module
- Temperature collection module

All major nodes are mounted on the breadboard and all optical components can be easily adjusted or modified depending on a type or specific needs of experiments.

2.2. Lasers

Independence of the different nodes of the system allows to quickly exchange the laser sources for experiments at a synchrotron facility or heating at the home institute (i.e. laser sources do not need to be transferred together with the laser-heating set up); however, the central wavelength of laser emission should be in the range of 1050-1070 nm, because all of the shaping and focusing optics described below are configured to work in this range.

The setup was tested with two different pairs of lasers. Each of the two SPI RedPower R4 Modulated Fiber Lasers of the first pair, one with a maximum power of 100 W and the other with 50 W, emits a randomly polarized Gaussian beam (TEM_{00}) with a full width at $1/e^2$ of 5 ± 0.5 mm (the central wavelength is 1070 ± 10 nm). The lasers can be operated in two modes: in a continuous-wave (CW) mode or a modulated with a maximum frequency of up to 100 kHz. The second pair of lasers are SPI G4 Pulsed Fiber Lasers with maximum output power up to 50 W and central emission wavelength at 1064nm ± 10nm. Each one has a Randomly polarized Gaussian beam (TEM_{00}) with an output beam diameter of 10 mm and divergence of 120 μrad. The lasers can be operated in both continuous-wave and pulsed modes. The minimum possible laser pulse FWHM 11 ns.

For both laser pairs, the output power level can be controlled by an external GUI, provided by the manufacturer. However, working in a low-power CW mode (power below 5 W) or working in short-pulse mode significantly increase the power control error of the laser feedback loop and strongly demand an external power control. For accurate power control, we use an external analogous optical controller, which will be described in detail in part 2.4.

Lasers are equipped with an additional low-power red laser source (630-680nm) for preliminary beam alignment and positioning on the sample.

2.3. Beam shaping and focusing

The setup demands focusing optics that can simultaneously operate in two spectral bands: NIR for focusing of the laser beam, and the optical range for collection of thermal emission and imaging of the sample.

Both sides of the LH setup are equipped with specially designed for TEM_{00} Focal-π Shapers (Focal-π Shaper_9_1064 by AdlOptica GmbH) to expand the output collimated laser beam and convert its initially spatial Gaussian distributed intensity to a flat-top π-shape profile.

To focus the laser beam in synchrotron experiments, we use a GeoHeat 40_NIR achromatic objective specially designed for laser heating applications in DACs. The GeoHeat 40_NIR working distance is 80 mm that provides enough space around a DAC for inserting additional optics to target the laser beam on a sample that is essential for *in situ* synchrotron X-ray diffraction and imaging in LHDAC studies. It minimizes chromatic aberrations in the spectral range of 600-900 nm used for temperature measurements and focuses the NIR laser beam[17,18].

By adjusting the Focal-π Shaper we reach the smallest FWHM of the laser beam of 20 μm, for a flat-top profile is used, and 10 μm FWHM for a Gaussian-shaped laser beam.

Experiments with ultra-high pressure DACs require tighter laser beam focusing, higher magnification, and better optical resolution as far as the size of a sample could be less than 5 μm. To overcome these challenges, we use a Mitutoyo 20x objective (Mitutoyo NIR infinity-corrected M Plan Apo B 20x) on both sides of the setup. Likewise, GeoHeat 40_NIR, the Mitutoyo 20x objective works in optical and NIR spectral ranges and allows focusing the laser beam to 5 μm FWHM on a sample. However, the working distance of the Mitutoyo 20x is 25 mm that does not provide enough space between the end of the objective and a DAC, and makes it inapplicable for *in situ* synchrotron experiments.

2.4. Power control node

It is well known that in pulsed fiber lasers there is a strict relation between the pulse shape and the energy. Therefore, pulsed LHDAC experiments require independent control of the laser pulse shapes and the energy of the individual pulses to provide stable heating and to avoid damaging the diamond anvils. The hardware control of the laser power in the CW mode does not allow access to the low-power region (between 0 to 5 W).

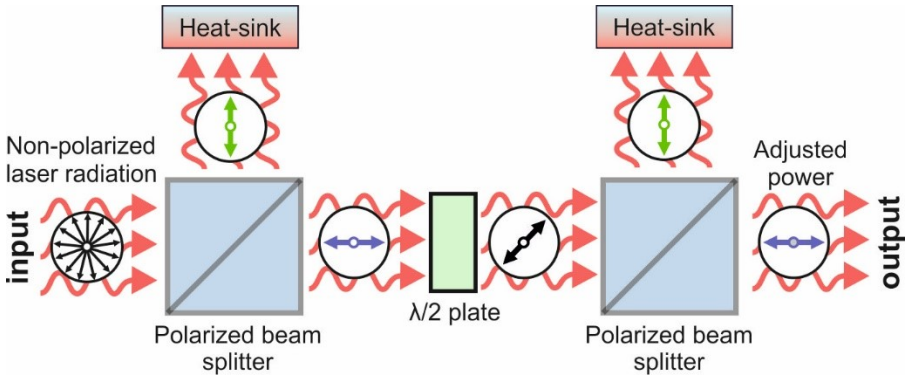

FIG. 2. Working principle of the power control node.

To resolve this problem, in our setup we used the polarization-based power control module schematically presented in FIG. 2. The module consists of two polarized NIR beam splitters (Thorlabs CCM1-PBS25-1064) and a half-wave plate (Thorlabs WPH05M-1064) mounted between them. The output power level is controlled by the rotation of the λ/2 wave plate in the range from 0 to 45 degrees to reach zero and maximum power, correspondingly. The part of laser radiation rejected from the beam splitters is dissipated on graphite-based beam blocks (Thorlabs LB2/M) to satisfy the safety regulations.

2.5. Observation

For imaging of the sample, we use high-resolution EYE © CMOS cameras (UI-3240CP), while the sample is illuminated by the LED (Thorlabs MCWHLP1). The image of the sample is obtained either in transmitted light, if the material in the sample chamber is at least partially transparent, or/and in reflected light. The light passes through a set of lenses into a zoom objective (Nikon AF-S NIKKOR 28-300mm f/3.5-5.6G ED VR Lens) projecting the image of the sample on the matrix of a CMOS camera. A short pass filter (Edmund #47-586) with a cut-off at 800 nm is placed in front of the zoom objective to protect the CMOS camera from laser reflections.

To determine the magnification of the optical system we imaged the Positive Test Target (Thorlabs R1DS1P, conformed to MIL-S-150A standard) with a maximum resolution of 228 lines per millimeter. The images of the test target for both objectives (GeoHeat_40 NIR and Mitutoyo NIR infinity-corrected M plan Apo B 20x) are presented in FIG. 3.

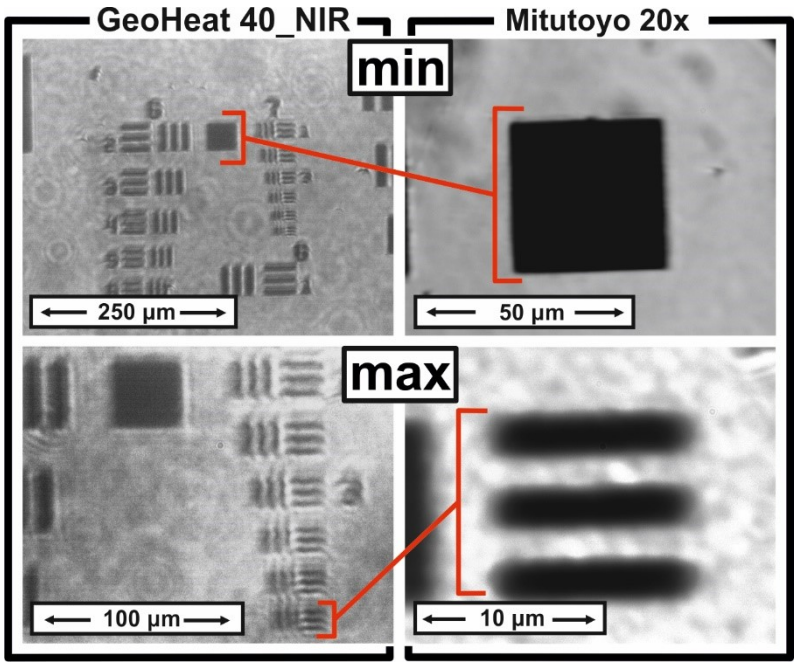

FIG. 3. The images of the test target plate at a minimum and maximum magnification for GeoHeat 40_NIR and Mitutoyo 20x objectives.

GeoHeat_40_NIR enables the magnification to be varied within approximately 20 to 35 times, while Mitutoyo 20x provides 80 to 320 times magnification. The spatial resolution of the final image with GeoHeat 40_NIR objective is limited to approximately 180 lines per millimeter at maximum magnification; Mitutoyo 20x provides spatial resolution higher than 228 lines per millimeter, which is the limit for the used test target.

2.6. Thermal radiation collection

Minimization of the optical distortions introduced by optical elements (lenses, beam splitters, filters) encountered by emitted radiation on the way to the spectrometer is necessary for precise temperature measurements in LHDAC experiments, and it is one of the primary goals for the designed setup.

To separate laser and optical observation/collection paths, we use a Thorlabs DMLP900 dichroic mirror, that reflects the visible wavelength light and transmits the laser-frequency light. The DMLP900 provides a flat top reflection spectral profile in the range of 600 – 850 nm. A 50/50 beam splitter (Thorlabs BSW10) installed on the observation path reflects half of the light intensity to the spectrometer for the temperature measurements, and the

other half of the light intensity goes eventually to the CMOS camera for simultaneous visual observations. The thermal radiation reflected by the beam splitter is focused on the optical fiber by an additional lens (Edmund #45-220) and guided into an IsoPlane SCT 320 spectrometer with a 1024x256 PI-MAX 4 camera (Princeton Instruments, Inc.). To prevent saturation of the detector by diffused laser radiation, we use a blocking notch filter with a central wavelength of 1064 nm (Edmund #86-128). For precise temperature measurements above 4500 K, a long-pass filter with the edge at 550 nm (Thorlabs FEL0550) is installed to avoid contamination of thermal emission spectra by second-order UV reflections.

Calibration of the system's response is performed by using calibrated tungsten lamps at temperatures of 1388, 1757, and 2361 K. The non-corrected spectra of a calibration lamp are presented in FIG. 4(a). Once the emission spectra are corrected and the effects introduced by optical components removed, the temperature can be determined by fitting the spectra in a given wavelength range (600-800 nm) to the Plank radiation function. Figure 4(b) demonstrates an example of fitting of thermal radiation spectra collected during heating of silicate perovskite ($Fe_{0.5}Mg_{0.5}Si_{0.5}Al_{0.5}O_3$) at 65(2) GPa inside a DAC.

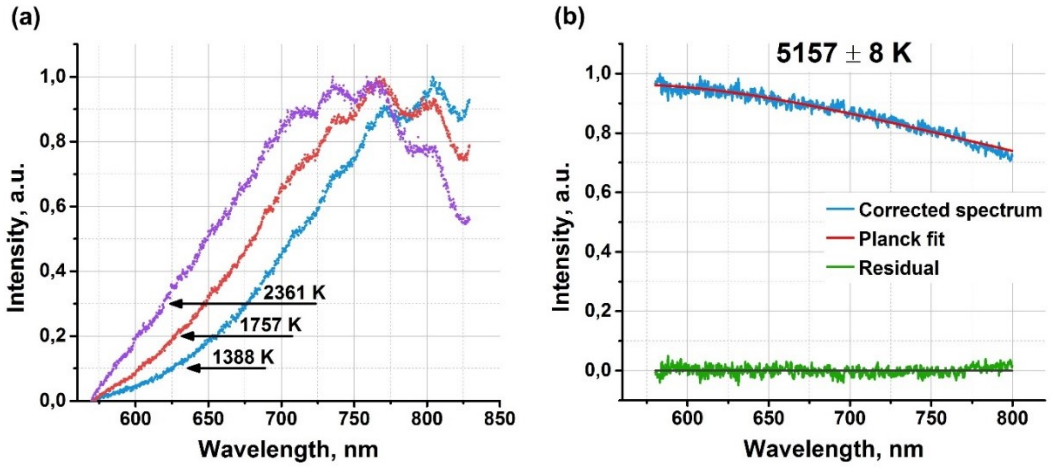

FIG. 4. Temperature determination procedure. (a) Normalized spectra of a calibration lamp at 1388, 1757, and 2361 K. (b) Example of temperature determination of heated silicate perovskite (Fe0.5Mg0.5Si0.5Al0.5O3) at 65(2) GPa inside a DAC using the gray body approximation of Planck's law. The error of measured temperature corresponds to the standard deviation from the fit.

3. Examples of application

3.1. Ultra-high pressure LH

In conventional LH-DAC experiments, the size of the laser beam is ranged from 10 to 50 μm FWHM. However, LH- DAC experiments at pressures over 200 GPa require tighter focusing of the laser beam as far as the size of the sample is about 3-4 μm in diameter. Furthermore, to distinguish the sample from the environment during the heating it is necessary to have high magnification and optical resolution of the image projected on the camera sensor.

During in-house LH experiments, the setup is mounted on the optical table as shown in FIG. 5.

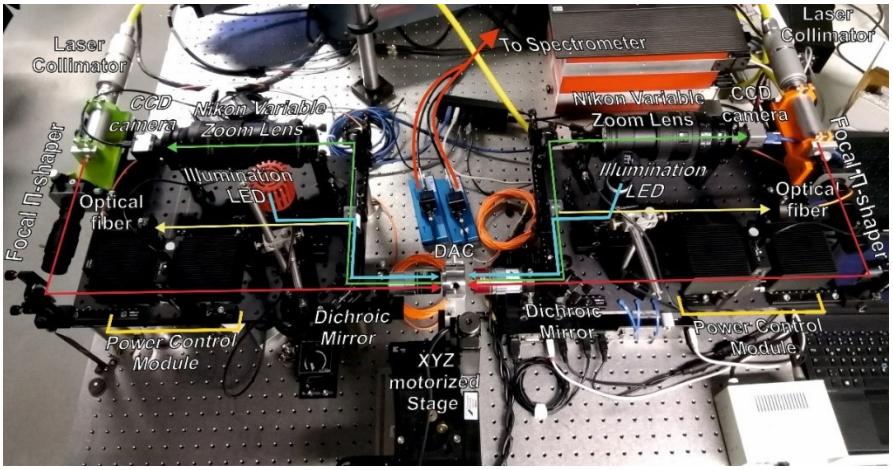

FIG. 5. Configuration of the LH setup for in house experiments

The setup was successfully tested in DAC experiments with 40-μm culet size anvils (pressure chambers are about 10 to 20 μm in diameter, characteristic sample sizes of about 5 μm) at pressures over 200 GPa. FIG. 6 shows an image of the DAC pressure

chamber during laser heating of NiO in a Ne pressure medium at 230(5) GPa and 2500±150 K.

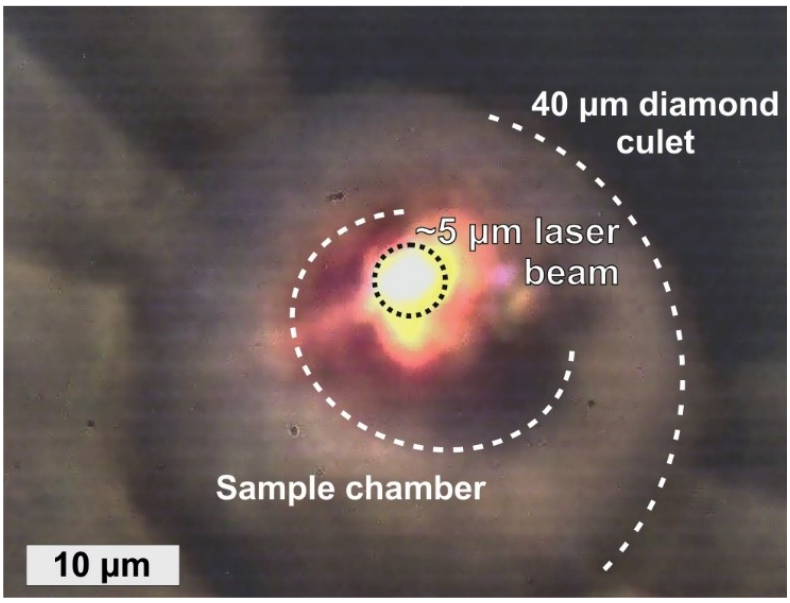

FIG. 6. Image of the sample chamber during laser heating of NiO in Ne as pressure transmitting medium at 230(5) GPa and 2700±150 K. Beveled diamond anvils have culet size of 40 µm in diameter.

3.2. *Combination with synchrotron techniques*

The transportability of the system was demonstrated during a series of experiments using X-ray diffraction and imaging at synchrotron X-ray source coupled with LHDAC at the High Pressure Diffraction beamline (ID15B) of the European Synchrotron Radiation Facility (ESRF). The system was transported to the ESRF and mounted in the experimental hutch of the beamline. The system's assembling and alignment take 8 to 10 hours before the experiment. To save experimental time the installation can be performed in advance, during a maintenance time, or shut down.

The geometry of the system was partially modified for synchrotron use, (FIG. 7) to enable simultaneous XRD and LH. All major nodes of the LH setup from the upstream (labeled (5) in FIG. 7) and downstream (labeled (6) in FIG. 7) sides were mounted on optical breadboards and installed on movable 3-axis stages. In lack of free space close to the 3D-stage with the DAC, focusing and targeting optics (labeled (4) in FIG. 7) were installed on rails and placed 300 mm away from the main breadboards.

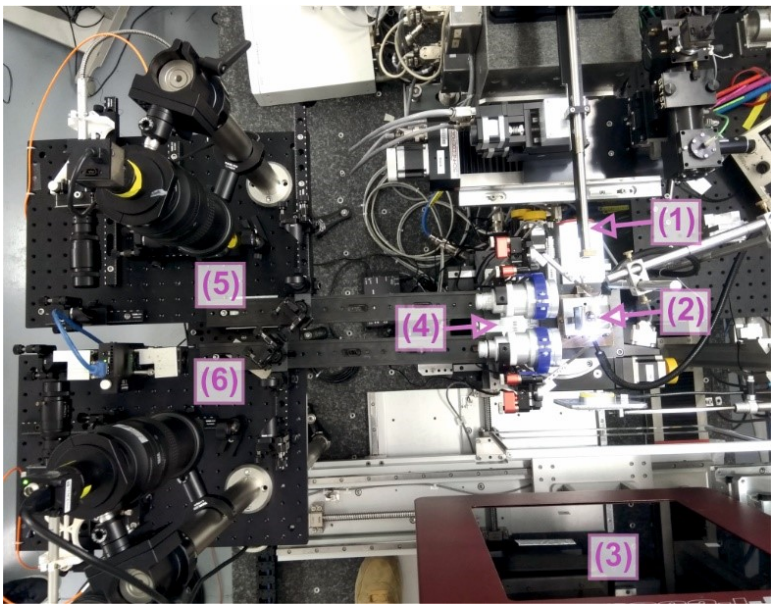

FIG. 7. (1) X-ray beam pinhole; (2) DAC; (3) Mar555 detector; (4) Focusing and targeting optics; (5) upstream breadboard; (6) downstream breadboard.

To direct the laser beam to the sample from both sides of the DAC, we used two graphite mirrors placed in front of each of the GeoHeat 40_NIR objectives (FIG. 8). As X-ray absorption of the carbon mirror is low, there is no problem if X-rays hit the mirror at the upstream side, which is positioned at ~45-degrees to both the laser beam and the X-ray beam. From the downstream side, the mirror is placed at ~40 degrees to the laser beam to prevent X-rays from heating the mirror and to avoid diffuse scattering from carbon. For precise positioning of the laser beam on the sample during the experiment, both mirrors were fixed on piezo mirror mounts (Newport 8821).

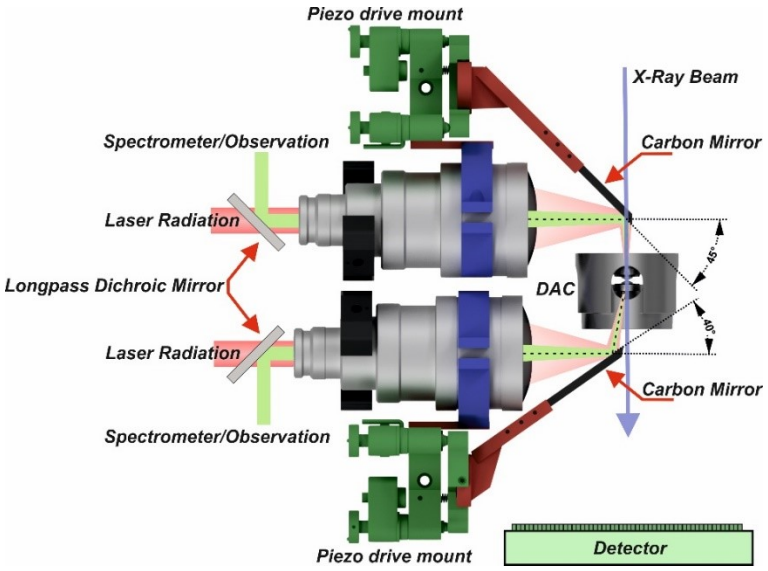

FIG. 8. Scheme of the laser beam targeting on the sample inside DAC in experiments with synchrotron X-ray radiation at ID15B (ESRF). The upstream carbon mirror is positioned at ~45 degrees to the laser beam. To prevent X-rays from hitting the mirror resulting in diffuse scattering from carbon on the detector, the downstream mirror is positioned at ~ 40 degrees to the laser.

3.2.1. Synthesis and behavior of palladium hydride (PdH) at high P-T

Palladium is a transition metal well known for its exceptional ability to absorb hydrogen in the bulk[19,20], forming *fcc*–structured PdH_x compounds. Along with some other transition metal polyhydrides, palladium hydrides PdH_x are known for their superconducting properties.[21–23]

As a part of our studies of the Pd-H system at high pressure, we investigated the behavior of PdH_x at high P-T conditions using LHDAC with *in situ* synchrotron X-ray diffraction. To synthesize this palladium hydride, a piece of Pd foil was loaded inside a sample chamber of a BX90-type diamond anvil cell equipped with Boehler–Almax type diamonds (culet diameter 250 μm) and a rhenium gasket. To form the sample chamber, a rhenium gasket was pre-indented to 25 μm thickness and a hole of 100 μm in diameter was drilled in the center of the indentation. Paraffin oil was used as both a pressure-transmitting medium and a source of hydrogen for the synthesis. The sample was compressed up to 39(2) GPa and laser-heated from both sides at 1500±100 K. The *fcc*-structured PdH_x formed

due to a reaction between Pd and paraffin oil. The unit cell parameter was found to be 60.18 ± 0.05 Å^3 from synchrotron X-ray diffraction data (FIG. 9) obtained at the ID15B synchrotron beamline at the ESRF (λ = 0.4117 Å, Mar555 flat panel detector). The X-ray diffraction images at ambient temperature were collected during continuous rotation of the DAC from – 20° to + 20° ω.

Within the uncertainty of experimental data, the unit cell volume of synthesized PdH_x (60.18 ± 0.05 Å^3) is consistent with that for PdH (x=1) (60.1 ± 0.1 Å^3) calculated from the PdH equation of state[24], thus, we consider for our sample x to be equal to 1. As seen in FIG. 9, after heating, not only palladium hydride but also diamond could be detected in the pressure chamber.

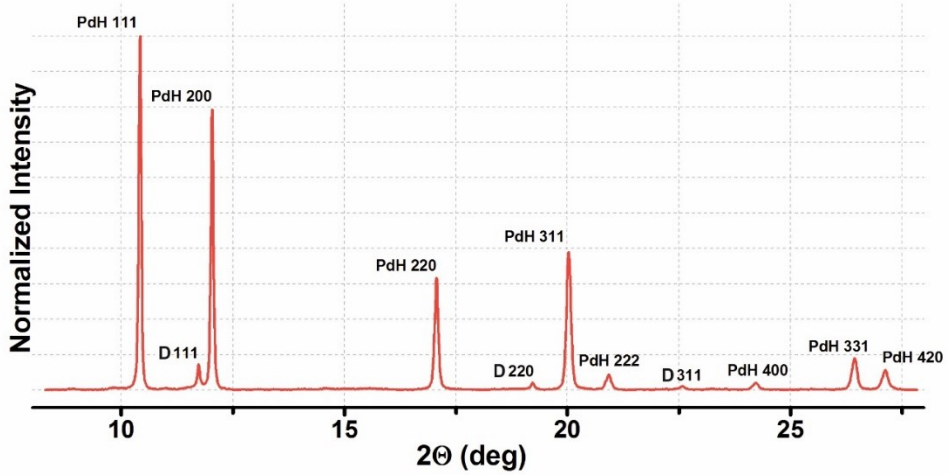

FIG. 9. A diffraction pattern of palladium hydride at 39 (2) GPa and ambient temperature. The fcc PdHx (x≈1) along with diamond was formed after laser heating of Pd in paraffin at 1500±200 K and 39(2) GPa. Indexes of the diffraction peaks of palladium hydride (PdH) and diamond (D) are designated (λ = 0.4117 Å). The unit cell volume of PdH is 60.18 ± 0.05 Å^3.

To check the stability of the synthesized PdH under high P-T conditions, we collect X-ray diffraction during LH at 2000±200 K and 39(2) GPa. The diffraction pattern of the sample at 2000±200 K (FIG. 10a) doesn't have any other reflections aside from those of cubic PdH and diamond. The unit cell parameters of palladium hydride before and after heating appeared to be the same (FIG. 10b) that could give evidence that the amount of hydrogen in PdH didn't change during heating and the shift of the position of the (111) reflection of

cubic PdH upon heating to 2000±200 K at 39(2) GPa was attributed only to the expansion of the PdH lattice.

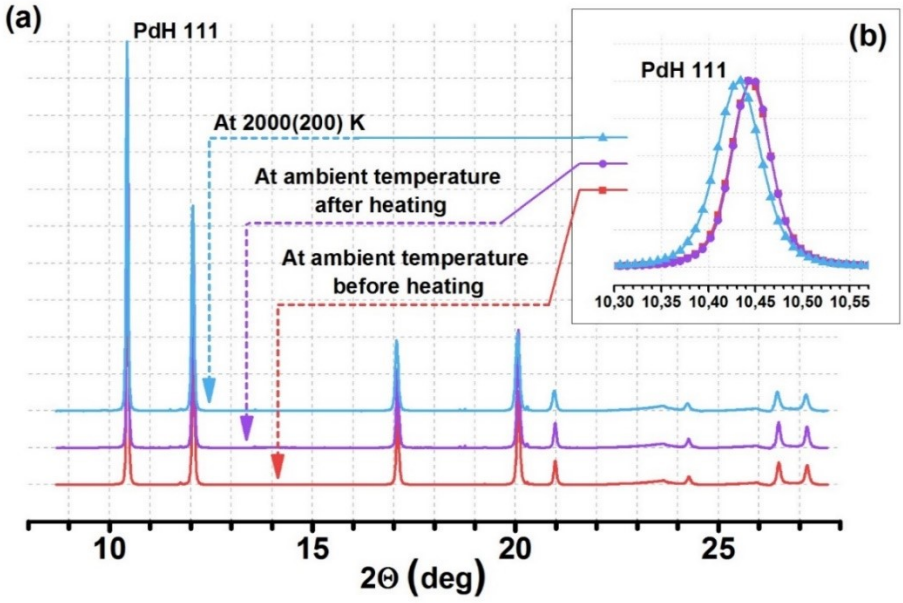

FIG. 10. (a) The diffraction patterns of the PdH sample at 39(2) GPa. (b) The shift of the position of the (111) reflection of the cubic PdH upon heating to 2000±200 K at 39(2) GPa. The position of the (111) reflection remains the same before and after heating. (λ = 0.4117 Å)

According to the XRD, the unit cell volume increased from 60.18(5) A^3 at room temperature (298 K) to 60.42(5) A^3 at 2000±200 K. This gives for PdH at 39(2) GPa a volumetric thermal expansion coefficient of 2.3 (±0.4) 10^{-6} 1/K, which is significantly lower than that of Pt (20.1(±0.5) 10^{-6} 1/K)[25] at similar conditions (39 GPa at heating up to 1900 K).

To our knowledge, the thermal behavior of Pd and Pd-hydrides at high pressure has not been studied so far, therefore we compare our data with those known for Pt, as the thermal expansion of Pt is close to that of Pd at atmospheric pressure. One of the possible explanations of the observed large difference in the thermal expansion coefficients of Pt and PdH at high pressure can be related to the chemical behavior of PdH on heating. Indeed, if PdH loses hydrogen at high temperature, this should lead to a decrease of the unit cell volume, compensating for the effect of the thermal expansion, and thus effectively

lower thermal expansion coefficient. During cooling, hydrogen can be accommodated up to the same amount as before. Thus, there is a possibility that the effect of the volume change under heating can not be exclusively attributed to the thermal expansion.

3.2.2. In situ X-ray Transmission Microscopy in LH-DACs

In this part, we describe the application of our transportable laser-heating setup for visualization of processes in DAC at high temperature using X-ray Transmission Microscopy (XRTM). Particularly, on the beamline ID15B (ESRF) we observed *in situ* melting of platinum in a DAC at high pressures.

Several methods of detection of melting in laser-heated DACs are known. In particular, it can be done due to optical observations, XRD, X-ray absorption, or Raman measurements.[8,26–28] Search for signs of melting on surfaces of recovered materials using Scanning Electron Microscope and Focus Ion Beam techniques, put forward by Boehler et al.[29,30], is helpful, but time and labor-consuming. Moreover, distinguishing between melting and re-crystallization textures, and the analysis of possible chemical contamination by carbon are not always trivial. Considerable difficulties associated with the detection of melting at high pressures result in significant inconsistencies in reported melting curves for the same materials.[31,32]

Each of the current methods of melting detection in LHDACs is associated with specific challenges, which can lead to ambiguities. *In situ* melting detection at temperatures above ~2000 K is possible by visual observation of fluid motion in a speckle interference pattern[33] but linked to the subjective judgment of the observer.[34] The image analysis procedure for quantification of changes in speckle interference pattern appeared last years.[35] Identification of melting using X-ray diffraction is in general possible at synchrotron beamlines with an appropriate setup[27,28]. In this case, melting is manifested either by the disappearance of Bragg reflections and/or by the appearance of diffuse scattering due to the short-range order in the liquid state. However, the disappearance of reflections on still X-ray images may be a result of re-crystallization (without melting) of the sample[31]. To produce a detectable signal, the amount of melted liquid in the sample should be significant, and the melt has to be stable for some time in a complex and highly thermally and chemically inhomogeneous environment of DAC. Moreover, experiments

can be complicated due to possible chemical reactions with the pressure medium or the diamond anvils[36,37]. The detection of melting using X-ray absorption suffers from at least the same problems.

The development of XRTM using compound refractive lenses at ID15B opened up new perspectives for studies in DACs. We demonstrated[38,39], particularly, that with XRTM it is possible to get an image with sub-micron resolution, which is hardly possible with conventional optics in the visual light.

X-ray energy of 30 keV was selected using a cryogenically cooled Si (111) horizontally deflected monochromator with $\Delta\lambda/\lambda \sim 10^{-4}$. Transmission X-ray Microscopy was realized using compound refractive lenses (CRL)[40], according to the scheme shown in FIG. 11. The design of the beamline allows to translation of the diffraction detector out of the beam and introduces an additional X-ray objective lens to perform X-ray microscopy. The objective lens assembly consists of 66 aluminum and 45 beryllium parabolic refractive lenses. The lenses of both types have the radius of the parabola apex of 50 μm. The objective lens was placed on the stage with all necessary translations and rotations needed for the lens alignment.

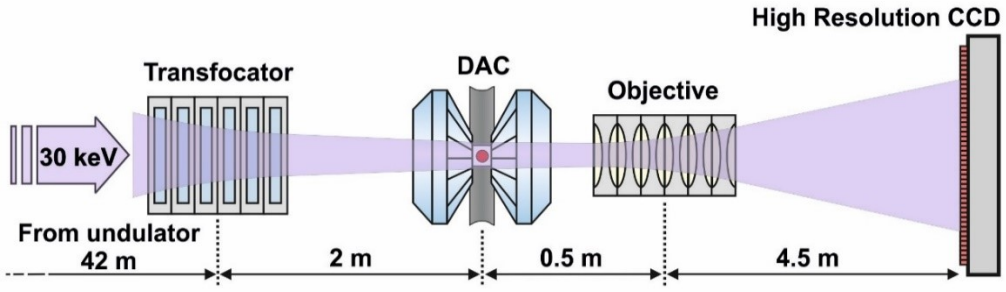

FIG. 11. Experimental layout for X-ray microscopy experiments

The DAC was located at a distance of 50 cm in front of the objective. X-ray images were recorded with a high-resolution PCO X-ray CCD camera with 0.74 μm pixel size, which was installed at a distance of about 5 m from the DAC. Therefore, a magnification of about 10 was achieved. The transfocator, which was located at 44 m from the undulator, was used to provide appropriate illumination on the sample.[41–43] It should be noted that it is very important to match the illumination area on the sample with sample sizes during microscopy experiments. This was achieved by varying the number of lenses in the transfocator. Such an experimental arrangement allows to preserve beam coherence and

gives unique opportunities for the realization of X-ray phase contrast microscopy with a spatial resolution down to 200 nm [38,39,44–46].

X-ray phase contrast microscopy allows to monitor the position and size of the sample; map the sample and find the area of interest; investigate the morphology of the sample during phase transitions, chemical reactions or melting of the sample and study mechanical stresses in DACs and a failure mechanism under ultra-high pressures. It is necessary to point out that the proposed beamline concept can be easily adapted for the upgraded Extremely Brilliant Source (EBS) simply by changing the number of individual lenses in the transfocators.

To demonstrate the feasibility of in situ XRTM in LHDACs we performed an experiment aiming to detect the melting of Pt. Platinum was chosen, because it is chemically inert, and possible chemical reactions, that could affect the result, can be excluded. The relatively low melting temperature of Pt simplifies the experiment and its melting curve has been already experimentally established[47]. A piece of Pt foil was clamped between two thin layers of NaCl from both sides and loaded inside a sample chamber of a BX90-type diamond anvil cell equipped with Boehler–Almax type diamonds (with culet diameter of 250 μm). To form the sample chamber, a rhenium gasket was pre-indented to 25 μm thickness and a hole with a 110-μm diameter was drilled in the center of the indent. NaCl was used as a pressure-transmitting medium and a thermal insulator to minimize the dissipation of heat through the diamonds. The sample was compressed up to 22(1) GPa. We heated the sample for 200 seconds simultaneously recording a series of XRTM images with 1-second exposure time and measuring the temperature using spectroradiometry. FIG. 12 represents the XRTM images of the sample during the heating, as seen the sample changes its shape and texture.

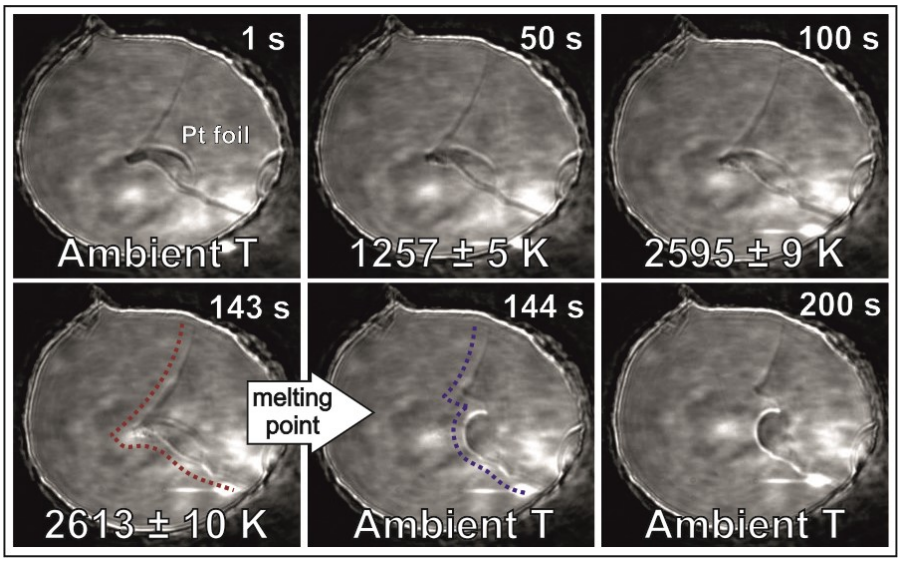

FIG. 12. XRTM images of the sample chamber taken during the heating process. Each image was collected with 1 second exposure time. Red and blue dotted lines represent the shape of the Pt foil before and after melting respectively. The melting moment was detected between 143th and 144th seconds by observation of the Pt foil shape. The melting temperature of Pt at 22 (1) GPa is 2613±10 K. Presented errors correspond to the standard deviation from the fit.

For the first 143 seconds, the laser power was slowly increasing. Significant change of the shape of Pt foil caused by its melting was detected between 143th and 144th seconds. We observe the formation of Pt droplet (the size is around 10 μm) from initial Pt foil, which excludes simple recrystallization. XRTM tomography collected after LH proves the formation of a droplet is shown in FIG. 13 (Multimedia view).

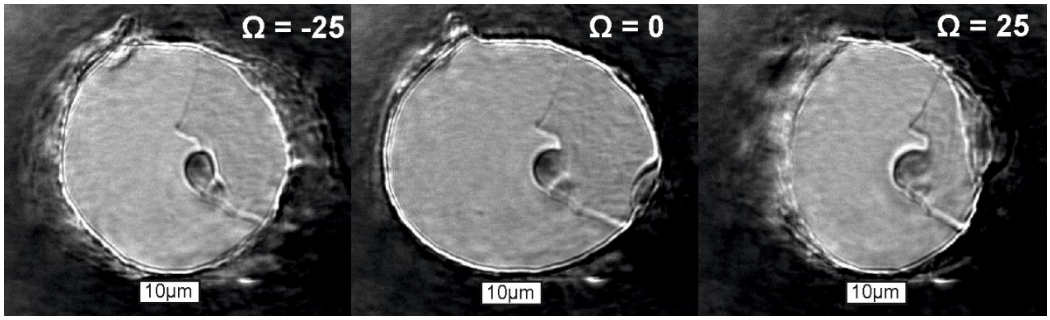

FIG. 13. XRTM images of the DAC sample chamber at different angular orientations of the DAC (Multimedia view).

Before the melting event, all visual changes in the texture and shape of the Pt foil were caused by the warming up of the sample chamber and its relaxation. The temperature collected at the last moment before melting was 2613 (10) K. After melting, the sample moved out of the laser beam and no thermal emission was present.

The diffraction pattern of the heated area recorded after LH is presented in FIG. 14. It proves the absence of a chemical interaction between the Pt sample and its surrounding. The melting temperature of Pt at 22(1) GPa (2613 ±10 K) obtained in the experiment described above due to a combination of XRTM with LH-DACs is in good agreement with the literature data (2583±97 K)[47].

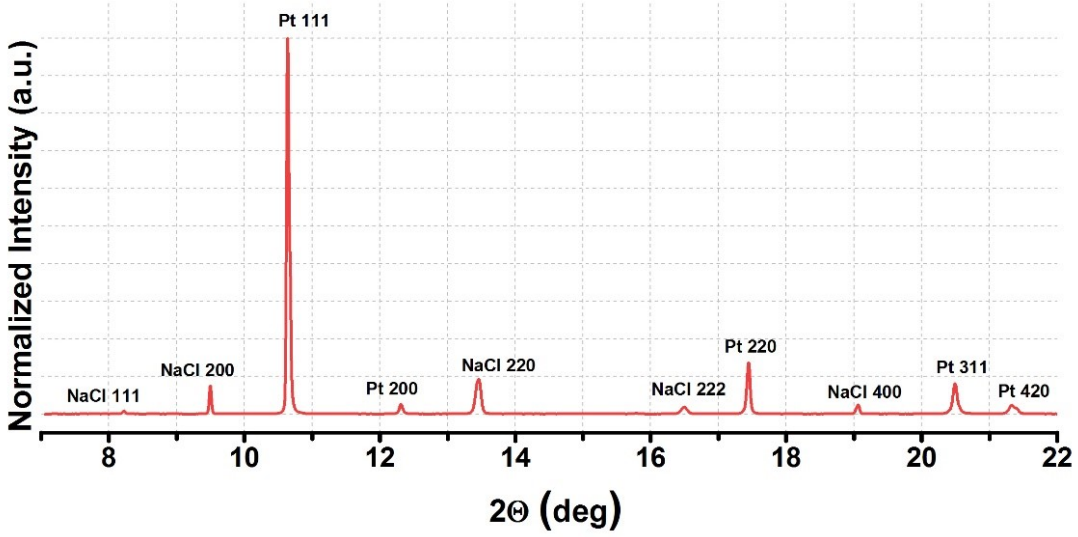

FIG. 14. The diffraction pattern was taken from the melted area of the sample at 22(1) GPa after heating. Pure Pt and B1-NaCl are the only materials detected by XRD.

4. *Conclusion*

A transportable double-sided laser heating system enabling simultaneous visual observation of a sample, its heating and temperature measurements have been developed. The configuration of the system can be easily changed: the geometry and optical components can be modified for any specific needs. The use of Mitutoyo 20x objectives as focusing optics for in-house experiments allows to decrease beam size of the laser beam to 5 μm and improves the optical quality of imaging that opens new opportunities in LHDAC experiments at pressures above 200 GPa. Using conventional Nikon camera lenses as a zoom objective allows varying the optical magnification of the

setup from 80 to 320 times with optical resolution significantly higher than 228 lines per millimeter. For accurate temperature determination by spectroradiometry method, optical components of the system were selected to minimize the optical distortions (such as chromatic aberrations, etc.), increase the bandwidth window of collected thermal radiation spectra to 570-830 nm. Due to external control of the laser power, the energy of the laser pulse can be changed independently on its shape, as necessary for pulsed LH experiments. The flexibility and transportability of the system, as well as the possibility to couple it with various techniques at synchrotron facilities, have been successfully tested in a study of PdH behavior at high P-T conditions by means of powder X-ray diffraction and development of melting detection by XRTM on the beamline ID15B at the ESRF. The system can be assembled and aligned by users after basic training. All components of the system are commercially available that making it a ready solution for duplication.

5. Acknowledgments

N.D. and L.D. thank the Federal Ministry of Education and Research, Germany (BMBF, grant no. 5K16WC1) and the Deutsche Forschungsgemeinschaft (DFG projects DU 954-11/1, DU 393-9/2, and DU 393-13/1) for financial support. A.S., A.B., and P.E. are very grateful for financial support by Russian Science Foundation (Project N^0. 19-72-30009). A.B. expresses gratitude to the Russian Academic Excellence Project at the Immanuel Kant Baltic Federal University for the financial support for his travel.

6. References

[1] W.A. Bassett, Rev. Sci. Instrum. **72**, 1270 (2001).

[2] W.A. Bassett, Laser Focus World (2016).

[3] L. Liu, Geophys. Res. Lett. **1**, 277 (1974).

[4] Y. Meng, R. Hrubiak, E. Rod, R. Boehler, and G. Shen, Rev. Sci. Instrum. **86**, 072201 (2015).

[5] B. Lavina, P. Dera, E. Kim, Y. Meng, R.T. Downs, P.F. Weck, S.R. Sutton, and Y. Zhao, Proc. Natl. Acad. Sci. **108**, 17281 (2011).

[6] L. Zhang, Y. Meng, W. Yang, L. Wang, W.L. Mao, Q.-S. Zeng, J.S. Jeong, A.J.

Wagner, K.A. Mkhoyan, W. Liu, R. Xu, and H. -k. Mao, Science (80-.). **344**, 877 (2014).

[7] W.L. Mao, Y. Meng, G. Shen, V.B. Prakapenka, A.J. Campbell, D.L. Heinz, J. Shu, R. Caracas, R.E. Cohen, Y. Fei, R.J. Hemley, and H. -k. Mao, Proc. Natl. Acad. Sci. **102**, 9751 (2005).

[8] R. Boehler, H.G. Musshoff, R. Ditz, G. Aquilanti, and A. Trapananti, Rev. Sci. Instrum. **80**, 045103 (2009).

[9] M. Mezouar, N. Rambert, G. Fiquet, D. Andrault, B. Sitaud, P. Loubeyre, S. Bauchau, W. Crichton, R. Boehler, E. Schultz, and G. Blattmann, High Press. Res. **25**, 71 (2007).

[10] G. Aquilanti, S. Pascarelli, O. Mathon, M. Muñoz, O. Narygina, and L. Dubrovinsky, J. Synchrotron Radiat. **16**, 376 (2009).

[11] C. Marini, I. Kantor, O. Mathon, and S. Pascarelli, High Press. Res. **33**, 108 (2013).

[12] J.-F. Lin, Geophys. Res. Lett. **31**, L14611 (2004).

[13] I. Kupenko, L. Dubrovinsky, N. Dubrovinskaia, C. McCammon, K. Glazyrin, E. Bykova, T.B. Ballaran, R. Sinmyo, A.I. Chumakov, V. Potapkin, A. Kantor, R. Rüffer, M. Hanfland, W. Crichton, and M. Merlini, Rev. Sci. Instrum. **83**, 124501 (2012).

[14] L. Dubrovinsky, K. Glazyrin, C. McCammon, O. Narygina, E. Greenberg, S. Übelhack, A.I. Chumakov, S. Pascarelli, V. Prakapenka, J. Bock, and N. Dubrovinskaia, J. Synchrotron Radiat. **16**, 737 (2009).

[15] T. Gu, X. Wu, S. Qin, and L. Dubrovinsky, Phys. Earth Planet. Inter. **184**, 154 (2011).

[16] O. Narygina, L.S. Dubrovinsky, H. Samuel, C.A. McCammon, I.Y. Kantor, K. Glazyrin, S. Pascarelli, G. Aquilanti, and V.B. Prakapenka, Phys. Earth Planet. Inter. **185**, 107 (2011).

[17] G. Aprilis, C. Strohm, I. Kupenko, S. Linhardt, A. Laskin, D.M. Vasiukov, V. Cerantola, E.G. Koemets, C. McCammon, A. Kurnosov, A.I. Chumakov, R. Rüffer, N. Dubrovinskaia, and L. Dubrovinsky, Rev. Sci. Instrum. **88**, 084501 (2017).

[18] Series of Lenses combining functions of Focusing the Laser Heating beam and spectroradiometric temperature measurements. http://pishaper.com/geoheat.htm (Accessed 1 January 2019)

[19] B.D. Adams and A. Chen, Mater. Today **14**, 282 (2011).

[20] F.D. Manchester, A. San-Martin, and J.M. Pitre, J. Phase Equilibria **15**, 62 (1994).

[21] T. Skośkiewicz, M. Horobiowski, and E. Trojnar, J. Less Common Met. **101**, 311 (1984).

[22] T. Skoskiewicz, Phys. Status Solidi **11**, K123 (1972).

[23] H.M. Syed, T.J. Gould, C.J. Webb, and E.M. Gray, (2016).

[24] K. Brownsberger, M. Ahart, M. Somayazulu, C. Park, S.A. Gramsch, and R.J. Hemley, J. Phys. Chem. C **121**, 27327 (2017).

[25] C.-S. Zha, K. Mibe, W.A. Bassett, O. Tschauner, H.-K. Mao, and R.J. Hemley, J. Appl. Phys. **103**, 054908 (2008).

[26] M. Santoro, J.F. Lin, V. Struzhkin, H.K. Mao, and R.J. Hemley, *Advances in High-Pressure Technology for Geophysical Applications* (Elsevier, 2005).

[27] L. Yang, Chinese Phys. B **25**, 076201 (2016).

[28] G. Shen and H.K. Mao, Reports Prog. Phys. **80**, 016101 (2017).

[29] J. Ruiz-Fuertes, A. Karandikar, R. Boehler, and D. Errandonea, Phys. Earth Planet. Inter. **181**, 69 (2010).

[30] L. Yang, A. Karandikar, and R. Boehler, Rev. Sci. Instrum. **83**, 063905 (2012).

[31] S. Anzellini, A. Dewaele, M. Mezouar, P. Loubeyre, and G. Morard, Science (80-.). **340**, 464 (2013).

[32] A. Salamat, R.A. Fischer, R. Briggs, M.I. McMahon, and S. Petitgirard, Coord. Chem. Rev. **277**–**278**, 15 (2014).

[33] D. Errandonea, B. Schwager, R. Ditz, C. Gessmann, R. Boehler, and M. Ross, Phys.

Rev. B **63**, 132104 (2001).

[34]Philos. Trans. R. Soc. London. Ser. A Math. Phys. Eng. Sci. **354**, 1279 (1996).

[35] R. Salem, S. Matityahu, A. Melchior, M. Nikolaevsky, O. Noked, and E. Sterer, Rev. Sci. Instrum. **86**, 093907 (2015).

[36] G. Aprilis, I. Kantor, I. Kupenko, V. Cerantola, A. Pakhomova, I.E. Collings, R. Torchio, T. Fedotenko, S. Chariton, M. Bykov, E. Bykova, E. Koemets, D.M. Vasiukov, C. McCammon, L. Dubrovinsky, and N. Dubrovinskaia, J. Appl. Phys. **125**, 095901 (2019).

[37] G. Morard, D. Andrault, D. Antonangeli, Y. Nakajima, A.L. Auzende, E. Boulard, S. Cervera, A. Clark, O.T. Lord, J. Siebert, V. Svitlyk, G. Garbarino, and M. Mezouar, Earth Planet. Sci. Lett. **473**, 94 (2017).

[38] N. Dubrovinskaia, L. Dubrovinsky, N.A. Solopova, A. Abakumov, S. Turner, M. Hanfland, E. Bykova, M. Bykov, C. Prescher, V.B. Prakapenka, S. Petitgirard, I. Chuvashova, B. Gasharova, Y.-L. Mathis, P. Ershov, I. Snigireva, and A. Snigirev, Sci. Adv. **2**, e1600341 (2016).

[39] A. Snigirev, P. Ershov, I. Snigireva, M. Hanfland, N. Dubrovinskaia, and L. Dubrovinsky, Microsc. Microanal. **24**, 238 (2018).

[40] A. Snigirev, V. Kohn, I. Snigireva, and B. Lengeler, Nature **384**, 49 (1996).

[41] G.B.M. Vaughan, J.P. Wright, A. Bytchkov, M. Rossat, H. Gleyzolle, I. Snigireva, and A. Snigirev, J. Synchrotron Radiat. **18**, 125 (2011).

[42] A. Snigirev, I. Snigireva, G. Vaughan, J. Wright, M. Rossat, A. Bytchkov, and C. Curfs, J. Phys. Conf. Ser. **186**, 012073 (2009).

[43] A. Narikovich, M. Polikarpov, A. Barannikov, N. Klimova, A. Lushnikov, I. Lyatun, G. Bourenkov, D. Zverev, I. Panormov, A. Sinitsyn, I. Snigireva, and A. Snigirev, J. Synchrotron Radiat. **26**, (2019).

[44] A. Bosak, I. Snigireva, K.S. Napolskii, and A. Snigirev, Adv. Mater. **22**, 3256 (2010).

[45] J.-M. Meijer, D. V. Byelov, L. Rossi, A. Snigirev, I. Snigireva, A.P. Philipse, and A. V.

Petukhov, Soft Matter **9**, 10729 (2013).

[46] I. Snigireva, K.V. Falch, D. Casari, M. Di Michiel, C. Detlefs, R. Mathiesen, and A. Snigirev, Microsc. Microanal. **24**, 552 (2018).

[47] A. Kavner and R. Jeanloz, J. Appl. Phys. **83**, 7553 (1998).

Section 5.B.

Isothermal Equation of State of Crystalline and Glassy Materials from Optical Measurements in Diamond Anvil Cells

T. Fedotenko[1,*], D.S. Souza[2], S. Khandarkhaeva[1], L. Dubrovinsky[2] and N. Dubrovinskaia[1, 3]

[1]*Material Physics and Technology at Extreme Conditions, Laboratory of Crystallography, University of Bayreuth, D-95440 Bayreuth, Germany*

[2]*Bayerisches Geoinstitut Universität Bayreuth, D-95440 Bayreuth, Germany*

[3]*Department of Physics, Chemistry and Biology (IFM), Linköping University, SE-581 83, Linköping, Sweden*

Review of Scientific Instruments 92, 063907 (2021), June 2021
DOI: 10.1063/5.0050190

Abstract:

Here we present a method to study the equation of state of opaque amorphous and crystalline materials in diamond anvil cells. The approach is based on measurements of sample dimensions using high-resolution optical microscopy. Data on the volumetric strain as a function of pressure allow deriving the isothermal equation of state of the studied material. The analysis of optical images is fully automatized and allows measuring the sample dimensions with a precision of about 60 nm. The methodology was validated by studying isothermal compression of ω-Ti up to 30 GPa in a Ne pressure transmitting medium. Within the accuracy of the measurements, the bulk modulus of ω-Ti determined using optical microscopy was similar to that obtained from X-ray diffraction. For glassy carbon compressed to ~30 GPa the previously unknown bulk modulus was found to be equal to K_0= 28.6 (8) GPa (K´= 5.5(2)).

* Corresponding author, email: TimofeyFedotenko@gmail.com

1. Introduction

Elastic properties of materials define the structural and electronic response of the system to applied stress that strongly depends on the nature of interatomic interactions. This makes knowledge of the elastic properties of materials as a function of pressure and temperature indispensable in materials science. The equation of state (EOS) of a system defines the relationship between the thermodynamic variables, such as volume (V), pressure (P), and temperature (T), through the bulk modulus and the thermal expansion coefficients. At a constant temperature, pressure-volume relations of a solid can be described by different types of analytical EOSes[1,2], involving the isothermal bulk modulus ($K = -V \cdot \left(\frac{\partial P}{\partial V}\right)$) and its pressure derivatives ($K' = \partial K/\partial P$).

Investigations materials' EOSes under pressure require subjecting them to extreme conditions. The first studies of condensed matter under static compression in the gigapascal pressure range were done many decades ago[3,4] in large volume presses. The invention and technical development of the diamond anvil cell (DAC) technique significantly enlarged accessible thermodynamic space in high-pressure studies, and the DAC technique has evolved in the powerful and routine experimental method at in-house laboratories and synchrotron beamlines[5]. X-ray diffraction (XRD) in DACs[6] is the most common technique for deriving EOSes of crystalline materials through measuring the unit cell volume of a sample as a function of pressure, but it is not applicable to amorphous and glassy materials because of their topological and chemical disorder[7]. This explains why EOSes of crystalline materials have been well studied, but so far little is known about P-V relations for non-crystalline matter (melts, metallic glasses, and other amorphous solids and nanocrystalline ceramics). These materials are currently in the focus of solid-state physics, chemistry, materials science, and geophysics research communities. In geosciences, glasses are considered as proxies of silicate melts whose properties are of great importance, as they control magmatic and volcanic activity and play therefore a central role in determining the chemical and physical evolution of the Earth throughout geologic time[8,9]. Studies of the compressional behavior, local structures, and densification mechanisms of silicate glasses at deep mantle conditions can shed light on the dynamics of the Earth's interior, which is still insufficiently undersood[10].

Elastic properties of both crystalline and amorphous materials can be studied *in situ* in DACs by utilizing such methods as X-ray absorption[11], Brillouin scattering (BS)[12], ultrasonic measurements (US)[6,13], impulsive stimulated scattering (ISS)[14], inelastic X-ray scattering (IXS)[15]**,** or by determining strain-stress relations using optical miscroscopy[16,17]. The sample density (and hence the EOS) can be obtained from high-pressure X-ray absorption measurements[18,19], but this method is hard to apply in DACs and it works reasonably well only for materials containing heavy elements (i.e. good X-ray absorbers).

Determination of the strain-stress relations using optical miscroscopy[16,17] requires measurements of the dimensions of an object being observed under the high-resolution optical microscope. According to Abbe's theory, the resolution limit of the optical system (assuming the absence of aberrations) is comparable with the size of the Airy disk[17]. However, it is possible to achieve a much higher resolution by taking into account the spatial distribution of the intensity in the Airy disk itself[20]. The technique for study EOS through the sample length determination in DAC using image shearing device[21] was firstly presented by Scott and Jeanloz in 1984[17], who reported the precision of measurements of about 0.065 μm (for the samples with the linear size of around 100 μm) and validated the technique through determining the EOS of Au[17]**.** The isothermal bulk modulus ($K_0 = 156(35)$ GPa) determined from the optical length measurements was found to be comparable with that known from high-precision XRD studies ($K_0 = 167(5)$ GPa)[22], and the high uncertainty was attributed to the limited pressure range of the investigations and small sizes of the samples used[17]. Deriving the EOS of GeO_2 glass up to 12 GPa through the optical measurements was reported by Smith et al in 1995[23]. In this work, the spacing between the lines deposited on the polished surface of the GeO_2 sample was determined using a magnified image and the precision was reported to be about 0.5 μm for the maximum line spacing of 100 μm. Such precision is significantly worse than the one reported by Scott and Jeanloz[17], but still reasonable for highly compressible glass samples[23]. One of the major problems of the approaches described above is the high uncertainty in the obtained sample dimensions: the observed sample length is strongly affected by the focus position of the sample and the definition of the length relies on the subjective perception of the operator. In order to make the method reliable and accurate,

the measurements have to be performed at the same focus position in each pressure point. Defining the focus point by eye is inaccurate.

In 2012, Amin et al.[16] described a partially automatized algorithm for determination of EOSes through high-resolution optical microscopy. The methodology relied on two-dimensional image acquisition and its subsequent analysis in order to quantify changes in the sample surface area. The authors applied the Canny edge detection algorithm[24] to define the sample boundaries and calculate its surface area. However, Amin et al.[16] yielded higher experimental uncertainties if compared to the method of Scott and Jeanloz[17]. The lower precision of the partially automatized measurements of Amin et al.[16] could be explained by the problem with a subjective choice of the focus point or/and with applying Gaussian smoothing during the image processing with the Canny algorithm. Amin et al.[16] chose samples of random shapes but applied a smoothing algorithms, which blur out the corners and junctions, thus making it harder to detect their actual positions. Still, despite all obstacles, the method by Amin et al.[16] performed reasonably well on several crystalline and amorphous compounds at pressures up to 12 GPa.

Here, we describe the methodology of the EOS determination based on optical studies of materials in DACs at pressures up to 30 GPa. The data analysis is fully automatized (i.e. the effect of the operator is negligible) and applicable to opaque crystalline and amorphous/glassy materials. Our methodology exploits high-resolution optical microscopy in DACs, image analysis, and statistical data treatment. A significant advantage of our approach is that experiments do not require access to synchrotron facilities or specialized X-ray sources. At the same time, our method can be easily applied in combination with X-ray imaging and diffraction.

2. Experimental details

2.1. Instrumental setup overview

In our experiments, we use the customized optical system based on the previously developed laser heating setup[25]. It is schematically shown in **FIG 1**.

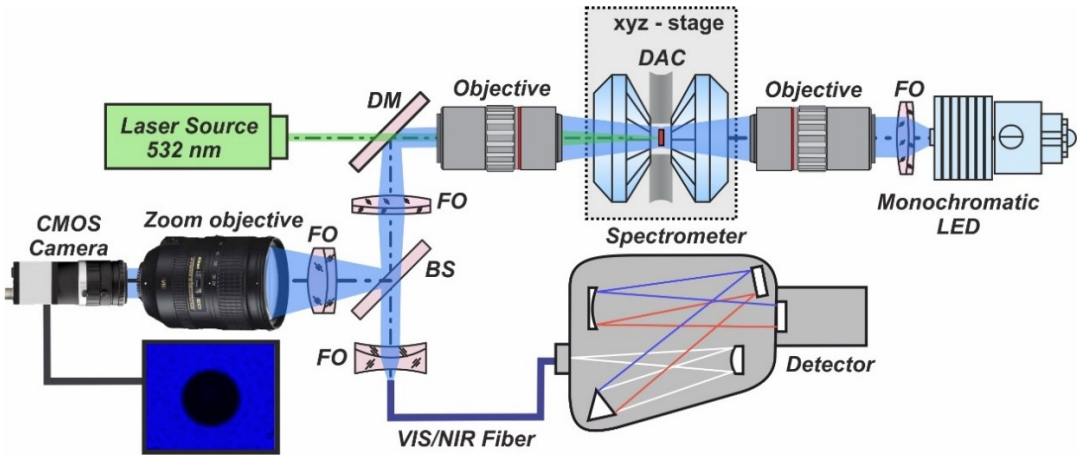

FIG. 1. Schematic diagram of the optical system. DM is the long-pass dichroic mirror (Thorlabs DMLP505); FOs are the focusing optics (1 – Edmund optics #49-366-INK; 2 - Edmund optics #49-323-INK; 3 - Edmund optics #45-220); BS is the 50/50 beam splitter (Thorlabs DMLP505); CMOS is the camera for image observation.

The image of the sample is formed by transmitted light passing through a DAC sample chamber and collected from the opposite side by a long working distance objective (Mitutoyo NIR infinity-corrected M Plan Apo NIR B 20x). To avoid chromatic aberrations, the sample is illuminated by the monochromatic LED (Thorlabs M455L2, λ = 455 nm). The light passes through a set of lenses into a zoom objective (Nikon AF-S NIKKOR 28-300mm f/3.5-5.6G ED VR Lens) and projects the sample image on the matrix of a high-resolution CMOS camera (EYE © CMOS cameras, UI-3280CP, resolution 2456 x 2054 pixels, sensor size ~ 8.4 x 7.0 mm, 12-bit depth). The setup provides variable magnification in the range of 80 to 320 times. At maximum magnification, the size of an image projected on the camera sensor from the sample of 25 μm is around 8 mm, while a single-pixel corresponds to approximately 0.22 μm.

The pressure during the experiment is controlled by ruby fluorescence[26] using a 532 nm green laser (Laser Quantum, Inc. model gem 532) and an IsoPlane SCT 320 spectrometer equipped with a 1024x256 PI-MAX 4 camera (Princeton Instruments, Inc.).

2.2. DAC and sample preparation

In our experiments, we utilize the BX90-type large aperture DACs equipped with Boehler-Almax type diamonds (culet diameters of 250 μm). For each DAC, the sample

chamber is formed by pre-indentation of a rhenium gasket to ~ 30-35 μm thickness and drilling a hole of 120 μm in diameter in the center of the indentation. Pressure is measured by ruby fluorescence, and Ne is used as a pressure transmitting medium.

The geometrical shape of a sample plays an important role in data acquisition and analysis. Simple and symmetrical shapes, such as balls or rectangular plates, allow more measurements of the sample length to be made at every pressure point that improves the statistics and reduces the random error upon data analysis (this will be discussed in detail below, in section 2.4).

In this study, metallic samples were prepared from titanium microspheres with a diameter of about ~ 25 μm (purchased from Cospheric Microspheres Inc.). The spheres were pressurized between two diamond anvils in a DAC to form a thin cylindrical plate with a thickness of about 5 μm. The obtained plates were given a square shape with an edge length of about 25-30 μm (**FIG. 2**) by milling using the FEI - QUANTA 3D Focused Ion Beam (FIB).

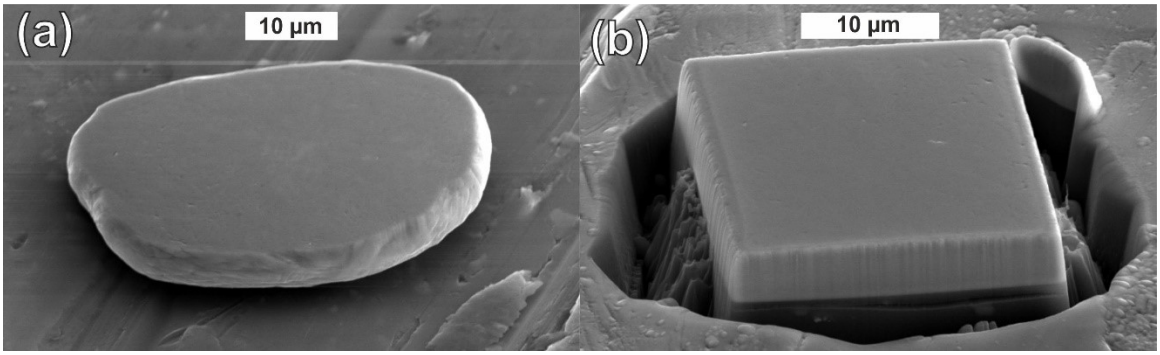

FIG. 2. SEM images of the Ti sample. (a) A flattened microsphere of the initial diameter of about 25 μm; (b) A square plate is shaped by FIB.

2.3. Data acquisition

Setup adjustment

Adjustment of the camera and the sample illumination is the key to obtaining high-quality images and, hence, reproducible and precise measurements. Such parameters as the intensity and the angle of incidence of light, settings of the CCD camera, and the sample position within the field of view must be maintained constant during the whole set

of measurements at different pressure points. To achieve stable illumination conditions during the whole experiment, the DAC was coupled with a membrane pressure controller and mounted on a 3-axis motorized stage. Then we manually adjusted the angle of incidence of light to achieve a flat field background in both horizontal and vertical planes on the entire image (**FIG. 3**)

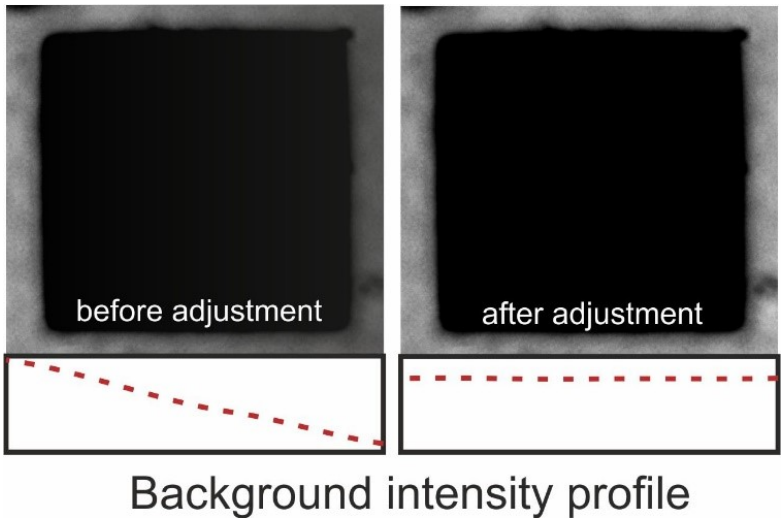

FIG.3. Images of the sample before and after adjustment of the angle of incidence of light. Diagrams under the images schematically represent the distribution of the background intensity in the horizontal direction.

Settings of the camera, which can affect the image representation (digital gain, automatic contrast/ brightness/ color adjustment, nonlinear LUT (Look-up table), white balance, black offset, infrared filter correction matrix) were disabled. At the last step, we adjusted the camera exposure time and the light intensity to use the complete dynamic range of the camera sensor.

Data acquisition

If the length of an object is measured under an optical microscope, the result depends on the focal position of the object. To avoid ambiguities, the measurements should be made on the images in focus. In order to choose the right image independent of the operator, we apply the focus-stacking technique by acquiring a set of optical images at different focal positions. At each pressure point, the images are collected upon

continuous movement of the DAC along the optical axis of the system. First, the best focal position is determined by the eye on the sharpness of the image. Then the DAC is moved in the range of about ±20 μm with a speed of ~2 μm/s, and a series of sample images is taken with ~100 ms exposure time (**FIG.4**). Typically, the total number of images for each pressure point is up to 200. Although a single set data collection for one pressure point takes less than a minute, the stabilization of pressure upon the relaxation of the metallic membrane requires ~5-10 min, and the total duration of an experiment with typically ~20 pressure points takes approximately 6 hours. The algorithm for selecting the sharpest images is described in the next section.

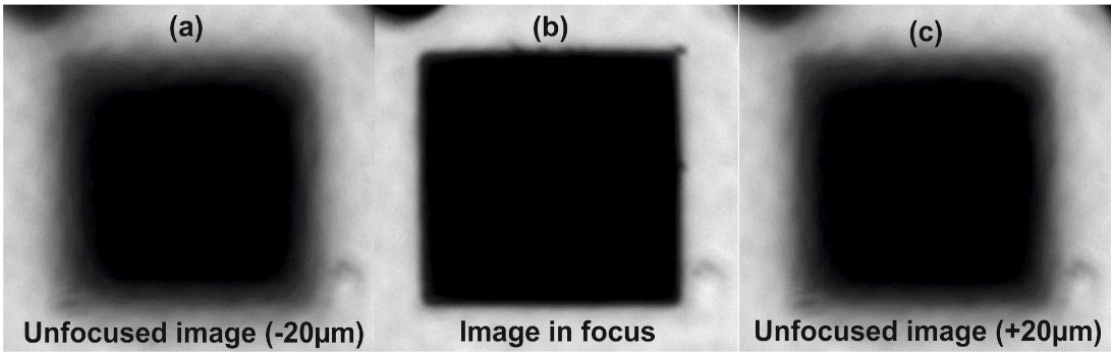

FIG. 4. Illustration of focus stacking on the example of images of a titanium plate at 4 GPa. (a) The image was taken at -20 μm from the approximate in-focus position; (b) near the in-focus position as first determined by eye; (c) at + 20 μm from the approximate in-focus position.

2.4. Data analysis

A fully automatic procedure (employing a custom Python script) has been developed for extracting the length of the sample from an acquired set of images at each pressure point. The procedure includes the analysis of image intensity profiles at the edges of the sample that results in unambiguous selections of in-focus images, whose intensity profiles are used for determining the exact positions of the sample edges (**FIG. 5**). This enables to precisely measure the sample length at a given pressure point.

Image intensity profile analysis

A digital image can be represented as a two-dimensional matrix of values of light intensities, where each element of the matrix corresponds to a pixel on the camera sensor. Considering rows or columns of that matrix, one can make the image cross-section intensity profiles (**FIG. 5**). The dotted line in **FIG. 5a** is the cross section line in the image of the square-shaped titanium plate. The intensity profile in **FIG. 5b** shows the intensity values taken from regularly spaced points along the line path in the image.

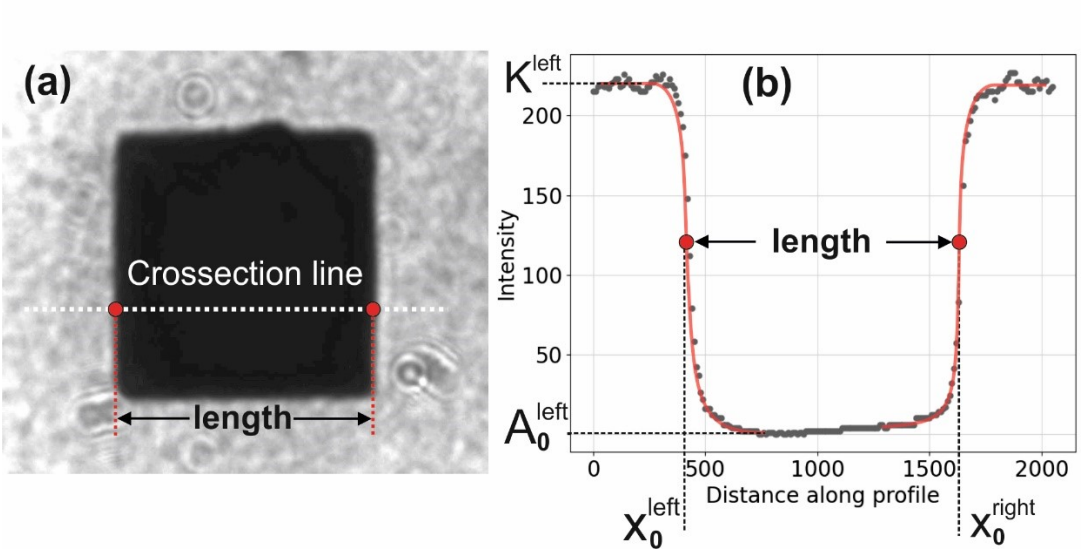

FIG. 5. Image intensity profile for defining the edges of the sample. (a) Sample image with the cross section line. The enlarged red dots mark the position of the sample edges, which define the sample length (in the horizontal direction); (b) image cross section intensity profile. Grey dots are the measured intensity profile; red curves are the fit of the left and right edges regions to the parametric sigmoid functions; enlarged red dots are left and right sigmoid's midpoints, which define the position of the sample edges.

To describe the shape of the edges of the intensity profile, we used a parametric sigmoid function:

$$S(x) = A_o + \frac{K - A_0}{1 + e^{-\alpha(x - x_0)}} \qquad Eq.(1)$$

(where x is the pixel coordinate, A_o is the lower asymptote, *K* is the upper asymptote, *α* is the growth rate (or steepness of the curve) and x_0 is the value of the sigmoid's midpoint). Thereby, we define the sample length in pixels as a difference between the two

sigmoid's midpoints taken along a single image cross section (at the right and left edges of the sample) ($x_0^{right} - x_0^{left}$). Such parametrization allows defining the positions of the edges with subpixel accuracy.

Selecting in-focus images

If an object is not in focus, its edges look blured. It is obvious that the sharper the image, the steeper the edges of the cross section intensity profile (**FIG. 6**).

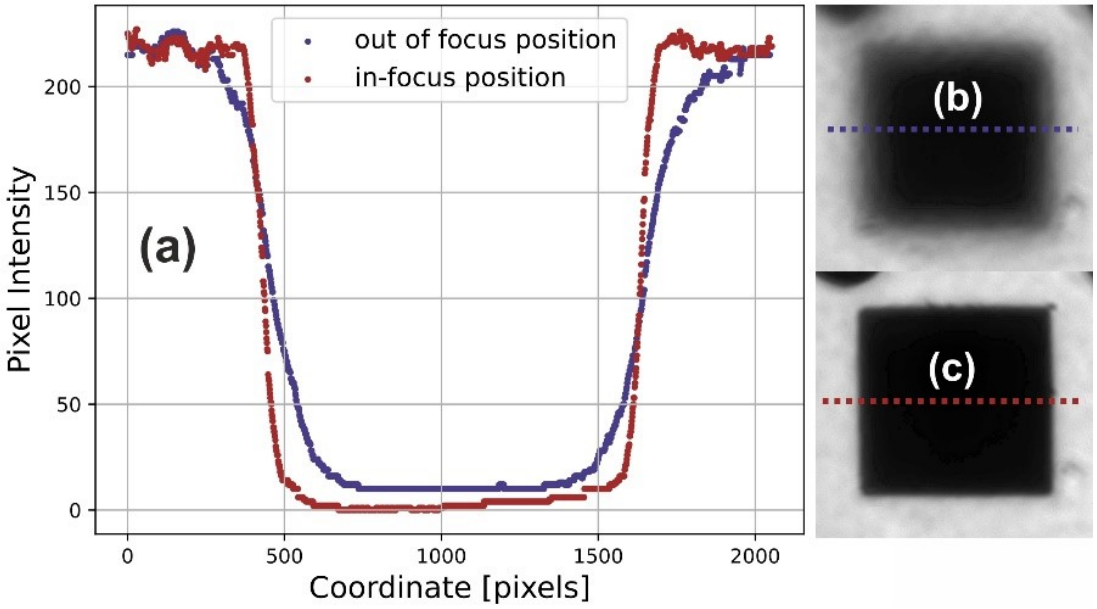

FIG. 6. The image cross section intensity profiles and microphotographs of the sample. (a) Profiles; (b) out of focus position; (c) in-focus position.

To select the in-focus images, we analyzed every image of the set and plotted the steepness parameter (i.e. the growth rate parameter α of the sigmoidal function, Eq. 1) *vs* the image number, which indicates the DAC position along the optical axis. An example of such a plot is shown in **FIG. 7**.

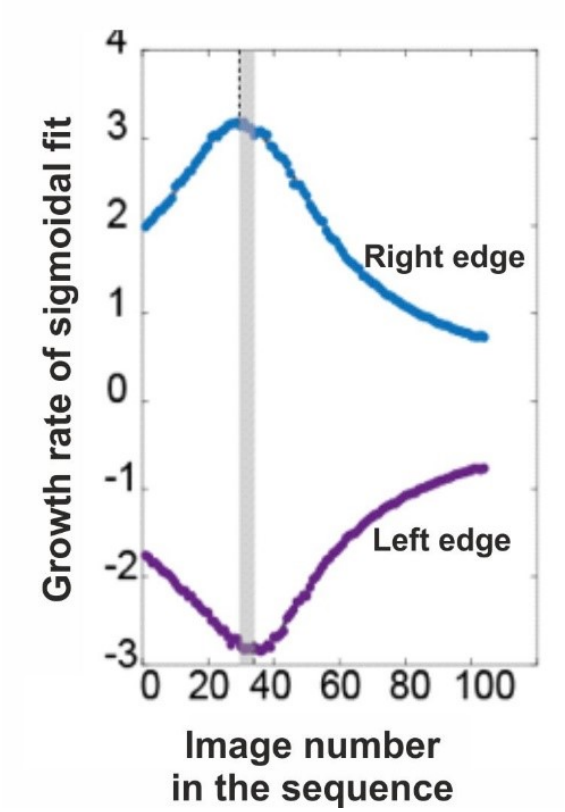

FIG. 7. Growth rate (parameter α of the sigmoidal function) *vs* the image number.

Since both vertical and horizontal cross-sections are used for in-focus images selection, the algorithm gives four, usually slightly different, focal positions. This can be attributed to slightly uneven illumination of different sample edges or minor inclination of the sample in the DAC. However, we found that for a set of 100 - 150 images (frames) the variations within up to 10 frames do not introduce measurable errors in the length of the sample (see error evaluations section below).

Sample length measurements

As said before, for each pressure point we collected a set of up to 200 images. Four in-focus images were selected as described above. In the case of rectangular shape samples for each of in-focus images, we made a cross section mesh of 50 to 100 lines with a line spacing of 5 to 20 pixels (**FIG. 8(a)**). For each line, the length of the sample was determined independently. All measurements for vertical and horizontal lines were

averaged independently, and the standard deviation we calculated for both vertical and horizontal dimensions.

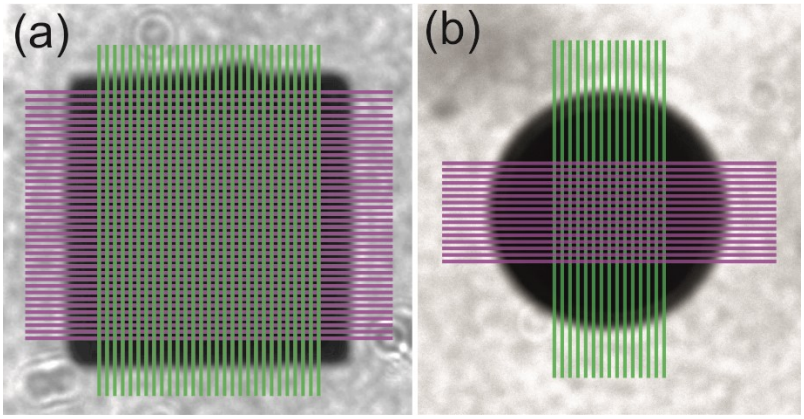

FIG. 8. Schematic of the cross section mesh for the length measurements. Green and purple lines represent image cross sections for rectangular (a) and spherical (b) shape samples. Length measurements are performed along each of vertical and horizontal cross sections. The mesh size depends on the sample size and geometry, with a typical value of 25 to 100 cross section lines per dimension with line spacing of 4 to 20 pixels.

For spherical shape samples, at each in-focus image cross section mesh was built around vertical and horizontal diameters (**FIG. 8(b)**). The length of the sample was determined as an average of the largest horizontal and vertical dimensions with error corresponds to the standard deviation.

Independently on shape, the final dimensions of the sample at each pressure point were the average values obtained for all four processed images (with the final random error being the outcome of error propagation for each individual image).

Data filtering and error evaluation

Filtering of the data is required in the presence of edge defects of the samples, which can induce significant errors in the selection of in-focus images and the measurements of the sample length. A bulb-like defect on the top edge of the square-plate sample is seen in **FIG. 9**. In such a case, we manually excluded the defect region

from further analysis and performed the focus position analysis along with length measurements only on defect-free regions of the sample (**FIG. 9**).

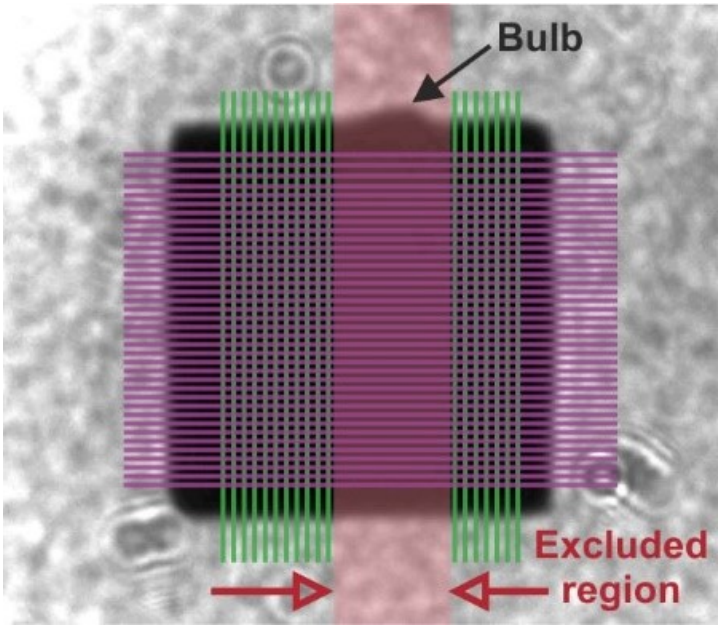

FIG. 9. Example of the data filtering. The black error indicates the bulb-like defect on the top edge of the square plate sample. Green and purple lines represent the filtered cross-section mesh and excluded defect region is shown as a pink shaded area.

FIG. 10 presents an example of the uncertainty in the length measurements of titanium square plate at different pressures. The average lengths of the sample, as measured at the first and the last pressure points, were 1217.2 and 1144.7 pixels, respectively. The maximum uncertainty in the sample length was less than three pixels that corresponds to the value of relative uncertainty of ~ 0.25% for the sample with the real size of 30 μm.

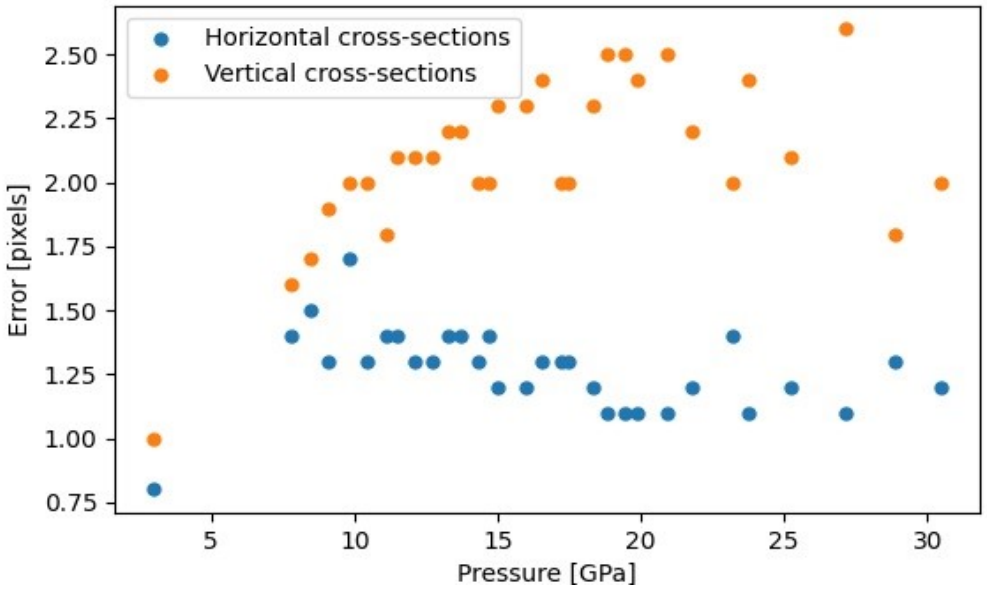

FIG. 10 Uncertainty in the length measurements at different pressures for the titanium square plate sample. Blue and yellow points correspond to the errors for length measurements in horizontal and vertical planes of the image. The average lengths of the sample at the first and the last pressure points were 1217.2 and 1144.7 pixels, respectively.

EOS determination

In this work, the determination of the sample volumetric strain is based on several assumptions: (1) sample conditions in DAC are quasi-hydrostatic; (2) the sample does not have voids in the bulk; (3) compression of the sample is isotropic. Then, the sample strain (f_e) can be described as Eulerian finite strain[27]:

$$f_e = \frac{1}{2}\left[\left(\frac{V_p}{V}\right)^{\frac{2}{3}} - 1\right] \qquad Eq.(2)$$

where V is the sample volume at a given pressure, and V_p is the sample volume at the reference pressure, and the following relationship is true:

$$\frac{V}{V_p} = \left(\frac{L}{L_p}\right)^3 \qquad Eq.(3)$$

where L is the average length at a given pressure, and L_p is the average length at the reference pressure. To determine the bulk modulus ($\boldsymbol{K_0}$) and it's derivative ($\boldsymbol{K'}$) the pressure–strain data, obtained by optical measurements, were fitted to the 3rd order Birch-Murnaghan EOS[28].

$$\mathbf{P} = 3\boldsymbol{K_0} \cdot f_e(1+2f_e)^{\frac{5}{2}} \cdot \left[1 + \frac{3}{2}(\boldsymbol{K'} - 4)f_e\right] \qquad Eq.(4)$$

3. Examples of application

EOS of ω-Titanium

To validate the technique described above, the EOS of a material obtained on the basis of optical microscopy measurements should be compared with the known EOS of the same material, previously determined using well-established methods. Titanium is a transition metal with the EOS well studied using X-ray diffraction[29], so we chose Ti as the reference material. It is known that Ti undergoes the α-to-ω structural phase transition[30] which takes place between 2 and 12 GPa at 300 K, depending on the pressurization conditions[30]. It results in a volume reduction of a few percent that provides a chance to test if the first order phase transition can be detected using optical microscopy.

The sample was prepared by flattening of a Ti microsphere (Cospheric Microspheres Inc.) and shaped using FIB to a square plate with the edge size of about 28 μm. After loading the DAC with Ne, the pressure was found to be ~8 GPa. The sample was then studied in the pressure range of 8 to 30 GPa (**FIG. 11**).

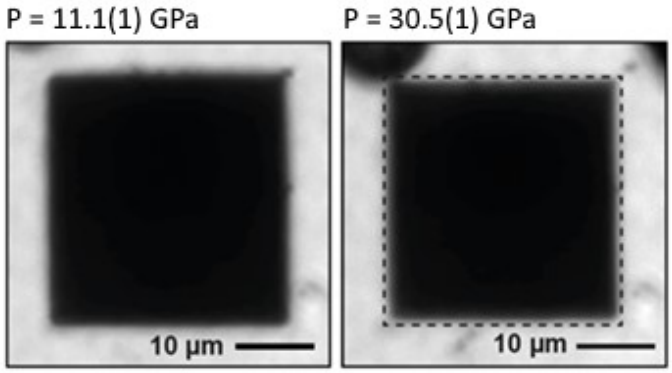

FIG. 11. Images of the Ti square plate at 11.1(1) and 30.5(1) GPa. The dashed line on the right image corresponds to the sample contour at 11.1(1) GPa.

The images were collected and processed as described above. The results of measurements, in form of the dependence of the relative volume on pressure, are shown in **FIG. 12**. Some irregularities in the compressional behavior of the sample were observed at around 11 GPa, which may be related to the *α*-to-*ω* Ti phase transition[29]. However, the effect is hardly visible (**FIG. 12, inset**), and further experiments are needed to establish how sensitive the optical microscopy may be to detect phase transitions.

The data collected above 11 GPa are related to *ω*–Ti. The sample was pressurized with a step of 1.5 - 2 GPa from 11.1(1) to 30.5(1) GPa that resulted in 24 data points (**FIG. 12**). At each pressure point, a set of 100 to 150 images was collected by focus stacking. Four in-focus images were selected. The difference in their focal positions did not exceed 2 μm. Determination of the length was performed on each of the four images by making 100 cross-section intensity profiles in the horizontal and vertical directions. Therefore 200 lengths measurements were made for each image, thus 800 measurements for four images in total. The standard deviation of the average length lays within 3 pixels that corresponds to approximately 60 nm.

Over the compression from 11.1(1) to 30.5(1) GPa, a decrease in the average sample length of 48 pixels (~1μm) was observed, while the sample volume contracted by about 10%. The pressure – relative volume data (**FIG. 12**) were fitted to the 3rd order BM EOS with the parameters $K_0 = 108\ (2.6)\ \mathrm{GPa}$ and $K_0' = 3.5(3)$, in good agreement with those obtained from XRD data of Dewaele et al. ($K_0 = 107(3)\ \mathrm{GPa}$, $K_0' = 3.55(3)$)[29].

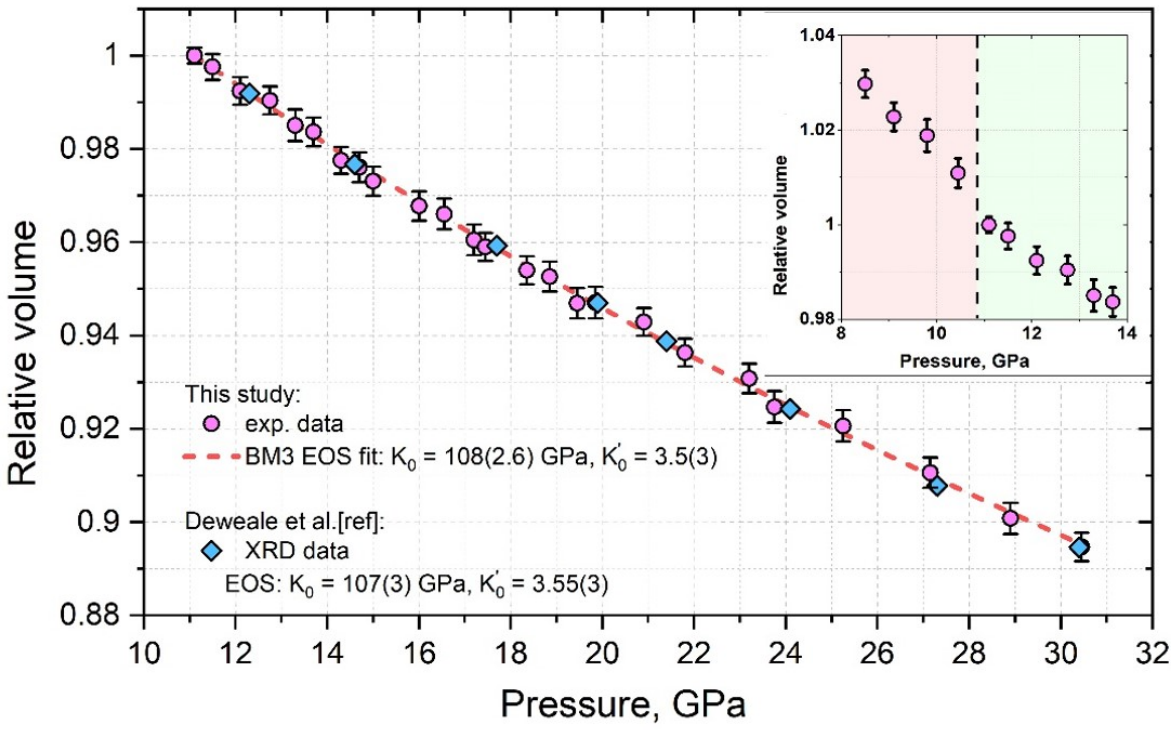

FIG. 12. The pressure dependence of the relative volume of ω-Ti. Our experimental points are shown by purple circles; the red dashed line is the fit of the experimental data to the 3rd order BM EOS with the following parameters $K_0 = 108\ (2.6)$ GPa, $K' = 3.5(3)$. Blue diamonds are the experimental data from Dewaele et al[30] obtained by XRD measurements. The inset shows the P region between 8 and 14 GPa. Different colors indicate the fields of *α*-Ti (pink) and *ω*-Ti (green).

EOS of glassy carbon

Here, two glassy carbon spheres (microspheres type-I, purchased from Alpha Aesar Inc.) with the initial diameters of about 12 - 14 μm were loaded into the sample chamber (FIG. 13) and pressurized in a Ne pressure transmitting medium up to 30 GPa.

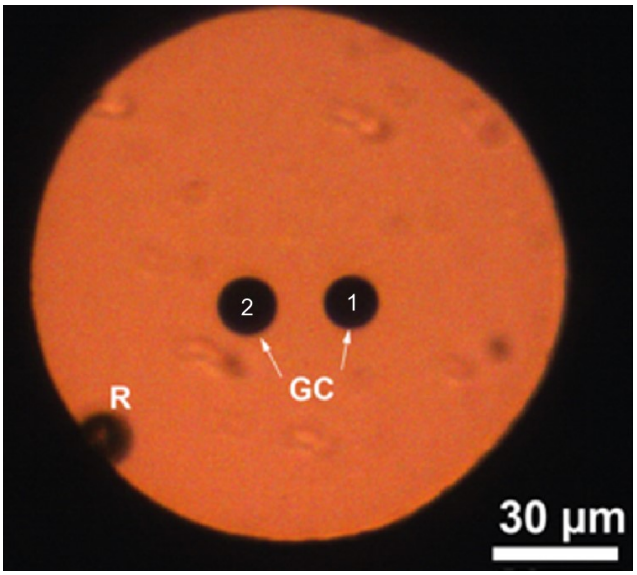

FIG. 13. Microphotograph of DAC sample chamber with GC samples at ambient pressure (before Ne loading). The GC-1 and GC-2 are glassy carbon spheres with diameters of around 12 - 14 μm; R is the ruby pressure marker.

Starting pressure (after Ne loading) was 6.9 (1) GPa. The sample volume at this pressure was chosen as the reference for further strain calculations. Like in the experiment with Ti, we performed the length measurements at each pressure step with an interval of 1.5 – 2 GPa (18 data points in total). A set of 100 to 150 images was obtained by the focus stacking at each pressure point, and four in-focus images were selected. The sample in-focus positions were found within the range of 2 μm.

For GC-1 sphere (the smaller one), we observed a decrease in the average sample size (the diameter of the sphere) of ~81 pixels (~1.1 μm) with a volume contraction of about 20% upon compression from 6.9 to 30 GPa (FIG. 14). Similar compressional behavior was observed for GC-2 sphere (the larger one) up to 23 GPa (FIG. 14), but beyond its volume stayed unchanged within the error of size measurements. Considering the larger initial diameter of the GC-2 sphere, it might be a result of its bridging between the diamond anvils, therefore we excluded the corresponding data points from the further analysis. The fit of the experimental data to the 3rd order BM EOS gave the following parameters: $K_0 = 28(2)$ GPa, $K' = 5.5(5)$ (FIG. 14). As expected, the compressibility of glassy carbon appeared to be relatively high. According to the obtained EOS, the total volume contraction (relative to the ambient pressure) was of about 31%. Thus, the

compressional behavior of glassy carbon was found to be very smooth, in agreement with the previous studies based on on Raman spectroscopy[35], which gave no evidence of a significant change in the type of chemical bonding in GC up to 60 GPa.

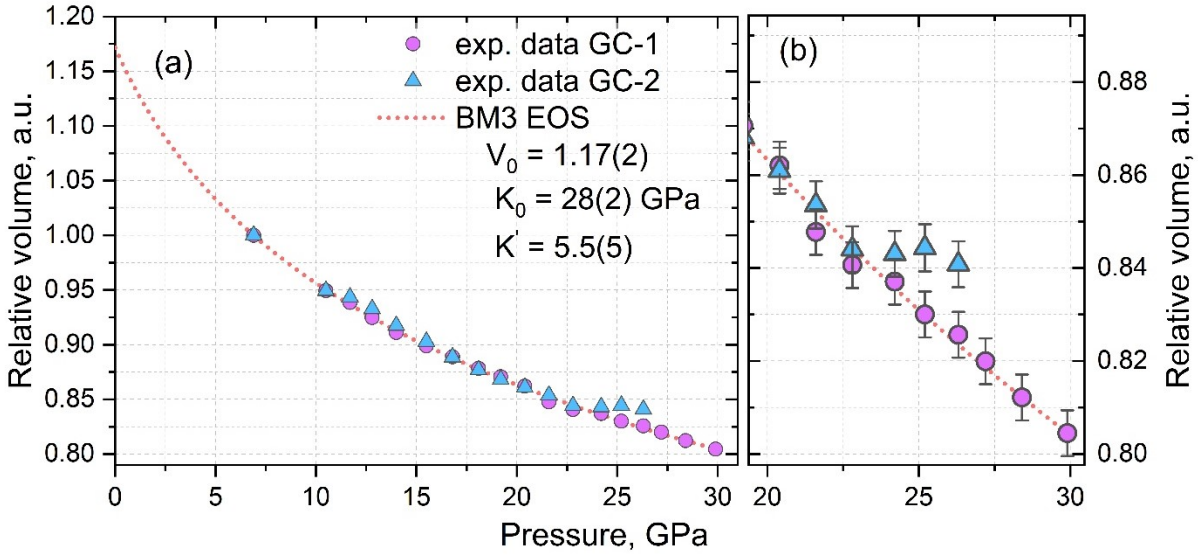

FIG. 14. The EOS of glassy carbon. (a) Experimental P-V data obtained for two GC spheres, GC-1 (purple circles) and GC-2 (blue triangles); the red dashed line is the fit of the experimental data to the 3rd order BM EOS with the following parameters: $K_0 = 28(2)$ GPa, $K' = 5.5(5)$. (b) Enlarged view for the pressure region between 20 and 30 GPa.

4. Conclusion

In this work, we have developed the technique to determine the EOS of opaque crystalline and amorphous solids using high-resolution optical microscopy in DACs. Our methodology is based on acquiring sample images at variable pressure and determining changes in the sample linear dimensions upon compression with a very high precision down to 60 nm. The analysis of images is automatized that grants the results to be independent of the operator.

The method was validated by studies of the EOS of ω-Ti up to 30 GPa. Our results agree well with the literature data obtained for ω-Ti on the basis of synchrotron XRD[29]. The EOS of glassy carbon reported in this work was determined for the first time.

The significant advantage of the presented method is that experiments do not require access to synchrotron facilities or specialized X-ray sources (but it can be easily coupled with X-ray imaging and diffraction). We are convinced that our work opens the way for wide investigations of opaque glasses, amorphous alloys, and crystalline materials at high pressures.

5. Acknowledgments

N.D. and L.D. thank the Federal Ministry of Education and Research, Germany (BMBF, grant No. 05K19WC1) and the Deutsche Forschungsgemeinschaft (DFG projects DU 954-11/1, DU 393-9/2, and DU 393-13/1) for financial support. N.D. thanks the Swedish Government Strategic Research Area in Materials Science on Functional Materials at Linköping University (Faculty Grant SFO-Mat-LiU No. 2009 00971).

6. Data Availability

The data that support the findings of this study are available from the corresponding author upon reasonable request.

7. References

[1] P. Vinet, J. Ferrante, J.H. Rose, and J.R. Smith, J. Geophys. Res. **92**, 9319 (1987).

[2] F. Birch, Phys. Rev. **71**, 809 (1947).

[3] F.D. Murnaghan, Proc. Natl. Acad. Sci. **30**, 244 (1944).

[4] P.W. Bridgman, Phys. Rev. **60**, 351 (1941).

[5] W.A. Bassett, High Press. Res. **29**, 163 (2009).

[6] S.D. Jacobsen, J. Geophys. Res. **107**, 2037 (2002).

[7] F. Yonezawa and T. Ninomiya, *Topological Disorder in Condensed Matter* (Springer Berlin Heidelberg, Berlin, Heidelberg, 1983).

[8] I. Kushiro, J. Geophys. Res. **81**, 6347 (1976).

[9] B.O. Mysen and D. Virgo, in *Adv. Mineral.* (Springer Berlin Heidelberg, Berlin,

Heidelberg, 1994), pp. 238–254.

[10] S.K. Lee, Y. Fei, G.D. Cody, and B.O. Mysen, in *Adv. High-Pressure Technol. Geophys. Appl.* (Elsevier, 2005), pp. 241–261.

[11] S. Petitgirard, G. Spiekermann, K. Glazyrin, J. Garrevoet, and M. Murakami, Phys. Rev. B **100**, 214104 (2019).

[12] Y.-H. Ko, M. Ahart, J.-H. Ko, and J. Song, J. Korean Phys. Soc. **70**, 382 (2017).

[13] S.D. Jacobsen, H. Spetzler, H.J. Reichmann, and J.R. Smyth, Proc. Natl. Acad. Sci. **101**, 5867 (2004).

[14] J.M. Brown, L.J. Slutsky, K.A. Nelson, and L.-T. Cheng, J. Geophys. Res. **94**, 9485 (1989).

[15] G. Fiquet, J. Badro, F. Guyot, C. Bellin, M. Krisch, D. Antonangeli, H. Requardt, A. Mermet, D. Farber, C. Aracne-Ruddle, and J. Zhang, Phys. Earth Planet. Inter. **143**–**144**, 5 (2004).

[16] S.A. Amin, E.N. Rissi, K. McKiernan, and J.L. Yarger, Rev. Sci. Instrum. **83**, 033702 (2012).

[17] C. Scott and R. Jeanloz, Rev. Sci. Instrum. **55**, 558 (1984).

[18] Y. Katayama, K. Tsuji, H. Kanda, H. Nosaka, K. Yaoita, T. Kikegawa, and O. Shimomura, J. Non. Cryst. Solids **205**–**207**, 451 (1996).

[19] Y. Katayama, K. Tsuji, O. Shimomura, T. Kikegawa, M. Mezouar, D. Martinez-Garcia, J.M. Besson, D. Häusermann, and M. Hanfland, J. Synchrotron Radiat. **5**, 1023 (1998).

[20] W.M. BULLIS and D. NYYSSONEN, in (1982), pp. 301–346.

[21] J. Dyson, J. Opt. Soc. Am. **50**, 754 (1960).

[22] D.L. Heinz and R. Jeanloz, J. Appl. Phys. **55**, 885 (1984).

[23] K.H. Smith, E. Shero, A. Chizmeshya, and G.H. Wolf, J. Chem. Phys. **102**, 6851 (1995).

[24] J. Canny, IEEE Trans. Pattern Anal. Mach. Intell. **PAMI-8**, 679 (1986).

[25] T. Fedotenko, L. Dubrovinsky, G. Aprilis, E. Koemets, A. Snigirev, I. Snigireva, A. Barannikov, P. Ershov, F. Cova, M. Hanfland, and N. Dubrovinskaia, Rev. Sci. Instrum. **90**, 104501 (2019).

[26] G. Shen, Y. Wang, A. Dewaele, C. Wu, D.E. Fratanduono, J. Eggert, S. Klotz, K.F. Dziubek, P. Loubeyre, O. V. Fat'yanov, P.D. Asimow, T. Mashimo, and R.M.M. Wentzcovitch, High Press. Res. **40**, 299 (2020).

[27] T. Katsura and Y. Tange, Minerals **9**, 745 (2019).

[28] O.L. Anderson, *Equations of State of Solids for Geophysics and Ceramic Science* (Oxford University Press, New Yourk, 1995).

[29] A. Dewaele, V. Stutzmann, J. Bouchet, F. Bottin, F. Occelli, and M. Mezouar, Phys. Rev. B **91**, 134108 (2015).

[30] D. Errandonea, Y. Meng, M. Somayazulu, and D. Häusermann, Phys. B Condens. Matter **355**, 116 (2005).

[31] P.J.F. Harris †, Philos. Mag. **84**, 3159 (2004).

[32] R.E. FRANKLIN, Nature **177**, 239 (1956).

[33] P.J.F. Harris and S.C. Tsang, Philos. Mag. A **76**, 667 (1997).

[34] G.M. Jenkins and K. Kawamura, J. Mol. Struct. **36**, 172 (1977).

[35] N.A. Solopova, N. Dubrovinskaia, and L. Dubrovinsky, Appl. Phys. Lett. **102**, 121909 (2013).

Section 5.C.

Synthesis of palladium carbides and palladium hydride in laser heated diamond anvil cells

T. Fedotenko[1*], L. Dubrovinsky[2], S. Khandarkhaeva[2], S. Chariton[2], E. Koemets[2], I. Koemets[2], M. Hanfland[3] and N. Dubrovinskaia[1, 4]

[1]*Material Physics and Technology at Extreme Conditions, Laboratory of Crystallography, University of Bayreuth, D-95440 Bayreuth, Germany*

[2]*Bayerisches Geoinstitut Universität Bayreuth, D-95440 Bayreuth, Germany*

[3]*European Synchrotron Radiation Facility, F-38043 Grenoble, France*

[4]*Theoretical Physics Division, Department of Physics, Chemistry and Biology (IFM), Linköping University, SE-581 83, Linköping, Sweden*

Journal of Alloys and Compounds 844:156179, June 2020
DOI:10.1016/j.jallcom.2020.156179

Abstract:

The diamond anvil cell (DAC) technique is a powerful method for the synthesis and studying of novel materials at extreme conditions. In this work, we report on high-pressure high-temperature (HPHT) synthesis of palladium carbides (PdC_x) and palladium hydride (PdH) in a laser heated diamond anvil cell. Formation of PdC_x phases with a face-centered cubic (fcc) structure resulted from a chemical reaction of Pd with carbon from the diamond anvils at a pressure of about 50 GPa and temperature of 2500-3000 K. The samples were analyzed *in situ* using synchrotron X-ray diffraction. The compressional behavior of the two phases, $PdC_{0.19}$ and $PdC_{0.21}$, was studied on decompression. The fit of the pressure-volume data using the 3rd order Birch-Murnaghan equation of state gave the following parameters: V_0 = 65.1(1) Å^3, K_0 = 241(9) GPa and K_0' = 2.1(3) for $PdC_{0.21}$, and V_0 = 64.51(5) Å^3, K_0 = 189(8) GPa and K_0' = 4.5(4) for $PdC_{0.19}$. The palladium hydride PdH was synthesized at P= 39(2) GPa and T= 1500(200) K through a direct reaction of Pd with paraffin oil.

* Corresponding author, email: TimofeyFedotenko@gmail.com

1. Introduction

Palladium is a transition metal known for its exceptional ability to absorb hydrogen in a bulk [1,2]. The palladium hydride was found to exhibit superconducting properties (T_c = 8-10 K) [3,4] that stimulated intensive studying of the Pd-H and Pd-D systems at extreme conditions [5]. As palladium is one of the preferred catalysts for hydrogenation of hydrocarbons in the petrochemical industry [6–9], studies of its possible hydrides and carbides are also of technological importance: their formation in palladium nanoparticles-based catalysts can significantly affect the activity and selectivity of the catalysts [10,11].

The synthesis of PdC_x by melting a mixture of palladium and graphite powders in an induction furnace under an argon atmosphere at ambient pressure was realized by Cadevill and Lerner (1976) [12]. The solubility of carbon in the palladium bulk was found to be below x = 0.03. The higher carbon content (x = 0.13(5)) was reported in palladium carbide synthesized from palladium nanoparticles deposed on a carbon substrate [13]. At a temperature of 400 K in acetylene and hydrogen atmosphere at 1 bar, either hydrides or carbides formed depending on the partial pressure of hydrogen and acetylene.

Palladium carbides and hydrides are rather alloys than ionic compounds. Carbon or hydrogen atoms occupy octahedral interstitial sites of the *fcc* palladium structure that results in an increase of the lattice parameter without change of the symmetry.

In this work, we report on the synthesis of carbon-rich Pd-alloys, $PdC_{0.19}$ and $PdC_{0.21}$, and palladium hydride (PdH) in a laser heated diamond anvil cell through a chemical reaction of Pd with either carbon or paraffin oil. The samples were characterized using powder X-ray diffraction at the high-pressure diffraction beamline ID15B at the ESRF (the European Synchrotron Radiation Facility, Grenoble). The compressional behavior of the samples was studied up to 50 GPa. Reference data on the compressibility of palladium were obtained up to about 30 GPa.

2. Experimental methods

Here we present the results of four experiments. In all experiments, we used the BX90-type large X-ray aperture DACs equipped with Boehler–Almax type diamonds (culet diameter 250 μm). The sample chamber was formed by pre-indenting of a rhenium gasket

to ~25μm thickness and drilling a hole of ~100 μm in diameter in the center of the indentation.

In the first two experiments (DAC1 and DAC2), a Pd foil was loaded into the sample chamber along with a Ne gas (compressed to about 1.2 kbar), which was used as a pressure transmitting medium and a pressure marker. In the experiment DAC3, a piece of a Pd foil was clamped between two thin layers of NaCl inside the sample chamber in order to reduce the temperature gradients in the sample during laser heating. Paraffin oil was used in the experiment DAC4 as both a pressure-transmitting medium and a reagent for Pd hydride synthesis. The pressure was determined using the equations of states (EOSes) of NaCl[14] and Ne [15] and monitored additionally on the Raman signal from the diamond anvils [16].

The laser-heating (LH) of the samples was performed using an in-house laser heating setup [17]. The LH system is equipped with two YAG lasers (1064 nm central wavelength) and the IsoPlane SCT 320 spectrometer with a 1024x2560 PI-MAX 4 camera for the collection of thermal emission spectra from the heated spot. Temperatures were estimated by the fitting of thermal emission spectra of the sample to the grey body approximation of Planck's radiation function in a given wavelength range (570-830 nm).

X-ray diffraction experiments were carried out at the high-pressure diffraction beamline ID15B of the ESRF. Powder diffraction images at ambient temperatures were collected during continuous rotation of a DAC from – 20° to + 20° ω with an acquisition time of 2 seconds under incident monochromatic X-ray beam (λ = 0.4117 Å, $\Delta\lambda/\lambda \sim 10^{-4}$) using a MAR555 flat panel detector. Conventional diffraction patterns were obtained by integration of X-ray diffraction images to the intensity profile as a function of 2θ angle using Dioptas software [18] and were analyzed with the Le Bail fitting technique using TOPAS 4.2. The EOSes of the synthesized materials were obtained by fitting the pressure-volume dependence data using the EoSFit7-GUI [19].

3. Results and discussion

3.1. EOS of Pd (DAC 1)

To detect the effect of possible carbon (or hydrogen) dissolution in palladium, data on the compressibility of pure Pd metal are required. A piece of Pd foil was loaded into a sample chamber of a DAC along with Ne and pressurized stepwise (with a step of 2-3 GPa) up to about 30 GPa. Table 1 presents the unit cell volume of Pd as a function of pressure.

Table 1. The pressure dependence of the unit cell parameter of Pd. Pressure was determined using the EOS of Ne [15].

P, GPa	V, Å^3
0	58.868(2)
6.9(2)	56.709(3)
7.9(2)	56.476(3)
9.5(2)	56.121(3)
11.2(2)	55.743(3)
13.2(2)	55.324(3)
15.6(2)	54.847(3)
17.8(2)	54.448(3)
19.6(2)	54.134(3)
21.4(2)	53.828(3)
23.3(2)	53.517(3)
25.2(2)	53.246(3)
27.2(2)	52.965(3)
29.5(2)	52.667(3)
31.2(2)	52.411(3)

The experimental pressure-volume data of Pd were fitted using the 3rd order Birch-Murnaghan equation of state (BM3 EOS) (**Figure 1(a)**):

$$\mathbf{P} = \frac{3K_0}{2} \cdot \left[\left(\frac{V_0}{V}\right)^{\frac{7}{3}} - \left(\frac{V_0}{V}\right)^{\frac{5}{3}}\right] \cdot \left\{1 - \frac{3}{4}(4 - K') \cdot \left[\left(\frac{V_0}{V}\right)^{\frac{2}{3}} - 1\right]\right\} \quad (1)$$

where P is the pressure, V_0 is the volume at ambient pressure, V is the volume at pressure P, K_0 is the bulk modulus, and K_0' is the pressure derivative of K_0.

The parameters of the equations were found to be: V_0= 58.868(2) Å^3 K_0 = 157(3) GPa, and K' = 9.9(4). The volume of the Pd unit cell at ambient pressure (58.868 Å^3) is in good agreement with literature data (V_0 = 58.85[20], 58.9 [21]).

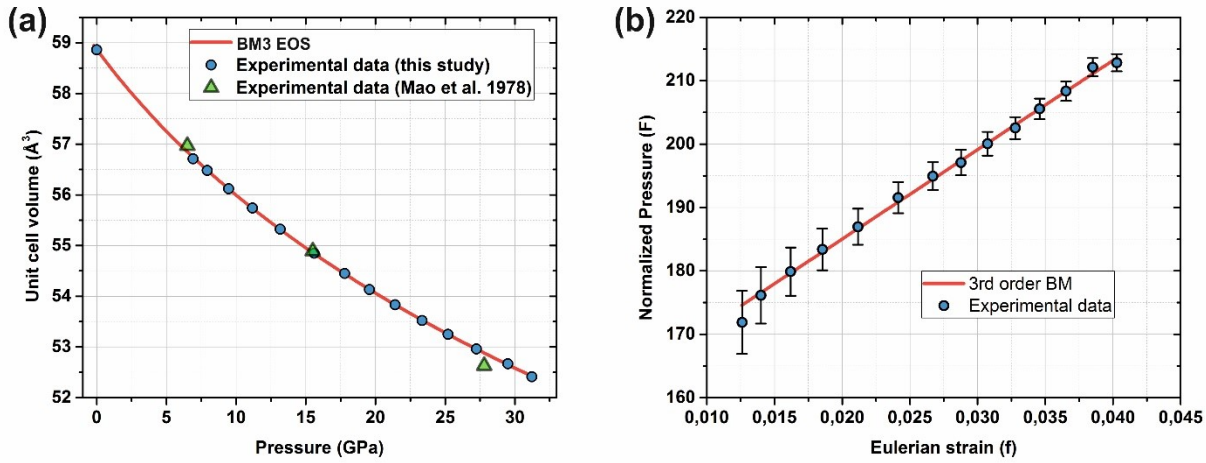

Figure 1. The pressure dependence of the unit cell volume of Pd (a) and the Eulerian strain – normalized pressure (f-F) plot of the experimental data (b). Our experimental points are shown by circles. The solid curve is the fit of the experimental P-V data using the BM3 EOS with the following parameters: V_0= 58.868(2) Å^3, K_0= 157(3) GPa, K'= 9.9(4). Errors in experimental data are within the symbol size.

The F-f plot shown in **Figure 1(b)** indicates a good quality of fit of experimental data with the BM3 EOS and confirms that there are no structural phase transitions in Pd on compression up to 30 GPa. The bulk modulus and its pressure derivative obtained in this work do not agree well with the values reported previously by Mao et al. (1978) (V_0 = 58.45 Å^3, K_0 = 183 GPa, K' = 5.28) [5,22]. A reason for the apparent inconsistency is unclear, but it might be due to Mao et al. had only 5 experimental points in the range of 0 -100 GPa obtained in two different experiments, and water or methanol-ethanol mixture used as a pressure medium [22] created highly non-hydrostatic conditions above ~15 GPa. If we fit our data using the K' parameter fixed on the value reported in [22] (K' = 5.28), then we get K_0=190(2) GPa that is reasonably close to the value reported in [22]. We admit that $K' = 9.9(4)$ obtained in our work is rather unusual for transition metals (for most of the pure transition metals K_0' varies within the range of 3.5-6 [23]) and further studies are needed to clarify this phenomenon.

3.2. The chemical reaction of Pd with a diamond anvil at high pressure and temperature

3.2.1. Pd in Ne pressure transmitting medium (DAC 2)

In the DAC2, the sample of Pd foil was pressurized in Ne pressure-transmitting medium to 52(1) GPa. The sample was laser heated from both sides by scanning with a laser beam through the whole surface of the sample. During continuous-wave laser heating of the sample at constant laser power, the temperature varied from 2500(200) to 3000(200) K in different parts of the sample. The examples of high-pressure X-ray diffraction patterns of the sample before and after laser heating are shown in **Figure 2**.

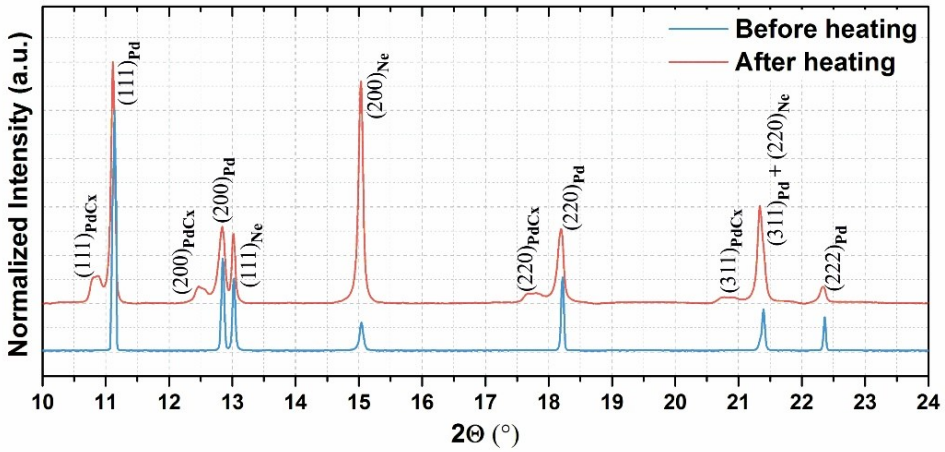

Figure 2. Diffraction patterns of the Pd sample in a Ne pressure transmitting medium before and after laser heating at 52(1) GPa. The *fcc* PdC_x was formed after laser heating of Pd at 2500(200) – 3000(200) K. Indexes of the diffraction peaks of palladium (Pd), pallidum carbide (PdC_x), and neon (Ne) are designated (λ = 0.4111 Å).

The new peaks appearing after laser heating are readily indexed as those of the *fcc* structure. The unit cell volume of the new phase is significantly larger than that of pure Pd at a similar pressure and we interpreted this phase as palladium carbide, PdC_x formed due to a reaction between Pd and carbon from the diamond anvil.

Close examination of the individual reflections of PdC_x shows that all of them are split (see **Figure 3** featuring the (111) reflection of Pd and two split (111) reflections of PdC_x). This fact makes us suggest that we are dealing with a material with a range of compositions (varying carbon content, x).

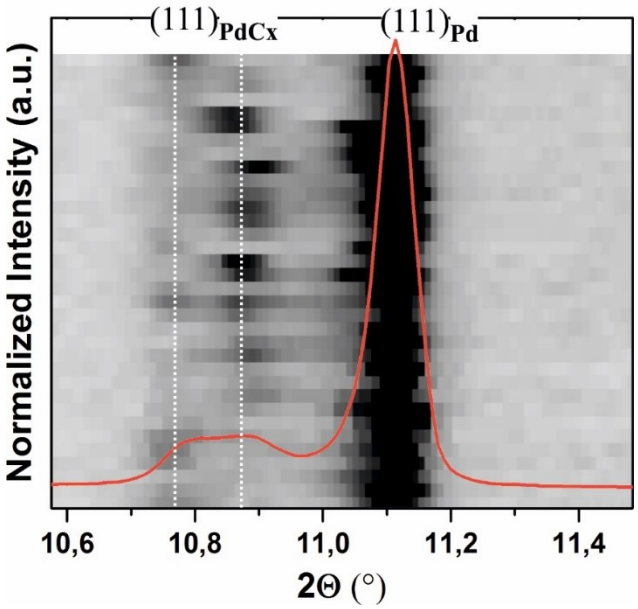

Figure 3. The (111) reflection of Pd and PdC_x phases at 52(2) GPa. The unit cell volume of Pd is 49.738(5) $Å^3$. The unit cell volumes of two different phases of PdC_x with different carbon content are 52.85(2) $Å^3$ and 54.31(2) $Å^3$.

A conventional chemical analysis (with a microprobe, for example) is impossible on the very small samples we synthesized in DACs, so we had to rely on our estimation of the chemical composition of PdC_x using Vegard's law and the known unit cell volumes of pure Pd and $PdC_{0.03}$ [12]. The phase with the largest amount of carbon was determined as $PdC_{0.21(1)}$. The smallest content of carbon was found to be x=0.15(1). One of the possible explanations of the observed phenomenon is the temperature dependence of the solubility of carbon in palladium that leads to the formation of a plethora of PdC_x compositions at conditions of large temperature gradients during laser heating. More homogeneous temperature distribution in the heated spot could probably promote the synthesis of a carbide of single chemical composition.

Upon decompression to ambient pressure, all peaks of PdC_x remain split and demonstrate similar behavior. We followed changes in the lattice parameters for various PdC_x phases with pressure (**Figure 4(a)**) and determined the parameters of the BM3 EOS for $PdC_{0.21(1)}$. The fitting of the P-V data for $PdC_{0.21(1)}$ gives V_0 = 65.1(1) $Å^3$, K_0 = 241(9) GPa and K' = 2.1(3). The Eulerian strain-normalized pressure (f-F) plot of the data based

on the Birch-Murnaghan equation of state is shown in **Figure 4(b)**. The solid line represents the linear fit which evidences an appropriate choice of the BM3 EOS.

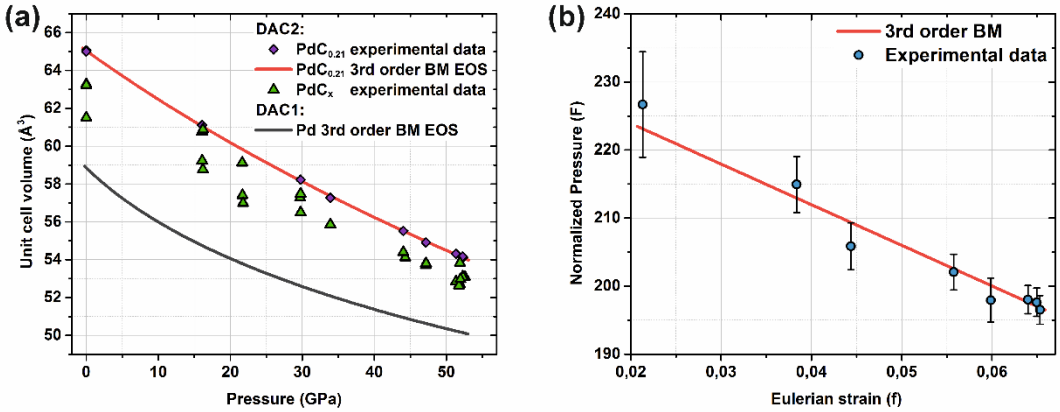

Figure 4. (a) The pressure-volume dependence for a few PdC_x. phases with different carbon content from x=0.15(1) to x=0.21(1). Green triangles and purple diamonds represent experimental results; the solid red curve is the BM3 EOS fit for $PdC_{0.21(1)}$ (V_0 = 65.1(1) Å^3, K_0 = 241(9) GPa and K' = 2.1 (0.3)). All error bars are within the size of the symbol. (b) Eulerian strain – normalized pressure (f-F) plot of the synthesized $PdC_{0.21}$ phase based on the BM3 EOS. The circles and solid lines represent experimental data points and their fit, correspondently.

3.2.2. Pd in NaCl pressure transmitting medium (DAC 3)

A piece of Pd foil was clamped between two thin layers of NaCl inside the sample chamber of DAC 3 and compressed up to 58(2) GPa. NaCl was chosen as a pressure transmitting medium due to its better thermal insulating properties, as compared to Ne [24], which can reduce thermal gradients in the sample during its laser heating. An example of the diffraction pattern collected after laser heating of the sample at 2500(200) K is shown in **Figure 5**.

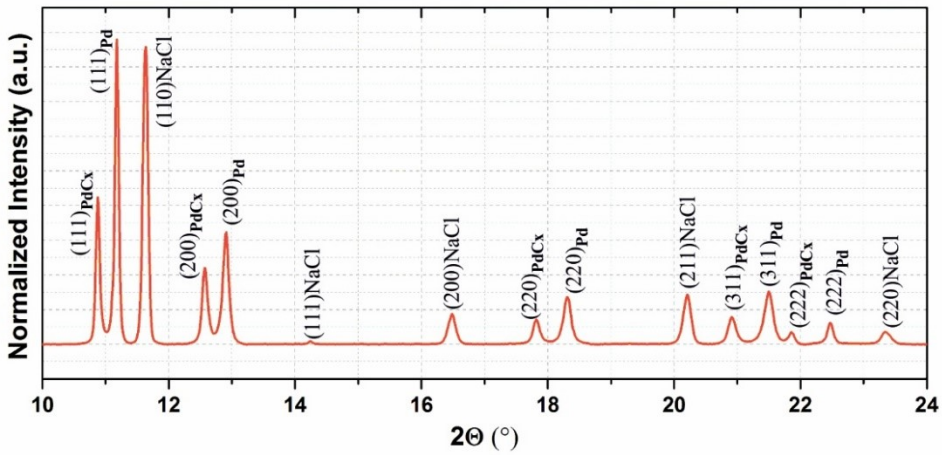

Figure 5. The diffraction pattern of the Pd sample in a NaCl pressure transmitting medium after laser heating at 58(2) GPa. The *fcc* PdC_x (x=0.19(1)) was formed after laser heating of Pd at 2500(200) K. Indexes of the diffraction peaks of palladium (Pd), palladium carbide (PdC_x), and B2-structured sodium chloride (NaCl) are designated (λ = 0.4113 Å).

Unlike the experiment DAC2, with Ne as a pressure-transmitting medium, no peak splitting of PdC_x was detected here. This supports our suggestion of the temperature dependence of carbon's solubility in palladium.

The DAC3 was decompressed in several steps to ambient pressure; powder diffraction data were collected at each pressure point. The P-V data of the PdC_x phase, identified as $PdC_{0.19(1)}$ on Vegard's law, was fitted using the BM3 EOS (**Figure 6)** that gave V_0 = 64.51(5) $Å^3$, K_0 = 189(8) GPa, and K' = 4.5(4).

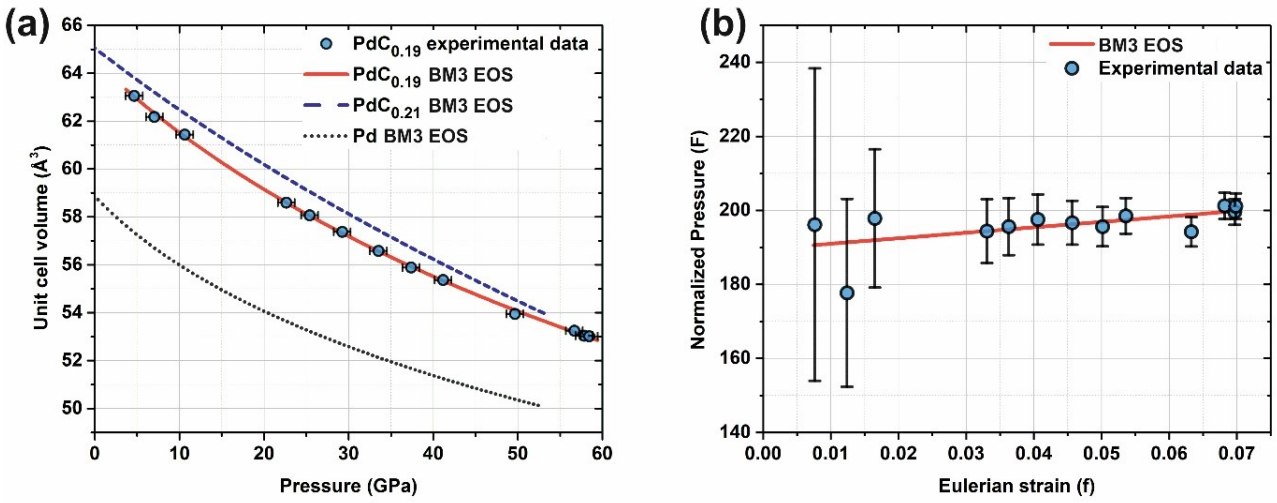

Figure 6. (a) The pressure-volume dependence of $PdC_{0.19(1)}$. The dots represent experimental results, the solid curve is the fit to the BM3 EOS (V_0 = 64.51(5) Å^3, K_0 = 189(8) GPa and K' = 4.5(4)). All error bars are within the size of the symbol. (b) Eulerian strain – normalized pressure (f-F) plot of the synthesized $PdC_{0.19}$ phase based on the BM3 EOS. The circles and solid lines represent experimental results and their fit correspondingly.

The EOS parameters of the two PdC_x phases studied are presented in **Table 2**. There is an apparent difference in the elastic behavior of carbides with very similar compositions (**Figure 6**). Use of the BM3 EOS leads to quite different EOS parameters for Pd, $PdC_{0.19}$, and $PdC_{0.21}$, whereas the BM2 EOS ($K_0' = 4$) gives similar K_0 values for all of them (**Table 2**).

Table 2. Parameters of the BM3 EOSes for pure Pd, $PdC_{0.19}$ and $PdC_{0.21}$.

Sample	V_0, Å^3	K_0, GPa	K'	K_0, GPa (K'= 4)
Pd	58.863(2)	157(3)	9.9(4)	203(3)
$PdC_{0.19(1)}$	64.51(5)	189(8)	4.5 (4)	203(5)
$PdC_{0.21(1)}$	65.1(1)	241(9)	2.1(3)	198(2)

3.3. The chemical reaction of Pd with paraffin oil at high pressure and high temperature (DAC 4)

It is known that laser heating of metal in paraffin oil in a DAC may lead to the synthesis of carbides (sometimes together with hydrides) [25]. In this experiment, a piece of Pd foil was loaded inside the sample chamber of a DAC along with paraffin oil, which served as both a pressure-transmitting medium and a source of carbon and hydrogen. The sample was compressed up to 39(2) GPa (close to the pressure at which PdC_x were synthesized in DAC 2 and DAC 3), and laser-heated from both sides at 1500(200) K. Powder X-ray diffraction pattern of the temperature quenched sample (**Figure 7**) features two sets of reflections which were assigned to diamond (D) and the *fcc*-structured phase with the lattice parameter a=3.918(2) Å.

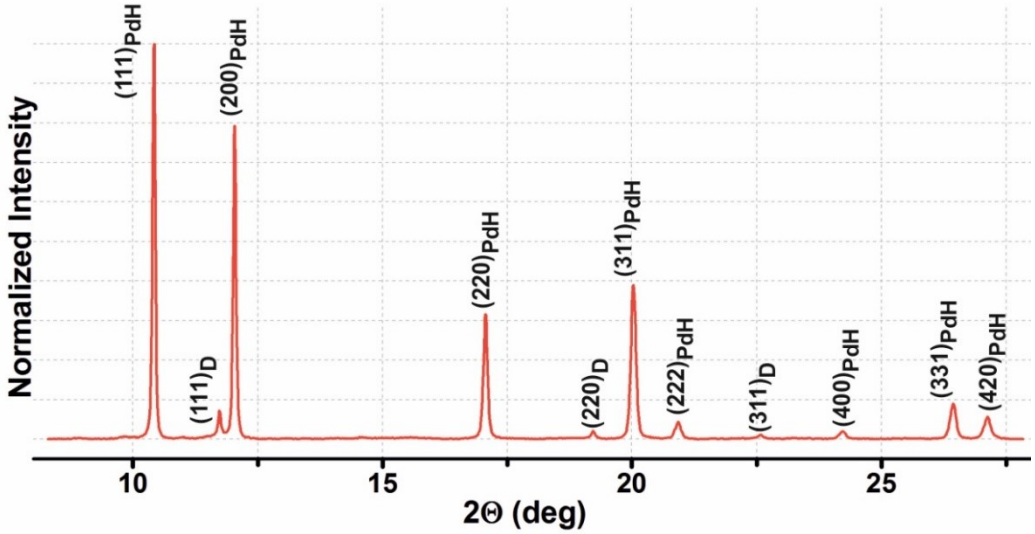

Figure 7. A diffraction pattern of palladium hydride at 39 (2) GPa and ambient temperature. The *fcc* PdH_x (x≈1) along with diamond was formed after laser heating of Pd in paraffin at 1500(200) K and 39(2) GPa. Indexes of the diffraction peaks of palladium hydride (PdH) and diamond (D) are designated (λ = 0.4117 Å). The unit cell volume of PdH is 60.18(5) $Å^3$.

The unit cell volume of the *fcc*-phase (60.18(5) $Å^3$) at 39(2) GPa is too large to allow identifying it as an *fcc*-PdC_x carbide, but within the uncertainty of the measurements, the volume agrees well with the unit cell volume (60.1(1) $Å^3$) of *fcc* palladium hydride PdH at the pressure of 39 GPa [5]. Thus we could suggest that the reaction of pure Pd and paraffin oil at ~39 GPa and ~1500(200) K results in the synthesis of PdH compound and diamond. This observation shows a method of synthesis of PdH at high pressure in DACs

which does not require special equipment (like a high-pressure hydrogen gas loader) if the hydride is produced through a direct reaction between metal and hydrogen.

4. Conclusion

In the presented work we synthesized Pd carbides and Pd hydride in laser heated diamond anvil cells. We used synchrotron X-ray diffraction to determine the composition of the synthesized phases and study their equations of state at room temperature. It was shown that pure Pd metal reacts with carbon from the diamond anvil at high pressure and high temperature conditions that result in the formation of a number of PdC_x phases of different compositions in the case of the use of Ne as a pressure medium. We interpreted this observation as to be due to inhomogeneous heating of the samples and the temperature dependence of carbon's solubility in Pd. The use of NaCl as a pressure transmitting medium resulted in the formation of a single ($PdC_{0.19}$) carbide. Additionally, we showed a possibility of the synthesis of PdH at high pressure in DACs by a direct chemical reaction of Pd and paraffin oil.

5. Acknowledgments

N.D. and L.D. thank the Federal Ministry of Education and Research, Germany (BMBF, grants No. 5K16WC1 and No. 05K19WC1) and the Deutsche Forschungsgemeinschaft (DFG projects DU 954-11/1, DU 393-9/2, and DU 393-13/1) for financial support. N.D. thanks the Swedish Government Strategic Research Area in Materials Science on Functional Materials at Linköping University (Faculty Grant SFO-Mat-LiU No. 2009 00971).

6. References

[1] F.D. Manchester, A. San-Martin, J.M. Pitre, The H-Pd (hydrogen-palladium) System, J. Phase Equilibria. 15 (1994) 62–83. doi:10.1007/BF02667685.

[2] B.D. Adams, A. Chen, The role of palladium in a hydrogen economy, Mater. Today. 14 (2011) 282–289. doi:10.1016/S1369-7021(11)70143-2.

[3] B. Stritzker, W. Buckel, Superconductivity in the palladium-hydrogen and the palladium-deuterium systems, Zeitschrift Für Phys. A Hadron. Nucl. 257 (1972) 1–8. doi:10.1007/BF01398191.

[4] T. Skoskiewicz, Superconductivity in the palladium-hydrogen and palladium-nickel-hydrogen systems, Phys. Status Solidi. 11 (1972) K123–K126. doi:10.1002/pssa.2210110253.

[5] K. Brownsberger, M. Ahart, M. Somayazulu, C. Park, S.A. Gramsch, R.J. Hemley, X-ray Diffraction, Lattice Structure, and Equation of State of PdH x and PdD x to Megabar Pressures, J. Phys. Chem. C. 121 (2017) 27327–27331. doi:10.1021/acs.jpcc.7b09290.

[6] R. Pellegrini, G. Agostini, E. Groppo, A. Piovano, G. Leofanti, C. Lamberti, 0.5wt.% Pd/C catalyst for purification of terephthalic acid: Irreversible deactivation in industrial plants, J. Catal. 280 (2011) 150–160. doi:10.1016/j.jcat.2011.03.012.

[7] D. Teschner, J. Borsodi, A. Wootsch, Z. Revay, M. Havecker, A. Knop-Gericke, S.D. Jackson, R. Schlogl, The Roles of Subsurface Carbon and Hydrogen in Palladium-Catalyzed Alkyne Hydrogenation, Science (80-.). 320 (2008) 86–89. doi:10.1126/science.1155200.

[8] A. Lazzarini, A. Piovano, R. Pellegrini, G. Leofanti, G. Agostini, S. Rudić, M.R. Chierotti, R. Gobetto, A. Battiato, G. Spoto, A. Zecchina, C. Lamberti, E. Groppo, A comprehensive approach to investigate the structural and surface properties of activated carbons and related Pd-based catalysts, Catal. Sci. Technol. 6 (2016) 4910–4922. doi:10.1039/C6CY00159A.

[9] A. Borodziński, G.C. Bond, Selective Hydrogenation of Ethyne in Ethene-Rich Streams on Palladium Catalysts. Part 1. Effect of Changes to the Catalyst During Reaction, Catal. Rev. 48 (2006) 91–144. doi:10.1080/01614940500364909.

[10] M.W. Tew, M. Nachtegaal, M. Janousch, T. Huthwelker, J.A. van Bokhoven, The irreversible formation of palladium carbide during hydrogenation of 1-pentyne over silica-supported palladium nanoparticles: in situ Pd K and L3 edge XAS, Phys. Chem. Chem. Phys. 14 (2012) 5761. doi:10.1039/c2cp24068h.

[11] D. Teschner, J. Borsodi, Z. Kis, L. Szentmiklósi, Z. Révay, A. Knop-Gericke, R. Schlögl, D. Torres, P. Sautet, Role of Hydrogen Species in Palladium-Catalyzed

Alkyne Hydrogenation, J. Phys. Chem. C. 114 (2010) 2293–2299. doi:10.1021/jp9103799.

[12] M.C. Cadeville, C. Lerner, On the electronic structure of interstitial transition-metal based alloys with boron and carbon impurities, Philos. Mag. 33 (1976) 801–824. doi:10.1080/14786437608221917.

[13] A.L. Bugaev, A.A. Guda, A. Lazzarini, K.A. Lomachenko, E. Groppo, R. Pellegrini, A. Piovano, H. Emerich, A. V. Soldatov, L.A. Bugaev, V.P. Dmitriev, J.A. van Bokhoven, C. Lamberti, In situ formation of hydrides and carbides in palladium catalyst: When XANES is better than EXAFS and XRD, Catal. Today. 283 (2017) 119–126. doi:10.1016/j.cattod.2016.02.065.

[14] P.I. Dorogokupets, A. Dewaele, Equations of state of MgO, Au, Pt, NaCl-B1, and NaCl-B2: Internally consistent high-temperature pressure scales, High Press. Res. 27 (2007) 431–446. doi:10.1080/08957950701659700.

[15] Y. Fei, A. Ricolleau, M. Frank, K. Mibe, G. Shen, V. Prakapenka, Toward an internally consistent pressure scale, Proc. Natl. Acad. Sci. 104 (2007) 9182–9186. doi:10.1073/pnas.0609013104.

[16] Y. Akahama, H. Kawamura, Pressure calibration of diamond anvil Raman gauge to 310GPa, J. Appl. Phys. 100 (2006) 043516. doi:10.1063/1.2335683.

[17] T. Fedotenko, L. Dubrovinsky, G. Aprilis, E. Koemets, A. Snigirev, I. Snigireva, A. Barannikov, P. Ershov, F. Cova, M. Hanfland, N. Dubrovinskaia, Laser heating setup for diamond anvil cells for in situ synchrotron and in house high and ultra-high pressure studies, Rev. Sci. Instrum. 90 (2019) 104501. doi:10.1063/1.5117786.

[18] C. Prescher, V.B. Prakapenka, DIOPTAS : a program for reduction of two-dimensional X-ray diffraction data and data exploration, High Press. Res. 35 (2015) 223–230. doi:10.1080/08957959.2015.1059835.

[19] J. Gonzalez-Platas, M. Alvaro, F. Nestola, R. Angel, EosFit7-GUI : a new graphical user interface for equation of state calculations, analyses and teaching, J. Appl.

Crystallogr. 49 (2016) 1377–1382. doi:10.1107/S1600576716008050.

[20] H.F. McMurdie, M.C. Morris, E.H. Evans, B. Paretzkin, W. Wong-Ng, L. Ettlinger, C.R. Hubbard, Standard X-Ray Diffraction Powder Patterns from the JCPDS Research Associateship, Powder Diffr. 1 (1986) 64–77. doi:10.1017/S0885715600011593.

[21] C.N. Rao, K.K. Rao, EFFECT OF TEMPERATURE ON THE LATTICE PARAMETERS OF SOME SILVER–PALLADIUM ALLOYS, Can. J. Phys. 42 (1964) 1336–1342. doi:10.1139/p64-120.

[22] H.K. Mao, P.M. Bell, J.W. Shaner, D.J. Steinberg, Specific volume measurements of Cu, Mo, Pd, and Ag and calibration of the ruby R 1 fluorescence pressure gauge from 0.06 to 1 Mbar, J. Appl. Phys. 49 (1978) 3276–3283. doi:10.1063/1.325277.

[23] S. Raju, E. Mohandas, V.S. Raghunathan, The pressure derivative of bulk modulus of transition metals: An estimation using the method of model potentials and a study of the systematics, J. Phys. Chem. Solids. 58 (1997) 1367–1373. doi:10.1016/S0022-3697(97)00024-3.

[24] I. Uts, K. Glazyrin, K.K.M. Lee, Effect of laser annealing of pressure gradients in a diamond-anvil cell using common solid pressure media, Rev. Sci. Instrum. 84 (2013) 103904. doi:10.1063/1.4821620.

[25] O. Narygina, L.S. Dubrovinsky, C.A. McCammon, A. Kurnosov, I.Y. Kantor, V.B. Prakapenka, N.A. Dubrovinskaia, X-ray diffraction and Mössbauer spectroscopy study of fcc iron hydride FeH at high pressures and implications for the composition of the Earth’s core, Earth Planet. Sci. Lett. 307 (2011) 409–414. doi:10.1016/j.epsl.2011.05.015.

Section 5.D.

Synthesis and compressibility of novel nickel carbide at pressures of Earth's outer core

T. Fedotenko[1,*], S. Khandarkhaeva[1], L. Dubrovinsky[2], K. Glazyrin[3], P. Sedmak[4] and N. Dubrovinskaia[1, 5]

[1]*Material Physics and Technology at Extreme Conditions, Laboratory of Crystallography, University of Bayreuth, D-95440 Bayreuth, Germany*

[2]*Bayerisches Geoinstitut Universität Bayreuth, D-95440 Bayreuth, Germany*

[3]*Petra III, P02, Deutsches Elektronen Synchrotron, 22607 Hamburg, Germany*

[4]*European Synchrotron Radiation Facility, F-38043 Grenoble, France*

[5]*Department of Physics, Chemistry and Biology (IFM), Linköping University, SE-581 83, Linköping, Sweden*

Minerals 2021, 11(5), 516; May 2021
DOI: 10.3390/min11050516

Abstract: We report the high-pressure synthesis and the equation of state (EOS) of a novel nickel carbide (Ni_3C) It was synthesized in a diamond anvil cell at 184(5) GPa through a direct reaction of a nickel powder with carbon from the diamond anvils upon heating at 3500(200) K. Ni_3C has the cementite-type structure (*Pnma* space group, a = 4.519(2) Å, b = 5.801(2) Å, c = 4.009(3) Å), which was solved and refined based on *in situ* synchrotron single-crystal X-ray diffraction. The pressure-volume data of Ni_3C was obtained on decompression at room temperature and fitted to the 3rd order Burch-Murnaghan equation of state with the following parameters: V_0 = 147.7(8) Å^3, K_0 = 157(10) GPa and K_0' = 7.8(6). Our results contribute to the understanding of the phase composition and properties of Earth's outer core.

Keywords: Nickel Carbide, High pressure, X-ray Diffraction, Equation of State, Earth's outer core.

* Corresponding author, email: TimofeyFedotenko@gmail.com

1. Introduction

Nickel is known as the second most abundant element in Earth's core after iron (Birch, 1952; Prescher et al., 2015). Cosmochemical models and studies of meteorites suggest that Earth's core apart of Fe contains also about 5 wt. % of Ni (Litasov and Shatskiy, 2016; McDonough, 2003) and, in the inner core, up to 10 wt. % of light elements (Poirier, 1994; Torchio et al., 2020; Wood, 1993). Which elements exactly and their amount is a subject of active discussions (Litasov and Shatskiy, 2016). A large amount of carbon in iron meteorites (Bashir et al., 1996), its high solubility in liquid Fe at high pressure (Hirayama et al., 1993; Wood, 1993), and high abundance in the solar system (Wood, 1993), suggest carbon be one of the most important light elements in Earth's core. Modern estimations of the inner core composition indicate up to 2.0 wt. % of carbon (Litasov and Shatskiy, 2016). All these facts resulted in numerous high-pressure studies of the Fe-C system over the last decades. The intermediate Fe-C compounds Fe_3C and Fe_7C_3 were suggested to be the most likely candidates to the carbon-bearing phases in Earth's core, as they were found at relevant pressures and temperatures (Chen et al., 2014; Lord et al., 2009; Nakajima et al., 2009; Prescher et al., 2015; Wood, 1993). Although at room temperature Fe_3C was shown to be stable up to 187 GPa, it decomposes into a mixture of solid Fe_7C_3 and hcp-Fe at above 145 GPa upon laser heating and transforms into Fe-C liquid and solid Fe_7C_3 at temperatures of above 3400 K (Liu et al., 2016). Moreover, the high Poisson's ratio of Fe_7C_3 at high pressures (Prescher et al., 2015) indicates that the presence of carbon may significantly affect the elastic properties of iron. This corroborates well with the Preliminary Reference Earth Model (PREM) (Dziewonski and Anderson, 1981), which shows that Earth's inner core also has a high Poisson's ratio.

Contrary to the binary iron-carbon system, the Fe – Ni – C, and Ni – C systems at high PT conditions are still poorly understood. Nickel can strongly modify the physical properties of pure Fe at elevated pressures and temperatures. Recent studies have shown that Ni alloying on Fe doesn't affect the melting temperature of Fe up to 100 GPa, however, modifies its phase boundary by shifting the hcp/fcc/liquid triple point to the higher pressure and temperature region (Torchio et al., 2020). For example, for Fe-20

wt.% Ni alloy the triple point was found to be at 170(20) GPa and 4000(400) K (Torchio et al., 2020) as compared to 100(10) GPa and 3500(200) K for pure Fe (Morard et al., 2018). Pressure-induced Invar effect in Fe-Ni alloys was reported by Dubrovinsky et al. in 2001. The thermal expansion of the alloys $Fe_{0.55}Ni_{0.45}$ and $Fe_{0.20}Ni_{0.80}$ was found to be extremely low in the temperature interval of 291 K to 500 K at pressures of 7.7 and 12.6 GPa, correspondingly (Dubrovinsky et al., 2001). It was also proven that alloys of Fe with Ni have significantly higher strength in comparison with pure Fe (Reagan et al., 2018). The mineral cohenite, $(Fe, Ni)_3C$, which is isostructural to Fe_3C, was found in iron meteorites(Brett, 1966) and predicted to be stable at high pressures (Ringwood, 1960). However, a pure-Ni cementite-type phase (Ni_3C) has never been reported before.

Here, we report the synthesis and EOS of a novel high-pressure phase of nickel carbide (Ni_3C) in a laser-heated diamond anvil cell (LHDAC) at 184(5) GPa and 3500(200) K. It has the orthorhombic cementite-type structure (Pnma, a = 4.519(2) Å, b = 5.801(2) Å, c = 4.009(3) Å), which was solved and refined using *in situ* synchrotron single-crystal X-ray diffraction.

2. Materials and Methods

In our experiments, we used the BX90-type large X-ray aperture Diamond Anvil Cell (DAC) equipped with Boehler–Almax type diamonds with 80 μm culet diameter. To form the sample chamber, a rhenium gasket was pre-indented to ~ 20 μm thickness and a hole of 40 μm in diameter was drilled in the center of the indentation. A nickel powder was clamped between two thin layers of LiF inside the DAC's sample chamber. LiF played a role of a pressure transmitting and thermal insulating medium in order to decrease temperature gradients in the sample during laser heating. The pressure was determined using the equations of states (EOSes) of Ni(Dewaele et al., 2008) and monitored additionally using Raman signal from the diamond anvils (Akahama and Kawamura, 2006).

The laser-heating (LH) of the samples was performed using in house laser heating setup(Fedotenko et al., 2019). The double-sided LH system is equipped with two YAG lasers (1064 nm central wavelength) and the IsoPlane SCT 320 spectrometer with a

1024x2560 PI-MAX 4 camera for the collection of thermal emission spectra from the heated spot. Temperatures were determined by fitting of thermal emission spectra of the sample to the grey body approximation of Planck's radiation function in a given wavelength range (570-830 nm).

High pressure single-crystal and powder X-ray diffraction (SCXRD) experiments were carried out at the extreme conditions beamline P02.2 (DESY, Hamburg, Germany) (Liermann et al., 2015) and material science beamline ID11 (ESRF, Grenoble, France). The following beamline setups were used: At P02.2, λ = 0.29 Å, the beam size ~2 × 2 μm^2, a Perkin Elmer XRD 1621 detector; at ID11, λ = 0.30996 Å, the beam size ~ 0.5 × 0.5 μm^2, a Frelon4M detector. Single-crystal XRD data were collected during rotation of the DAC around the vertical ω-axis in a range ±35°. The diffraction images were collected with an exposure time of 5 seconds per frame with an angular step Δω = 0.5°.

To analyze the SCXRD data we used the CrysAlisPro software (Rigaku Oxford Diffraction, 2018). The analysis procedure includes the peak search, finding reflections belonging to a unique single-crystal domain, indexing, and data integration. The crystal structure was solved using ShelXT (Sheldrick, 2015) structure solution program and refined with the JANA 2006 software (Petříček et al., 2016).

Powder diffraction measurements were performed either without or upon continuous sample rotation about the ω axis of a diffractometer in the range of ±20°. The images were integrated into powder patterns with Dioptas software (Prescher and Prakapenka, 2015) and analyzed with Le Bail fitting technique using TOPAS 4.2. The parameters of the equation of state were obtained by fitting the pressure-volume data using EoSFit7-GUI software (Gonzalez-Platas et al., 2016).

3. Results and discussion

Sample of Ni foil was pressurized in LiF pressure-transmitting medium up to 184 (5) GPa and laser-heated up to 3500 (200) K by scanning the Ni sample with a laser beam. A direct reaction between Ni and carbon from the diamond anvil resulted in the synthesis of a new compound indexed as orthorhombic (figure 1).

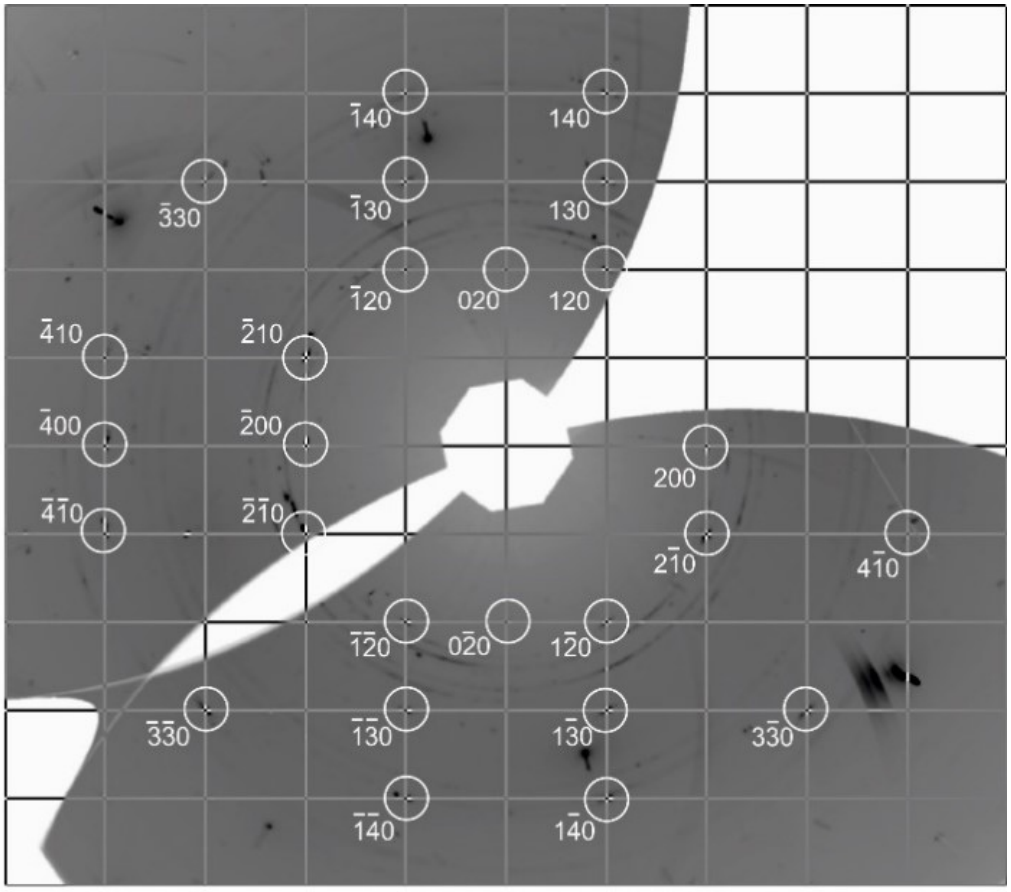

Figure 1. Reconstructed reciprocal lattice planes of orthorhombic Ni_3C compound with the cementite-type structure.

To localize the point of interest, high-resolution two-dimensional X-ray diffraction mapping (40x40 steps of 1 μm each) through the whole sample was realized at the ID11 beamline at the ESRF (figure 2).

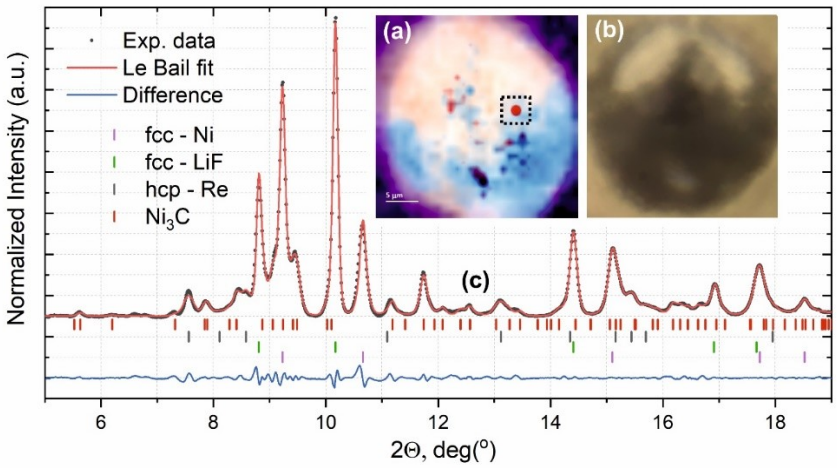

Figure 2. (a) Two-dimensional X-ray diffraction mapping of the sample chamber. The color map allowing to distinguish between the present phases. The intensity of the colors is proportional to the intensity of particular reflections: the dark purple region beyond the pressure chamber corresponds to the (100) and (101) reflections of the Re gasket; the blue region – the (200) reflection of the Ni; The orange region – the (111) reflection of LiF; (020) and (301) reflection of Ni_3C for the red region. (b) A comparison view of the sample chamber under an optical microscope. (c) Powder diffraction pattern collected from the sample at the position highlighted by a black dotted square on the XRD color map.

The reaction products consist of numerous single-crystalline grains that were identified using synchrotron single-crystal XRD. For one of such grains (one domain), we were able to collect 182 independent reflections and reduce the data with R_{int} = 7.3% at 184 (5) GPa. The structure solution and refinement (final R_1 = 6.4%, see Table 1) revealed the cementite-type orthorhombic structure (space group *Pnma, #62*; a = 4.520(3) Å, b = 5.8014(17) Å, c = 4.009(4) Å at 184 (5) GPa) and the Ni_3C chemical composition (Table 1).

Table 1. Crystallographic data for the Ni_3C at 184(5) GPa and 293 K.

Composition	Ni_3C	Density($g \cdot cm^{-3}$)	11.884
Crystal system	Orthorombic	Radiation type	synchrotron, λ = 0.2895 Å
Space group	Pnma	μ (mm^{-1})	4.113
temperature (K)	293	Diffractometer	P02.2 @DESY
a (Å)	4.520(3)	Absorption correction	Multi-scan (ABSPACK, CrysAlis PRO 1.171.40.53)
b (Å)	5.8014(17)	No. of measured, Independent and observed [I > 3σ(I)] reflections	366, 182, 83
c (Å)	4.009(4)	R_{int}	7.3%
α (°)	90	θ range values()	3.1 to 16.8
γ (°)	90	Refinement method	Full matrix least squares on F
β (°)	90	R[F > 3σ(F)], wR(F), S	6.43, 8.42, 1.43
V ($Å^3$)	105.12(13)	No. of parameters	19
Z	4	$\Delta\rho_{max}$, $\Delta\rho_{min}$($e \cdot Å^{-3}$)	3.09, -3.51

The structure can be described as built of distorted trigonal prisms formed by six nickel atoms coordinating a C atom (figure 3). The Ni – C distances in the prism vary from 1.7931(11) to 1.8112(13) Å.

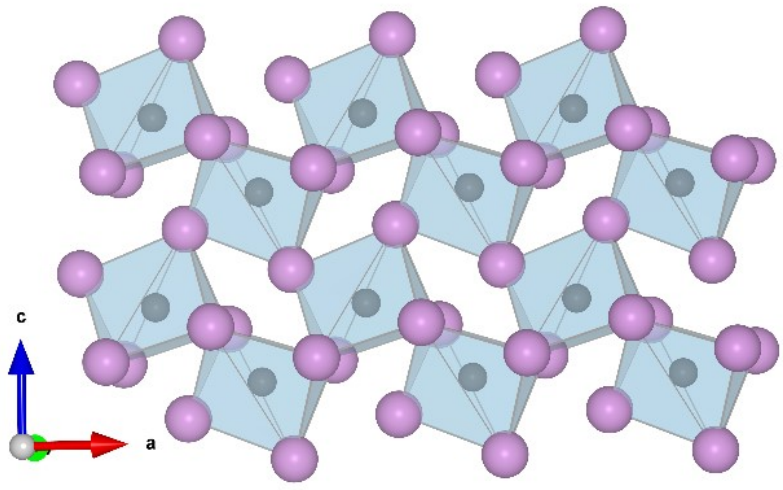

Figure 3. Crystal structure of the cementite type Ni_3C at 184(5) GPa and room temperature. Purple and black spheres designate nickel and carbon atoms, correspondingly.

The Ni_3C sample was studied on a stepwise decompression. SCXRD data were collected at seven pressure points down to 84(2) GPa. Below 84(2) GPa no diffraction pattern from Ni_3C was observed, however, a reason remained unclear. That makes the question if the quality of the sample deteriorated or the phase decomposed or amorphized, stays open. The pressure-volume data of Ni_3C was fitted to the 3rd order Birch-Murnaghan (BM3) EOS and gave the following parameters: V_0 = 147.7(8) Å^3; K_0 = 157(10) GPa, K´ = 7.8(6) (figure 4).

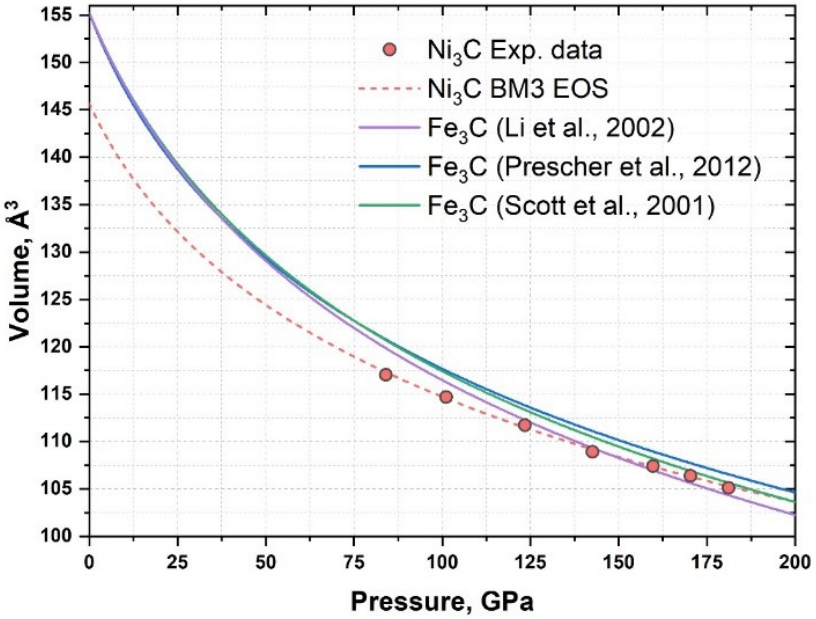

Figure 4. The pressure-volume dependence of Ni_3C. Red dots represent experimental data, the dashed red curve is the BM3 EOS fit (V_0 = 147.7(8) Å^3; K_0 = 157(10) GPa, K´ = 7.8(6)). Solid purple, blue and green lines correspond to the EOSes of Fe_3C from studies of Li et al. (K_0 = 174(6) GPa, K´ = 4.8(8)) (Li et al., 2002), Prescher et al (K_0 = 161(2) GPa, K' = 5.9(2)) (Prescher et al., 2012) and Scott et all (K_0 = 165(4) GPa, K' = 5.99 (9))(Scott et al., 2001).

Based on obtained data, we calculated the bulk sound velocity for Ni_3C as a function of pressure at 293 K and compared it with those known for Fe, Ni, and possible carbon-bearing components of Earth's core (Fe_3C and Fe_7C_3).

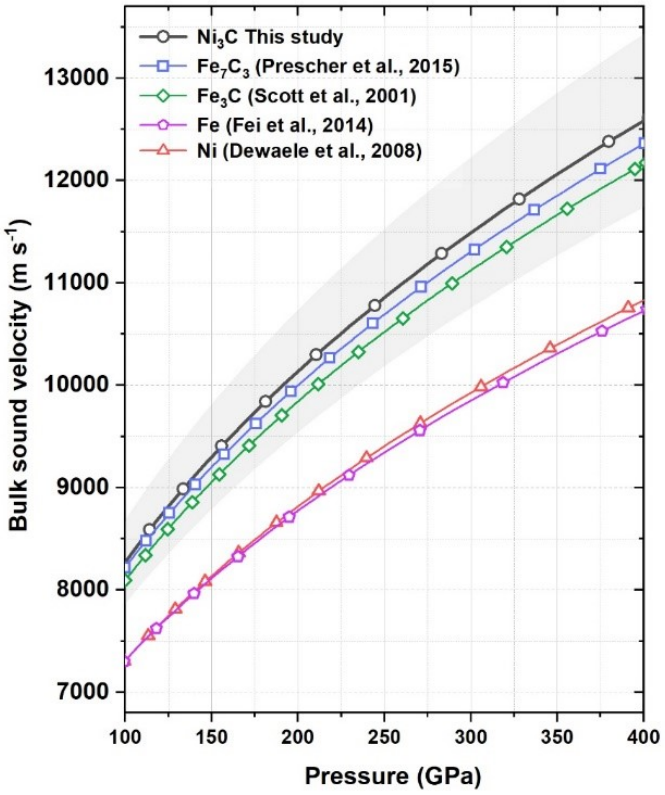

Figure 5. Calculated bulk sound velocity as a function of pressure for Ni_3C (this study, black solid line with circles); Fe_3C (green line with diamonds(Scott et al., 2001)) and Fe_7C_3 (blue line with squares (Prescher et al., 2015)); Ni (red line with triangles (Dewaele et al., 2008)); Fe (purple line with pentagons (Fei et al., 2016)) at 293 K.

Figure 5 shows that within the errors Ni_3C exhibits similar bulk velocities as Fe_3C and Fe_7C_3 at pressures up to 400 GPa. Thereby, the presence of Ni in the alloy likely should not affect the elastic properties of the Fe-Ni-C system at high pressure but potentially can change the carbon distribution. Due to the stability of Ni_3C at conditions of Earth's outer core, it may be considered as one of the likely candidates to carbon-bearing phases in the core along with Fe_7C_3.

4. Conclusion

In the presented work, we have synthesized a nickel carbide yet unknown at ambient conditions. It was shown that Ni reacts with carbon at high-pressure and high-temperature conditions that result in the formation of an orthorhombic Ni_3C compound (space group

Pnma, a = 4.520(3) Å, b = 5.8014(17) Å, c = 4.009(4) Å at 84(5) GPa) with the cementite-type structure revealed using synchrotron single-crystal X-ray diffraction. The Ni_3C was studied on decompression down to 84(2) GPa. We have shown that in the pressure range 84(2) -185(5) GPa, Ni_3C is less compressible than cementite (Fe_3C); the calculated bulk sound velocities are similar to those known for Fe_3C and Fe_7C_3 at pressures up to 400 GPa and 297 K. Ni_3C remains stable at pressure-temperature conditions relevant to Earth's core and thus can be considered as one of the likely candidates to carbon-bearing phases in the core along with Fe_7C_3.

5. Acknowledgments

N.D. and L.D. thank the Federal Ministry of Education and Research, Germany (BMBF, grant No. 05K19WC1) and the Deutsche Forschungsgemeinschaft (DFG projects DU 954-11/1, DU 393-9/2, and DU 393-13/1) for financial support. N.D. thanks the Swedish Government Strategic Research Area in Materials Science on Functional Materials at Linköping University (Faculty Grant SFO-Mat-LiU No. 2009 00971). We acknowledge DESY (Hamburg, Germany), a member of the Helmholtz Association HGF, for the provision of experimental facilities, photon beamline P02.2 (Petra III).

6. Data Availability

The data that support the findings of this study are available from the corresponding author upon reasonable request.

7. References

Akahama, Y., Kawamura, H., 2006. Pressure calibration of diamond anvil Raman gauge to 310GPa. J. Appl. Phys. 100, 043516. https://doi.org/10.1063/1.2335683

Bashir, N., Beckett, J. ~R., Hutcheon, I. ~D., Stolper, E. ~M., 1996. Carbon in the Metal of Iron Meteorites, in: Lunar and Planetary Science Conference, Lunar and Planetary Science Conference. p. 63.

Birch, F., 1952. Elasticity and constitution of the Earth's interior. J. Geophys. Res. 57, 227–286. https://doi.org/10.1029/JZ057i002p00227

Brett, R., 1966. Cohenite in Meteorites: A Proposed Origin. Science (80-.). 153, 60–62.

https://doi.org/10.1126/science.153.3731.60

Chen, B., Li, Z., Zhang, D., Liu, J., Hu, M.Y., Zhao, J., Bi, W., Alp, E.E., Xiao, Y., Chow, P., Li, J., 2014. Hidden carbon in Earth's inner core revealed by shear softening in dense Fe 7 C 3. Proc. Natl. Acad. Sci. 111, 17755–17758. https://doi.org/10.1073/pnas.1411154111

Dewaele, A., Torrent, M., Loubeyre, P., Mezouar, M., 2008. Compression curves of transition metals in the Mbar range: Experiments and projector augmented-wave calculations. Phys. Rev. B 78, 104102. https://doi.org/10.1103/PhysRevB.78.104102

Dubrovinsky, L., Dubrovinskaia, N., Abrikosov, I.A., Vennström, M., Westman, F., Carlson, S., van Schilfgaarde, M., Johansson, B., 2001. Pressure-Induced Invar Effect in Fe-Ni Alloys. Phys. Rev. Lett. 86, 4851–4854. https://doi.org/10.1103/PhysRevLett.86.4851

Dziewonski, A.M., Anderson, D.L., 1981. Preliminary reference Earth model. Phys. Earth Planet. Inter. 25, 297–356. https://doi.org/10.1016/0031-9201(81)90046-7

Fedotenko, T., Dubrovinsky, L., Aprilis, G., Koemets, E., Snigirev, A., Snigireva, I., Barannikov, A., Ershov, P., Cova, F., Hanfland, M., Dubrovinskaia, N., 2019. Laser heating setup for diamond anvil cells for in situ synchrotron and in house high and ultra-high pressure studies. Rev. Sci. Instrum. 90, 104501. https://doi.org/10.1063/1.5117786

Fei, Y., Murphy, C., Shibazaki, Y., Shahar, A., Huang, H., 2016. Thermal equation of state of hcp-iron: Constraint on the density deficit of Earth's solid inner core. Geophys. Res. Lett. 43, 6837–6843. https://doi.org/10.1002/2016GL069456

Gonzalez-Platas, J., Alvaro, M., Nestola, F., Angel, R., 2016. EosFit7-GUI : a new graphical user interface for equation of state calculations, analyses and teaching. J. Appl. Crystallogr. 49, 1377–1382. https://doi.org/10.1107/S1600576716008050

Hirayama, Y., Fujii, T., Kurita, K., 1993. The melting relation of the system, iron and carbon at high pressure and its bearing on the early stage of the Earth. Geophys. Res. Lett. 20, 2095–2098. https://doi.org/10.1029/93GL02131

Li, J., Mao, H.K., Fei, Y., Gregoryanz, E., Eremets, M., Zha, C.S., 2002. Compression of Fe 3 C to 30 GPa at room temperature. Phys. Chem. Miner. 29, 166–169. https://doi.org/10.1007/s00269-001-0224-4

Liermann, H.-P., Konôpková, Z., Morgenroth, W., Glazyrin, K., Bednarčik, J., McBride, E.E., Petitgirard, S., Delitz, J.T., Wendt, M., Bican, Y., Ehnes, A., Schwark, I., Rothkirch, A., Tischer, M., Heuer, J., Schulte-Schrepping, H., Kracht, T., Franz, H., 2015. The Extreme Conditions Beamline P02.2 and the Extreme Conditions Science Infrastructure at PETRA III. J. Synchrotron Radiat. 22, 908–924. https://doi.org/10.1107/S1600577515005937

Litasov, K.D., Shatskiy, A.F., 2016. Composition of the Earth's core: A review. Russ. Geol. Geophys. 57, 22–46. https://doi.org/10.1016/j.rgg.2016.01.003

Liu, J., Lin, J.-F., Prakapenka, V.B., Prescher, C., Yoshino, T., 2016. Phase relations of Fe 3 C and Fe 7 C 3 up to 185 GPa and 5200 K: Implication for the stability of iron carbide in the Earth's core. Geophys. Res. Lett. 43, 12,415-12,422. https://doi.org/10.1002/2016GL071353

Lord, O.T., Walter, M.J., Dasgupta, R., Walker, D., Clark, S.M., 2009. Melting in the Fe–C system to 70 GPa. Earth Planet. Sci. Lett. 284, 157–167. https://doi.org/10.1016/j.epsl.2009.04.017

McDonough, W.F., 2003. Compositional Model for the Earth's Core, in: Treatise on Geochemistry. Elsevier, pp. 547–568. https://doi.org/10.1016/B0-08-043751-6/02015-6

Morard, G., Boccato, S., Rosa, A.D., Anzellini, S., Miozzi, F., Henry, L., Garbarino, G., Mezouar, M., Harmand, M., Guyot, F., Boulard, E., Kantor, I., Irifune, T., Torchio, R., 2018. Solving Controversies on the Iron Phase Diagram Under High Pressure. Geophys. Res. Lett. 45. https://doi.org/10.1029/2018GL079950

Nakajima, Y., Takahashi, E., Suzuki, T., Funakoshi, K., 2009. "Carbon in the core" revisited. Phys. Earth Planet. Inter. 174, 202–211. https://doi.org/10.1016/j.pepi.2008.05.014

Petříček, V., Dušek, M., Plášil, J., 2016. Crystallographic computing system Jana2006: solution and refinement of twinned structures. Zeitschrift für Krist. - Cryst. Mater. 231. https://doi.org/10.1515/zkri-2016-1956

Poirier, J.-P., 1994. Light elements in the Earth's outer core: A critical review. Phys. Earth Planet. Inter. 85, 319–337. https://doi.org/10.1016/0031-9201(94)90120-1

Prescher, C., Dubrovinsky, L., Bykova, E., Kupenko, I., Glazyrin, K., Kantor, A., McCammon, C., Mookherjee, M., Nakajima, Y., Miyajima, N., Sinmyo, R., Cerantola, V., Dubrovinskaia, N., Prakapenka, V., Rüffer, R., Chumakov, A., Hanfland, M., 2015. High Poisson's ratio of Earth's inner core explained by carbon alloying. Nat. Geosci. 8, 220–223. https://doi.org/10.1038/ngeo2370

Prescher, C., Dubrovinsky, L., McCammon, C., Glazyrin, K., Nakajima, Y., Kantor, A., Merlini, M., Hanfland, M., 2012. Structurally hidden magnetic transitions in Fe3C at high pressures. Phys. Rev. B 85, 140402. https://doi.org/10.1103/PhysRevB.85.140402

Prescher, C., Prakapenka, V.B., 2015. DIOPTAS : a program for reduction of two-dimensional X-ray diffraction data and data exploration. High Press. Res. 35, 223–230. https://doi.org/10.1080/08957959.2015.1059835

Reagan, M.M., Gleason, A.E., Liu, J., Krawczynski, M.J., Van Orman, J.A., Mao, W.L., 2018. The effect of nickel on the strength of iron nickel alloys: Implications for the Earth's inner core. Phys. Earth Planet. Inter. 283, 43–47. https://doi.org/10.1016/j.pepi.2018.08.003

Rigaku Oxford Diffraction, 2018. CrysAlis Pro (v. 171.39.46).

Ringwood, A.E., 1960. Cohenite as a pressure indicator in iron meteorites. Geochim. Cosmochim. Acta 20, 155–158. https://doi.org/10.1016/0016-7037(60)90059-4

Scott, H.P., Williams, Q., Knittle, E., 2001. Stability and equation of state of Fe 3 C to 73 GPa: Implications for carbon in the Earth's core. Geophys. Res. Lett. 28, 1875–1878. https://doi.org/10.1029/2000GL012606

Sheldrick, G.M., 2015. SHELXT – Integrated space-group and crystal-structure

determination. Acta Crystallogr. Sect. A Found. Adv. 71, 3–8. https://doi.org/10.1107/S2053273314026370

Torchio, R., Boccato, S., Miozzi, F., Rosa, A.D., Ishimatsu, N., Kantor, I., Sévelin-Radiguet, N., Briggs, R., Meneghini, C., Irifune, T., Morard, G., 2020. Melting Curve and Phase Relations of Fe-Ni Alloys: Implications for the Earth's Core Composition. Geophys. Res. Lett. 47. https://doi.org/10.1029/2020GL088169

Wood, B.J., 1993. Carbon in the core. Earth Planet. Sci. Lett. 117, 593–607. https://doi.org/10.1016/0012-821X(93)90105-I

List of all author publications

[1] D. Laniel, B. Winkler, E. Koemets, **T. Fedotenko**, S. Chariton, V. Milman, K. Glazyrin, V. Prakapenka, L. Dubrovinsky, N. Dubrovinskaia, Nitrosonium nitrate (NO + NO^{3-}) structure solution using in situ single-crystal X-ray diffraction in a diamond anvil cell, IUCrJ. 8 (2021) 208–214. doi:10.1107/S2052252521000075.

[2] D. Laniel, J. Binck, B. Winkler, S. Vogel, **T. Fedotenko**, S. Chariton, V. Prakapenka, V. Milman, W. Schnick, L. Dubrovinsky, N. Dubrovinskaia, Synthesis, crystal structure and structure–property relations of strontium orthocarbonate, Sr_2CO_4, Acta Crystallogr. Sect. B Struct. Sci. Cryst. Eng. Mater. 77 (2021) 131–137. doi:10.1107/S2052520620016650.

[3] E. Koemets, I. Leonov, M. Bykov, E. Bykova, S. Chariton, G. Aprilis, **T. Fedotenko**, S. Clément, J. Rouquette, J. Haines, V. Cerantola, K. Glazyrin, C. McCammon, V.B. Prakapenka, M. Hanfland, H.-P. Liermann, V. Svitlyk, R. Torchio, A.D. Rosa, T. Irifune, A. V. Ponomareva, I.A. Abrikosov, N. Dubrovinskaia, L. Dubrovinsky, Revealing the Complex Nature of Bonding in the Binary High-Pressure Compound FeO_2, Phys. Rev. Lett. 126 (2021) 106001. doi:10.1103/PhysRevLett.126.106001.

[4] G. Aprilis, A. Pakhomova, S. Chariton, S. Khandarkhaeva, C. Melai, E. Bykova, M. Bykov, **T. Fedotenko**, E. Koemets, C. McCammon, A.I. Chumakov, M. Hanfland, N. Dubrovinskaia, L. Dubrovinsky, The Effect of Pulsed Laser Heating on the Stability of Ferropericlase at High Pressures, Minerals. 10 (2020) 542. doi:10.3390/min10060542.

[5] **T. Fedotenko**, L. Dubrovinsky, S. Khandarkhaeva, S. Chariton, E. Koemets, I. Koemets, M. Hanfland, N. Dubrovinskaia, Synthesis of palladium carbides and palladium hydride in laser heated diamond anvil cells, J. Alloys Compd. 844 (2020) 156179. doi:10.1016/j.jallcom.2020.156179.

[6] T. Meier, F. Trybel, G. Criniti, D. Laniel, S. Khandarkhaeva, E. Koemets, **T. Fedotenko**, K. Glazyrin, M. Hanfland, M. Bykov, G. Steinle-Neumann, N. Dubrovinskaia, L. Dubrovinsky, Proton mobility in metallic copper hydride from high-pressure nuclear magnetic resonance, Phys. Rev. B. 102 (2020) 165109. doi:10.1103/PhysRevB.102.165109.

[7] K. V. Yusenko, S.A. Martynova, S. Khandarkhaeva, **T. Fedotenko**, K. Glazyrin, E. Koemets, M. Bykov, M. Hanfland, K. Siemensmeyer, A. Smekhova, S.A. Gromilov, L.S. Dubrovinsky, High

compressibility of synthetic analogous of binary iridium–ruthenium and ternary iridium–osmium–ruthenium minerals, Materialia. 14 (2020) 100920. doi:10.1016/j.mtla.2020.100920.

[8] S. Chariton, M. Bykov, E. Bykova, E. Koemets, **T. Fedotenko**, B. Winkler, M. Hanfland, V.B. Prakapenka, E. Greenberg, C. McCammon, L. Dubrovinsky, The crystal structures of Fe-bearing $MgCO_3$ sp 2 - and sp 3 -carbonates at 98 GPa from single-crystal X-ray diffraction using synchrotron radiation, Acta Crystallogr. Sect. E Crystallogr. Commun. 76 (2020) 715–719. doi:10.1107/S2056989020005411.

[9] S. Khandarkhaeva, **T. Fedotenko**, M. Bykov, E. Bykova, S. Chariton, P. Sedmak, K. Glazyrin, V. Prakapenka, N. Dubrovinskaia, L. Dubrovinsky, Novel Rhenium Carbides at 200 GPa, Eur. J. Inorg. Chem. 2020 (2020) 2186–2190. doi:10.1002/ejic.202000252.

[10] A. Pakhomova, D. Simonova, I. Koemets, E. Koemets, G. Aprilis, M. Bykov, L. Gorelova, **T. Fedotenko**, V. Prakapenka, L. Dubrovinsky, Polymorphism of feldspars above 10 GPa, Nat. Commun. 11 (2020) 2721. doi:10.1038/s41467-020-16547-4.

[11] D. Laniel, B. Winkler, **T. Fedotenko**, A. Pakhomova, S. Chariton, V. Milman, V. Prakapenka, L. Dubrovinsky, N. Dubrovinskaia, High-Pressure Polymeric Nitrogen Allotrope with the Black Phosphorus Structure, Phys. Rev. Lett. 124 (2020) 216001. doi:10.1103/PhysRevLett.124.216001.

[12] S. Chariton, C. McCammon, D.M. Vasiukov, M. Stekiel, A. Kantor, V. Cerantola, I. Kupenko, **T. Fedotenko**, E. Koemets, M. Hanfland, A.I. Chumakov, L. Dubrovinsky, Seismic detectability of carbonates in the deep Earth: A nuclear inelastic scattering study, Am. Mineral. 105 (2020) 325–332. doi:10.2138/am-2020-6901.

[13] D.A. Kudryavtsev, **T.M. Fedotenko**, E.G. Koemets, S.E. Khandarkhaeva, V.G. Kutcherov, L.S. Dubrovinsky, Raman Spectroscopy Study on Chemical Transformations of Propane at High Temperatures and High Pressures, Sci. Rep. 10 (2020) 1483. doi:10.1038/s41598-020-58520-7.

[14] M. Bykov, S. Chariton, E. Bykova, S. Khandarkhaeva, **T. Fedotenko**, A. V. Ponomareva, J. Tidholm, F. Tasnádi, I.A. Abrikosov, P. Sedmak, V. Prakapenka, M. Hanfland, H. Liermann, M. Mahmood, A.F. Goncharov, N. Dubrovinskaia, L. Dubrovinsky, Innenrücktitelbild: High-Pressure Synthesis of Metal–Inorganic Frameworks Hf_4N_{20} N_2 , WN_8 N_2 , and Os_5N_{28} $3N_2$ with Polymeric Nitrogen Linkers (Angew. Chem. 26/2020), Angew. Chemie. 132 (2020) 10753–10753. doi:10.1002/ange.202005697.

[15] K. V. Yusenko, S. Khandarkhaeva, M. Bykov, **T. Fedotenko**, M. Hanfland, A. Sukhikh, S.A. Gromilov, L.S. Dubrovinsky, Face-Centered Cubic Refractory Alloys Prepared from Single-Source Precursors, Materials (Basel). 13 (2020) 1418. doi:10.3390/ma13061418.

[16] K. V. Yusenko, K. Spektor, S. Khandarkhaeva, **T. Fedotenko**, A. Pakhomova, I. Kupenko, A. Rohrbach, S. Klemme, W.A. Crichton, T. V. Dyachkova, A.P. Tyutyunnik, Y.G. Zainulin, L.S. Dubrovinsky, S.A. Gromilov, Decomposition of single-source precursors under high-temperature high-pressure to access osmium–platinum refractory alloys, J. Alloys Compd. 813 (2020) 152121. doi:10.1016/j.jallcom.2019.152121.

[17] G. Aprilis, I. Kantor, I. Kupenko, V. Cerantola, A. Pakhomova, I.E. Collings, R. Torchio, **T. Fedotenko**, S. Chariton, M. Bykov, E. Bykova, E. Koemets, D.M. Vasiukov, C. McCammon, L. Dubrovinsky, N. Dubrovinskaia, Comparative study of the influence of pulsed and continuous wave laser heating on the mobilization of carbon and its chemical reaction with iron in a diamond anvil cell, J. Appl. Phys. 125 (2019) 095901. doi:10.1063/1.5067268.

[18] T. Meier, A.P. Dwivedi, S. Khandarkhaeva, **T. Fedotenko**, N. Dubrovinskaia, L. Dubrovinsky, Table-top nuclear magnetic resonance system for high-pressure studies with in situ laser heating, Rev. Sci. Instrum. 90 (2019) 123901. doi:10.1063/1.5128592.

[19] D. Laniel, B. Winkler, E. Koemets, **T. Fedotenko**, M. Bykov, E. Bykova, L. Dubrovinsky, N. Dubrovinskaia, Synthesis of magnesium-nitrogen salts of polynitrogen anions, Nat. Commun. 10 (2019) 4515. doi:10.1038/s41467-019-12530-w.

[20] K. V. Yusenko, S. Khandarkhaeva, **T. Fedotenko**, A. Pakhomova, S.A. Gromilov, L. Dubrovinsky, N. Dubrovinskaia, Equations of state of rhodium, iridium and their alloys up to 70 GPa, J. Alloys Compd. 788 (2019) 212–218. doi:10.1016/j.jallcom.2019.02.206.

[21] T. Meier, F. Trybel, S. Khandarkhaeva, G. Steinle-Neumann, S. Chariton, **T. Fedotenko**, S. Petitgirard, M. Hanfland, K. Glazyrin, N. Dubrovinskaia, L. Dubrovinsky, Pressure-Induced Hydrogen-Hydrogen Interaction in Metallic FeH Revealed by NMR, Phys. Rev. X. 9 (2019) 031008. doi:10.1103/PhysRevX.9.031008.

[22] M. Bykov, S. Chariton, H. Fei, **T. Fedotenko**, G. Aprilis, A. V. Ponomareva, F. Tasnádi, I.A. Abrikosov, B. Merle, P. Feldner, S. Vogel, W. Schnick, V.B. Prakapenka, E. Greenberg, M. Hanfland, A. Pakhomova, H.-P. Liermann, T. Katsura, N. Dubrovinskaia, L. Dubrovinsky, High-pressure

synthesis of ultraincompressible hard rhenium nitride pernitride $Re_2(N_2)(N)_2$ stable at ambient conditions, Nat. Commun. 10 (2019) 2994. doi:10.1038/s41467-019-10995-3.

[23] **T. Fedotenko**, L. Dubrovinsky, G. Aprilis, E. Koemets, A. Snigirev, I. Snigireva, A. Barannikov, P. Ershov, F. Cova, M. Hanfland, N. Dubrovinskaia, Laser heating setup for diamond anvil cells for in situ synchrotron and in house high and ultra-high pressure studies, Rev. Sci. Instrum. 90 (2019) 104501. doi:10.1063/1.5117786.

[24] D. Laniel, M. Bykov, **T. Fedotenko**, A. V. Ponomareva, I.A. Abrikosov, K. Glazyrin, V. Svitlyk, L. Dubrovinsky, N. Dubrovinskaia, High Pressure Investigation of the S–N 2 System up to the Megabar Range: Synthesis and Characterization of the SN 2 Solid, Inorg. Chem. 58 (2019) 9195–9204. doi:10.1021/acs.inorgchem.9b00830.

[25] M. Bykov, E. Bykova, E. Koemets, **T. Fedotenko**, G. Aprilis, K. Glazyrin, H.-P. Liermann, A. V. Ponomareva, J. Tidholm, F. Tasnádi, I.A. Abrikosov, N. Dubrovinskaia, L. Dubrovinsky, High-Pressure Synthesis of a Nitrogen-Rich Inclusion Compound ReN_8 N_2 with Conjugated Polymeric Nitrogen Chains, Angew. Chemie. 130 (2018) 9186–9191. doi:10.1002/ange.201805152.

[26] M. Bykov, S. Khandarkhaeva, **T. Fedotenko**, P. Sedmak, N. Dubrovinskaia, L. Dubrovinsky, Synthesis of FeN_4 at 180 GPa and its crystal structure from a submicron-sized grain, Acta Crystallogr. Sect. E Crystallogr. Commun. 74 (2018) 1392–1395. doi:10.1107/S2056989018012161.

(Eidesstattliche) Versicherungen und Erklärungen

(§ 9 Satz 2 Nr. 3 PromO BayNAT)

Hiermit versichere ich eidesstattlich, dass ich die Arbeit selbstständig verfasst und keine anderen als die von mir angegebenen Quellen und Hilfsmittel benutzt habe (vgl. Art. 64 Abs. 1 Satz 6 BayHSchG).

(§ 9 Satz 2 Nr. 3 PromO BayNAT)

Hiermit erkläre ich, dass ich die Dissertation nicht bereits zur Erlangung eines akademischen Grades eingereicht habe und dass ich nicht bereits diese oder eine gleichartige Doktorprüfung endgültig nicht bestanden habe.

(§ 9 Satz 2 Nr. 4 PromO BayNAT)

Hiermit erkläre ich, dass ich Hilfe von gewerblichen Promotionsberatern bzw. -vermittlern oder ähnlichen Dienstleistern weder bisher in Anspruch genommen habe noch künftig in Anspruch nehmen werde.

(§ 9 Satz 2 Nr. 7 PromO BayNAT)

Hiermit erkläre ich mein Einverständnis, dass die elektronische Fassung meiner Dissertation unter Wahrung meiner Urheberrechte und des Datenschutzes einer gesonderten Überprüfung unterzogen werden kann.

(§ 9 Satz 2 Nr. 8 PromO BayNAT)

Hiermit erkläre ich mein Einverständnis, dass bei Verdacht wissenschaftlichen Fehlverhaltens Ermittlungen durch universitätsinterne Organe der wissenschaftlichen Selbstkontrolle stattfinden können.

…….

Ort, Datum, Unterschrift